
Measuring Young Planets from their Spiral Wakes

HONOURS THESIS

by Thomas Hilder

Supervisors:

Prof. Daniel Price
A/Prof. Christophe Pinte



School of Physics and Astronomy
Monash University

November 2022

Abstract

We present a semi-analytic framework for detecting and measuring planets through measurements of their spiral wakes in observations of protoplanetary disk kinematics. Building on previous work, we provide improvements to the accuracy and speed of semi-analytic models for the planet-disk interaction, and present our Python package WAKEFLOW that can readily generate these models in a few seconds. This work is then used to constrain potential planets in observations of the circumstellar disks of HD 163296, HD 169142, and IM Lupi by modelling the signatures of planet wakes present in molecular line emission. Finally, we present our preliminary work on the development of a fitting procedure for planet mass, using WAKEFLOW models.

Publication List

Chapter 4: Section 4.1 has been submitted for publication as

Hilder T., Fasano D., Bollati F., Vandenberg J., 2022, “*Wakeflow: A Python Package For Semi-Analytic Models of Planet Wakes*”.

Section 4.3.4 presents part of an upcoming paper

Fasano D., Lodato G., Toci C., Price D. J., **Hilder T.**, Pinte C., 2022, “*The theory of kinks — II. Testing the accuracy of the model in the high mass limit*”. In prep.

Chapter 5: Section 5.1 is published as part of

Garg H., Pinte C., Hammond I., Teague R., **Hilder T.**, Price D. J., Calcino J., Christiaens V., Poblete P. P., 2022, “*A kinematic excess in the annular gap and gas depleted cavity in the disc around HD 169142*”. Monthly Notices of the Royal Astronomical Society. Manuscript in press.

Section 5.2 is published as part of

Verrios H. J., Price D. J., Pinte C., **Hilder T.**, Calcino J., 2022, “*Kinematic Evidence for an Embedded Planet in the IM Lupi Disk*”. The Astrophysical Journal Letters, 934, L11.

Acknowledgements

I would like to thank my supervisors, Daniel Price and Christophe Pinte, for their guidance, wisdom and support over the course of the year. I feel privileged to have been part of a team that is dedicated to both high quality research and to having a laugh along the way. Thank you also to my collaborators, and to everyone in the SPH group. And of course I cannot forget my fellow honours students; while the year was certainly challenging, sharing it with so many great people helped make it all worthwhile.

I would also like to thank my partner Kayla for her constant support and seemingly limitless reserves of patience. Finally, thank you to my parents for teaching me to be curious and that no challenge is insurmountable.

It doesn't stop being magic just because you know how it works.

– Terry Pratchett

Preface

This thesis presents a complete account of the research I have completed as a part of my honours year. In April of this year my first scientific paper was published, where I was second-author, based on work done in my final year of undergraduate studies¹. The work done in that paper constitutes the necessary groundwork for the research presented here. This year I have additionally contributed to two further publications on the kinematic detection of young planets, working as part of the SPH group here at Monash²³. I am also an author on a manuscript in preparation concerned with testing the theory of velocity kinks, led by our collaborators at the University of Milan in Italy⁴. Finally, I produced my first leading-author paper, on the software package I wrote to produce semi-analytic models of planet wakes, which has been submitted to the Journal of Open Source Software and is currently in review⁵. My contributions to each of these projects, as well as the other work I completed in my honours year, are presented in this document.

¹Calcino et al. 2022

²Verrios et al. 2022

³Garg et al. 2022

⁴Fasano et al., in prep.

⁵Hilder et al., submitted.

Contents

Abstract	i
Publication List	ii
Acknowledgements	iii
Preface	iv
1 Introduction	1
1.1 Overview	1
1.1.1 Protoplanet detection	2
1.1.2 Disk substructures	3
1.2 Kinematic Observations	4
1.2.1 Semi-analytic models	5
2 Protoplanetary Disks	9
2.1 Accretion Disks	9
2.1.1 Fluid equations	9
2.2 Theoretical Structure	11
2.2.1 Vertical density structure	11
2.2.2 Rotation	12
2.2.3 Disk flaring	12
2.3 Viscous Evolution	13
2.4 Observed Properties	14
2.4.1 Components	14
2.4.2 Size	15
2.4.3 Mass	15
3 Planet-Disk Interaction	18
3.1 Spiral Density Waves	18
3.1.1 Spiral structure preliminaries	19
3.1.2 No leading spirals	20
3.2 The Linear Disk Response	21
3.2.1 Tightly-wound density waves	23
3.2.2 Perturbed potential under WKB	23
3.2.3 The Lin-Shu dispersion relation	24
3.2.4 Stability	24
3.3 Planet Forcing	24
3.3.1 Lindblad resonances	25
3.3.2 The planet wake	28
3.3.3 Additional spiral arms	31
3.4 Linear Planet Wake Excitation	32
3.5 Non-Linear Planet Wake Evolution	35
3.5.1 Wave dissipation	37
3.5.2 Asymptotic planet mass scaling	38
3.6 Gap Opening	40
4 Semi-Analytic Models of Planet Wakes	42
4.1 Wakeflow: A Python Package For Semi-Analytic Models of Planet Wakes	42
4.2 Semi-Analytic Solution Algorithm	43
4.3 Theoretical and Numerical Considerations	44
4.3.1 Unperturbed disk structure	44

4.3.2	Linear box	45
4.3.3	Transformations	46
4.3.4	The high mass regime	47
4.3.5	Velocity perturbations	49
5	HD 169142 and IM Lupi: Applications of the Models	54
5.1	The Kinematic Arc in HD 169142	54
5.1.1	Introduction	54
5.1.2	Observations and analysis	55
5.1.3	Semi-analytical modelling	55
5.2	The Planet Wake in IM Lupi	57
5.2.1	Introduction	57
5.2.2	Simulated model	58
5.2.3	Tracing the wake	58
6	Quantitative Measurements of the Wake	60
6.1	Peak velocity fitting	60
6.1.1	Models	60
6.1.2	Fitting procedure	61
6.1.3	Background fitting	63
6.1.4	Planet fitting	64
6.1.5	Model-model fitting	66
6.1.6	Discussion	66
6.2	Mirror Residuals	68
7	Conclusion	70
7.1	Future Work	71
A	1D Isentropic Gas	72
	Bibliography	74

1

Introduction

1.1 Overview

This thesis is concerned with solving one of the principal problems in the field of planet formation, how can we detect newly-formed planets, and measure their properties? Answering these question is a vital step in constraining the various theoretical models of the planet formation process.

Stars and planets are born inside vast, interstellar clouds of gas and dust. Sometimes called “stellar nurseries”, these regions make up less than one percent of the interstellar volume of the Milky Way galaxy (Ferrière, 2001). Unlike the majority of the interstellar medium, which is ionised, the *molecular clouds* of star-forming regions are composed primarily of gaseous H₂. The typical size and mass range of these clouds are 2 – 15 pc and 10³ – 10⁵ M_⊙ respectively (Cambrésy, 1999), where M_⊙ is a solar mass. Stars form as a result of the collapse of the cloud, through the gravitational instability acting on turbulent flows (see review by Mac Low and Klessen, 2004).

The Solar System contains clues for how planets are subsequently formed around newborn stars. The mass and angular momentum of the Sun and planets are segregated, with the Sun containing 99.86% of the total mass, and the orbits of the planets accounting for 98.5% of the total angular momentum (e.g. Woolfson, 2000). Accounting for this proved to be a significant challenge for early models of the Solar System’s formation, eventually culminating in the idea that the planets must have formed from a disk of gas and dust surrounding the Sun (see review by Edgeworth, 1949). Such disks are known as *circumstellar disks*, and they are a natural consequence of the star formation process; conservation of angular momentum prevents complete collapse, and instead a disk is formed (Hoyle, 1953). The outward transport of angular momentum and inward transport of mass is then facilitated by stresses and instabilities that operate within the disk (Lynden-Bell and Pringle, 1974; Pringle, 1981). The disks found around young stars are thought to be the sites of planet formation, and are therefore known as *protoplanetary disks*.

Protoplanetary disks have lifetimes on the order of a few Myr before they eventually disperse (Mamajek, 2009). Planets are formed some time during this period, although the efficiency of planet formation is not well known (see review by Helled et al., 2014). *Planetesimals* are formed in the disk through the repeated collision of dust and ice particles, resulting in the eventual formation of larger bodies. Terrestrial planets, and possibly the cores of gas and ice giants, are then thought to form through the subsequent accretion of planetesimals and the surrounding gas and dust (e.g. Johansen et al., 2014). Two competing models hope to explain giant planet formation, *core accretion* (CA; Safronov, 1972; Lissauer, 1993; Pollack et al., 1996) and *gravitational instability* (GI; Boss, 1997). CA provides a good explanation for the observed composition of the planets in the Solar System, as well as the known correlation between stellar metallicity and giant planet occurrence. Notably, the formation timescale in this scenario is comparable to the lifetime of the disk. On the other hand, GI allows planets to form essentially immediately, while the star is still embedded in its envelope. However, it

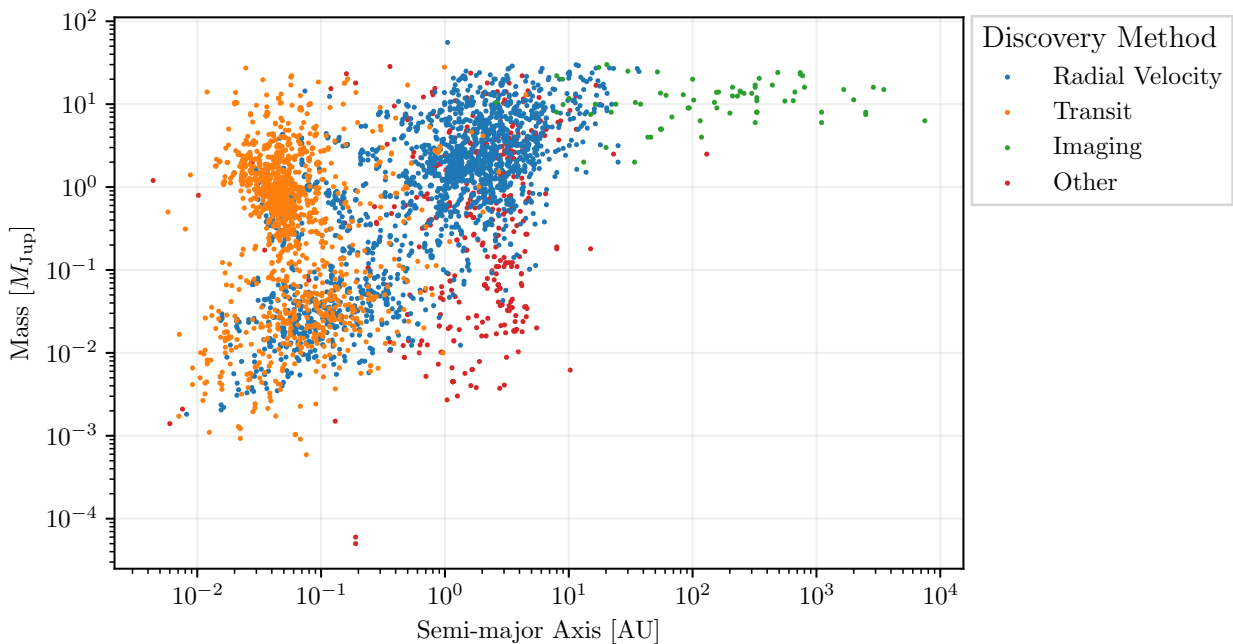


Figure 1.1: Distribution of known exoplanet mass and orbital radii, coloured by detection method. Data taken from *The Nasa Exoplanet Archive* <https://exoplanetarchive.ipac.caltech.edu>

also faces challenges explaining the observed composition and correlations previously mentioned (see review by Helled et al., 2014). Therefore, detecting and measuring the properties of newly formed planets while they are still in their natal disks will provide key constraints on these models, and insights into the physics driving planet formation.

1.1.1 Protoplanet detection

The first planet outside our own Solar System, called an *exoplanet*, was discovered in 1995 by Michael Mayor and graduate student Didier Queloz. 51 Pegasi b is a “hot Jupiter”, with a mass of $\sim 0.5 M_J$ and orbital period of ~ 4 days (where M_J is a Jupiter mass). This places it nearly 20 times closer to its star, than the Earth is to the Sun (Mayor and Queloz, 1995). In the nearly 30 years since that landmark discovery the number of confirmed exoplanets has skyrocketed to 5197 as of the time of writing¹. The mass and orbital radius distribution of these planets is shown in Figure 1.1. Primarily, these detections have come from the transit and radial velocity methods. The transit method relies on measuring the period dimming of star light as the planet passes between the star and observer, while the radial velocity method measures the doppler-shift of emission lines due to the motion of the star around the system barycentre. Here, we are interested in the subset of exoplanets that have been detected while still embedded in their protoplanetary disks, so-called *protoplanets*. Unfortunately, despite the other successes of exoplanet surveys, the number of uncontroversially confirmed protoplanets sits at an unimpressive total of two. These are PDS 70 b and c, observed through direct imaging in the near-infrared (Keppler et al., 2018; Haffert et al., 2019). Figure 1.2 shows a high angular resolution image of PDS 70 taken with the Atacama Large Millimetre Array (ALMA) in continuum.

Detecting protoplanets is a formidable task, owing to their environment. The transit method is essentially unviable due to the presence of optically thick disk material in the system. On the other hand, radial velocity searches are hampered by the high starspot and accretion activity of young stars, which complicates disentangling planet signals present in spectra (Desort et al., 2007). Furthermore, protoplanetary disks can have radii of hundreds of au (e.g. Tripathi et al., 2017), and so many protoplanets may sit outside the region of parameter space detectable by these methods (see Figure 1.1). Another popular technique, direct imaging, is able to detect planets at these separations, but is not sensitive to planet masses under a few M_J (Jorquera et al., 2021). However direct imaging

¹From <https://exoplanetarchive.ipac.caltech.edu>, up-to-date as of 11/02/2022.

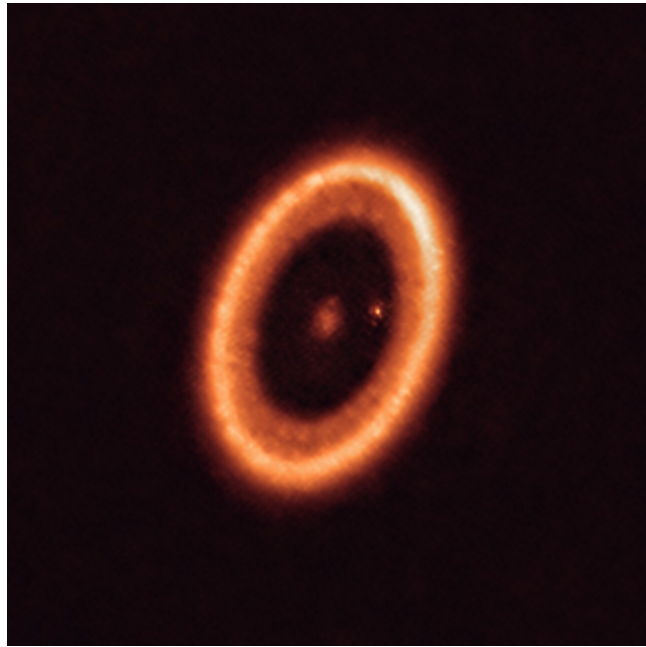


Figure 1.2: Band 7 ALMA image of the disk around PDS 70 ([Benisty et al., 2021](#)). The bright dot in the image is the circumplanetary disk around PDS 70c.

has still seen some successes, the two aforementioned confirmed planets in the disk of PDS 70, as well as a host of further claimed detections in the disks of HD 100546 ([Quanz et al., 2013a](#)), HD 169242 ([Biller et al., 2014](#)), LkCa15 ([Sallum et al., 2015](#)), MWC 758 ([Reggiani et al., 2018](#)) and AB Aurigae ([Currie et al., 2022](#)). Each of these are disputed in the literature ([Rameau et al., 2017; Ligi et al., 2018; Currie et al., 2019](#)) with the exception of PDS 70 b and c². The main difficulty with imaging is the possible confusion of disk material with a planet, since processing techniques can create spurious point sources from filamentary substructures like arcs and spirals (eg. [Rameau et al., 2017](#)).

1.1.2 Disk substructures

The difficulty in detecting protoplanets directly motivates studying the interactions between embedded planets and their host disks, in hopes of observationally identifying signatures induced by potential planets. The foundations of our theoretical models for the interaction between a disk and an embedded gravitating body were developed in the late 70s by [Goldreich and Tremaine \(1978, 1979, 1980\)](#), who were hoping to understand how Saturn's moons induce the spiral and concentric ring substructures within its rings. With the advent of the ALMA, we have begun to resolve the surfaces of protoplanetary disks at high resolution, and there we find evidence of the same kinds of interactions as those between Saturn's rings and moons. Figure 1.3 shows continuum observations of 20 disks taken as part of the Disk Substructures at High Angular Resolution Project (DSHARP; [Andrews et al., 2018a](#)). All of the disks imaged show some sort of substructure, including bright and dark rings, spiral arms and arcs. While alternative mechanisms have been suggested to drive the structures, such as the Rossby-wave instability ([Pinilla et al., 2012](#)), clumping ([Lyra and Kuchner, 2013](#)) or condensation fronts ([Zhang et al., 2015](#)), the most popular explanation is that they are driven by embedded planets ([Dipierro et al., 2015; Dong et al., 2015; Bae et al., 2017; Fedele et al., 2017, 2018; Zhang et al., 2018](#)). These observations provide evidence for early planet formation (e.g. fully formed planets in HL Tau with age < 1 Myr, see [Dipierro et al., 2015](#)), but they are far from a smoking gun due to the other proposed generation mechanisms. This thesis is concerned with disentangling these explanations, and confirming the presence of planets by instead looking for the characteristic way in which they perturb the velocity field of the disk. That is, through observations of the disk *kinematics*.

²AB Aurigae b is also currently not disputed in the literature but as of this writing the claimed detection is only 8 months old.

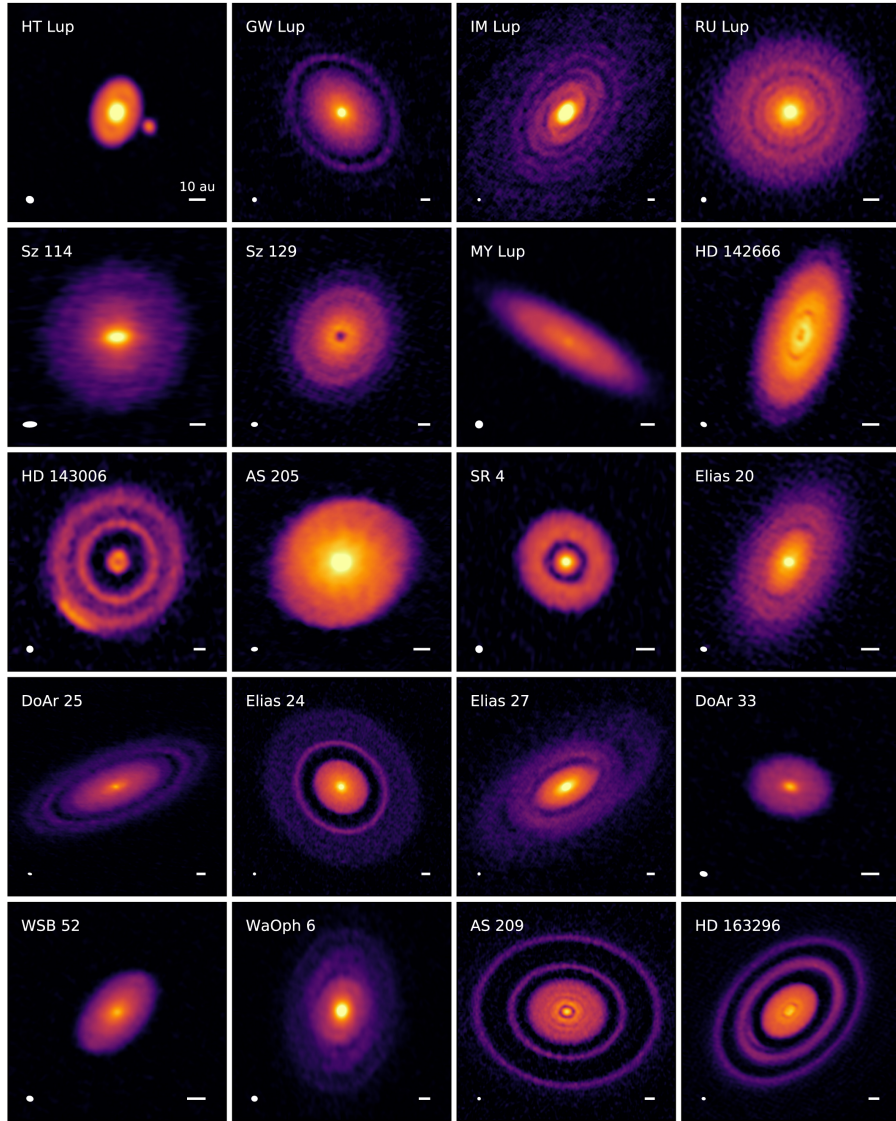


Figure 1.3: Continuum images taken at 1.5 mm of the 20 protoplanetary disks in the DSHARP program. The colour scale has been stretched to increase the contrast. ([Andrews et al., 2018a](#)). Substructures are evident in each disk. Notable examples include: the thin and wide rings in AS 209 and HD 163296, spiral arms in IM Lup and Elias 2-27, and a bright arc in HD 143006.

1.2 Kinematic Observations

We may probe the kinematics of a disk by measuring the Doppler shift of spectral line emission from different molecules and their isotopologues³. Such data comes in the form of channel maps, which make up a data cube that has two spatial dimensions and one frequency dimension. As it is the Doppler-shift of the line that is measured, the frequency dimension is equivalent to a velocity dimension. Thus, taking a velocity slice of the cube yields an image of all the material in the disk moving with the same line-of-sight velocity relative to the observer. Figure 1.4 shows velocity channels of ^{12}CO $J = 2 - 1$ rotational line emission from HD 163296, imaged with ALMA ([Andrews et al., 2018a](#)). The observations show the expected butterfly shape that is characteristic of Keplerian rotation ([de Gregorio-Monsalvo et al., 2013](#)). Note also that since ^{12}CO line emission occurs at multiple scale heights, there is a top and bottom surface in each image. Since velocity channels probe the material moving at a certain line-of-sight velocity, the maximum emission in each channel should trace an iso-velocity contour. These iso-velocity contours are the lines of constant line-of-sight velocity, and they should be continuous and smoothly varying in the absence of perturbations in the disk.

³Isotopologues are molecules that are different only by the isotopes of their atomic components.

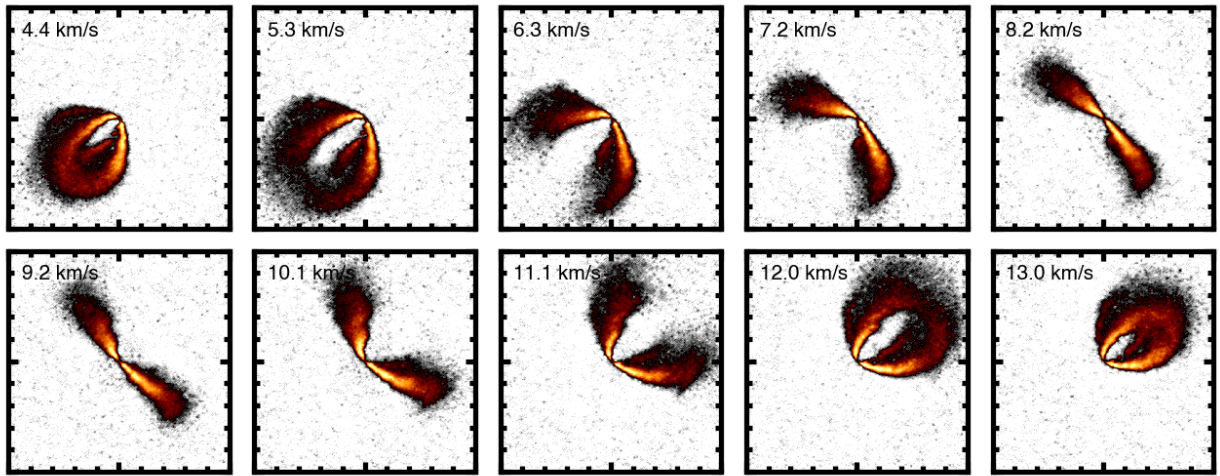


Figure 1.4: Velocity channels of ^{12}CO emission from the disk around HD 163296 (Andrews et al., 2018a). The colour corresponds to brightness temperature, ie. brighter means more emission (Disk Dynamics Collaboration et al., 2020). Each channel probes the material in the disk moving at a certain velocity, resulting in the butterfly patterns seen across the channels. Note also that the CO emitting layer sits above the disk mid-plane, and so there is both a top and bottom surface in each image, with one surface mostly obscured by the other.

Figure 1.5 shows a zoomed in view of one of the channels in HD 163296, highlighting the localised deviation from Keplerian rotation first found by Pinte et al. (2018b). Such deviations are called a “velocity kink”, and Pinte et al. (2018b) found that it matched the expected signature that should be produced by the gravitational disturbance of an embedded planet (Perez et al., 2015). Through 3D hydrodynamical modelling and radiation transfer simulations, Pinte et al. (2018b) showed that the density waves generated by such a planet can accurately recreate the observed kink. A comparison of their simulations with the observations is shown in Figure 1.6. A similar velocity kink was also found in the disk of HD 97048, and again detailed simulations show that a planet of a few M_J is capable of recreating the observations (Pinte et al., 2019). A follow up survey of the disks in the DSHARP sample found kinks in 8 out of 18 disks (Pinte et al., 2020). Importantly, all of the candidate protoplanets from that study lie within an observed dust gap or at the end of a spiral arm detected in continuum emission (Huang et al., 2018a,b; Pinte et al., 2020).

Further kinematic evidence for planets has been found through using the channels maps to calculate the velocity field of the disk, and then subtracting the best-fitting background rotation to generate residuals. Casassus and Pérez (2019) and Pérez et al. (2020) used this technique to identify a “Doppler flip” in the disk of HD 100546, where the velocity abruptly changes sign over the planet location. Furthermore, the high angular resolution gas observations taken as part of the Molecules with ALMA at Planet-forming Scales (MAPS) survey have allowed for detailed mapping of the kinematics in the disks of HD 163296 and MWC 480, with multiple spiral and arc structures detected (Teague et al., 2021). A similar analysis was performed with ALMA observations of TW Hya, with the authors claiming the detection of one large, coherent spiral structure (Teague et al., 2022).

Such kinematic observations provide support for the planet-disk interaction picture for disk substructures. Furthermore, they allow for the constraint of the planet mass through modelling of such interactions, as shown by Pinte et al. (2018b, 2019). However, the computational cost of full 3D hydrodynamical simulations prohibits their use as part of a robust fitting procedure. While statistical tools have recently shown promise in detecting and constraining planets through kinematics (Izquierdo et al., 2021, 2022), it would be valuable to do this through the physics of the interaction.

1.2.1 Semi-analytic models

Recently, Bollati et al. (2021) developed a theoretical framework for understanding velocity kinks through the creation of semi-analytic models of the planet wake. This work was based on the linear

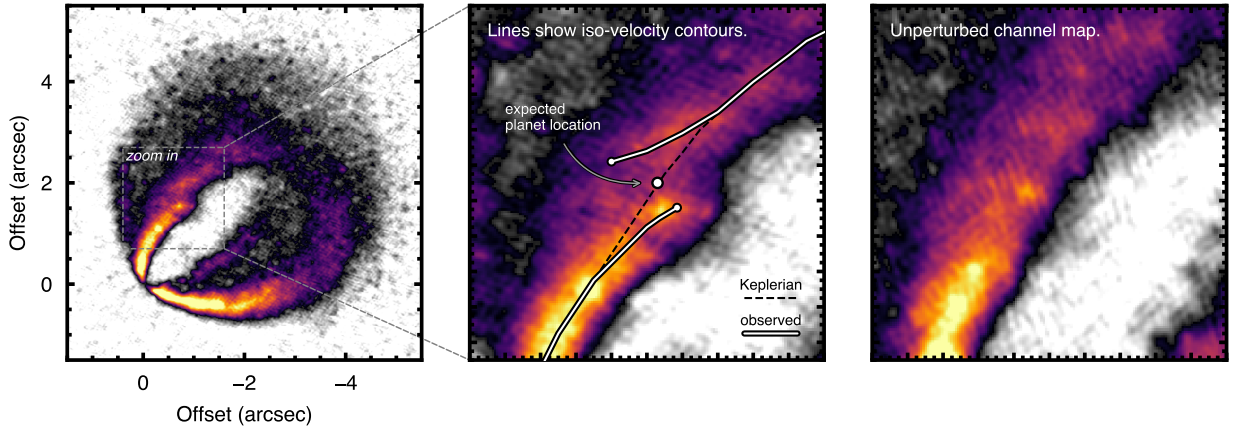


Figure 1.5: A close view of the 12 km/s velocity channel of HD 163296 (Andrews et al., 2018a), highlighting the velocity kink found by Pinte et al. (2018b) Comparing the middle and right panels, we see how the line of maximum emission deviates from the iso-velocity contour expected from pure Keplerian rotation. (Disk Dynamics Collaboration et al., 2020).

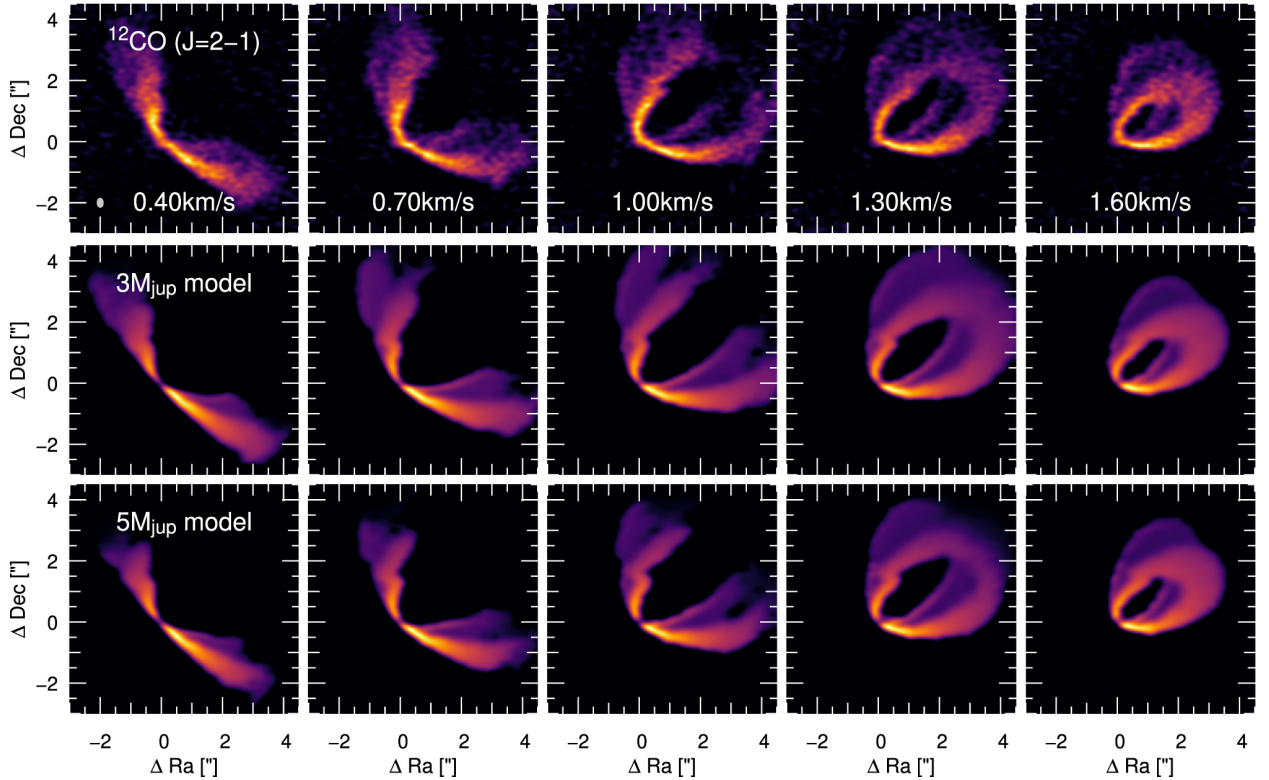


Figure 1.6: Comparison of ^{12}CO ALMA observations (top row) with the synthetic channel maps created from 3D hydrodynamical simulations of planet-disk interactions by Pinte et al. (2018b). The synthetic images were convolved with a Gaussian to match the beam size of the observations.

theory for the density waves excited in a disk by a gravitation body (Goldreich and Tremaine, 1980), as well a weakly non-linear theory for subsequent steepening into shock waves (Goodman and Rafikov, 2001; Rafikov, 2002a). In their view, velocity kinks are caused by these density waves perturbing the velocities of the disk, and they found that measuring the amplitude of the kinks should provide the necessary information needed to recover the planet mass. However, the mass obtained is in units that are very sensitive to the temperature structure of the disk, and so a robust planet mass measurement requires a tight constrain of this structure. They also found that velocity kinks arise due to the intersection of the planet wake and the velocity channels, and that these kinks are spread throughout the disk. Since at the time kinks were thought to be localised nearby the planet (Pinte et al., 2018b, 2019, 2020), Bollati suggested that viscous damping may suppress the amplitude of the wave as it travels through the disk.

In Calcino et al. (2022), we found that the HD 163296 is indeed host to velocity kinks far from the proposed planet location by using high resolution data from the Molecules with ALMA at Planet-Forming Scales program (MAPS; Öberg et al., 2021). Using this, we traced the outer planet wake through the disk, directly confirming the presence of a Lindblad planet wake for the first time. Figure 1.7 shows how this wake gives rise to the observed velocity kinks as it passes through the location probed by a velocity channel. This work showed that the wake-crossing interpretation of velocity kinks of Bollati et al. (2021) is indeed correct, and that there is no need for any damping. Importantly, the shape of the wake depends on the disk temperature, and so mapping the wake constrains the temperature structure of the disk, and so determines the unit for the planet mass.

Taken together the work presented in Bollati et al. (2021) and Calcino et al. (2022) provide the necessary ideas needed to recover a planet mass from observations of disk kinematics, by measuring both the amplitudes of velocity kinks, and the shape of the planet wake. This thesis builds on their work, by taking further steps towards the creation of a fitting procedure to do just this.

The structure of the thesis is as follows:

- Chapter 2 discusses the properties and structure of protoplanetary disks, from both a theoretical and observational point of view.
- Chapter 3 provides a theoretical overview of the planet-disk interaction, as well as the particular ideas behind the semi-analytic models.
- Chapter 4 presents our Python package for generating models of the planet wake excited by a planet embedded in a disk, and discusses improvements over the methods of Bollati et al. (2021).
- Chapter 5 presents applications of the semi-analytic the models, for kinematic planet detection in the disks of HD 169142 and IM Lupi.
- Chapter 6 presents our preliminary work on developing a fitting procedure to recover planet masses from kinematic observations using the semi-analytic models.

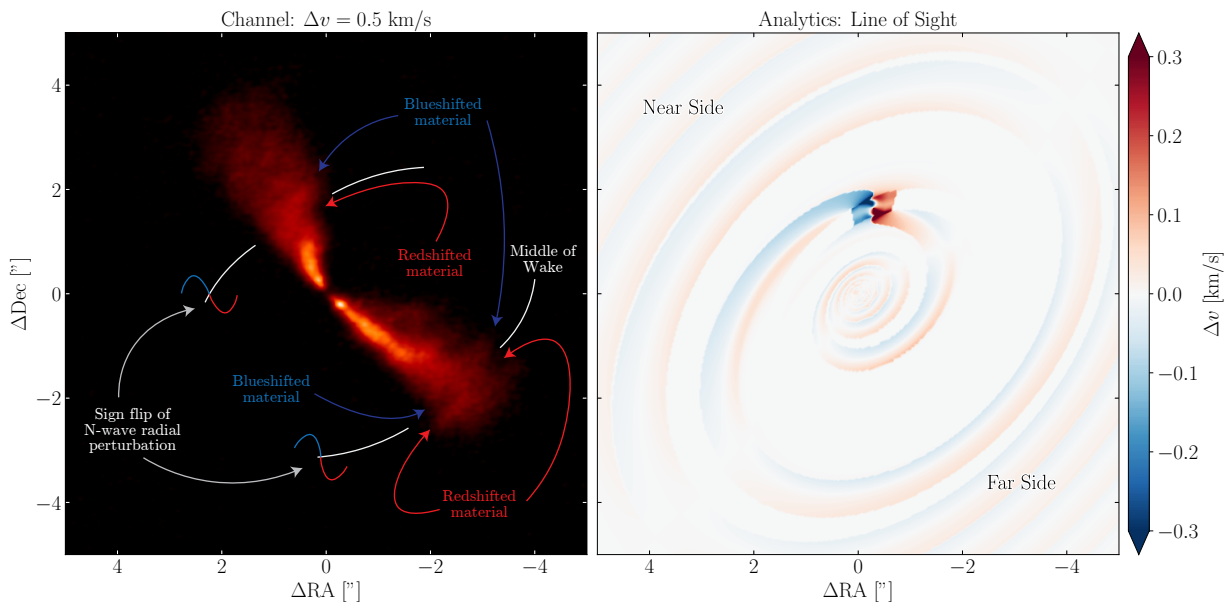


Figure 1.7: Comparison of one of the velocity channels of HD 163296 observed as part of the MAPS program (Öberg et al., 2021), with the analytic model (Bollati et al., 2021) of the proposed planet wake from Calcino et al. (2022). The observed kinks on each side of the disk are well explained by the crossing of the planet wake with the channel, as in Bollati et al. (2021).

2

Protoplanetary Disks

Before discussing the ways in which an embedded planet disturbs its host disk, we will first briefly outline physics underpinning accretion disks. This will be used to determine the structure of protoplanetary disks from a theoretical point of view. We then supplement this with a discussion of disk properties determined from observational studies, and of how these studies constrain the theoretical ideas.

2.1 Accretion Disks

After formation, young stars continue to grow in mass by accreting material from the inner edge of their disk. Protoplanetary disks are therefore also part of a larger class of astrophysical disks known as *accretion disks*. The angular velocity Ω of a test particle orbiting in a Newtonian point mass potential is given by

$$\Omega = \Omega_K \equiv \sqrt{\frac{GM_\star}{r^3}}, \quad (2.1)$$

where M_\star is the central mass, r is the orbital radius, G is Newton's constant, and we define Ω_K to be *Keplerian rotation*. Ω is a function of radius and so the rotation is said to be *differential*. The orbital speed v_ϕ is then a decreasing function of radius $v_\phi = r\Omega_K \propto r^{-1/2}$. In addition, the test particle specific angular momentum h is

$$h = r^2\Omega = \sqrt{GM_\star r}, \quad (2.2)$$

and is thus an increasing function of radius. In order for material in an accretion disk to move to lower radii, it needs to lose angular momentum. The differential rotation in the disk provides a natural mechanism for this transport due to the shearing stresses that occur between annuli of material orbiting at slightly different radii. Figure 2.1 shows a diagrammatic overview of this, where the inner annuli orbit faster than the outer annuli, resulting in shearing forces between them. Alternatively accretion may be powered by other disk instabilities or through an external torque, for example through magnetised outflows. Instead of attempting to consider the individual torques contributed by different instabilities or mechanisms operating in the disk, we will represent their overall effects as an effective fluid viscosity. This approach is known as *viscous disk theory* (Lynden-Bell and Pringle, 1974; Shakura and Sunyaev, 1973).

2.1.1 Fluid equations

Under the viscous disk theory framework we expect accretion disk structure and evolution to be described by the viscous and compressible equations of momentum and continuity. These are given

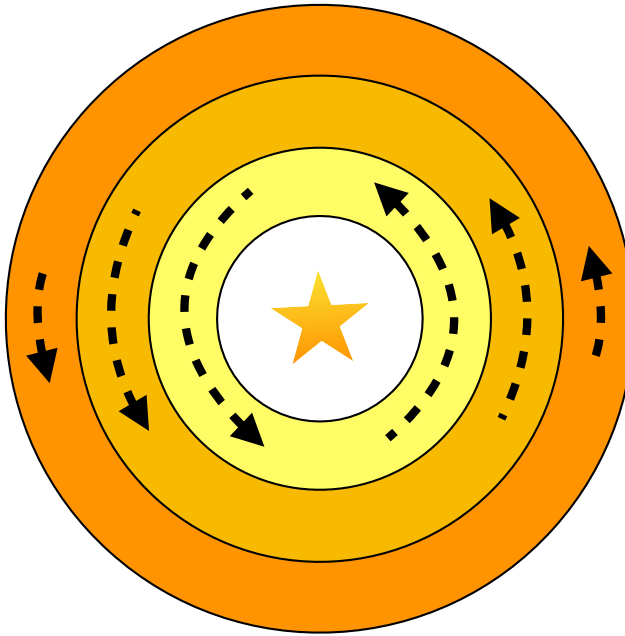


Figure 2.1: Cartoon diagram of an accretion disk, demonstrating the differential rotation of material orbiting at different radii. This results in shearing stresses and instabilities between neighbouring annuli of material.

by (e.g. [Landau and Lifshitz, 1987](#))

$$\partial_t \rho + \nabla \cdot (\rho \mathbf{v}) = 0, \quad (2.3)$$

$$\partial_t \mathbf{v} + (\mathbf{v} \cdot \nabla) \mathbf{v} = \frac{1}{\rho} (\nabla \cdot \mathcal{T} - \nabla P) - \nabla \Phi_*, \quad (2.4)$$

where ρ , P and \mathbf{v} are the fluid density, pressure and velocity respectively, \mathcal{T} is the viscous stress tensor and Φ_* is the gravitational potential of the central point mass (which is a star for a circumstellar disk). We will ignore any contributions to the potential from the disk itself, assuming $\Phi_{\text{disk}} \ll \Phi_*$.

Following the review by [Papaloizou and Lin \(1995\)](#), we will reduce Equations (2.3) and (2.4) to two one-dimensional conservation equations for a thin accretion disk. Expanding the continuity Equation (2.3) in cylindrical coordinates we find

$$\partial_t \rho + \nabla \cdot (\rho \mathbf{v}) = \partial_t \rho + \frac{1}{r} \partial_r (r \rho v_r) + \frac{1}{r} \partial_\phi (\rho v_\phi) + \partial_z (\rho v_z) = 0. \quad (2.5)$$

Integrating out the ϕ and z dependence causes the third term to vanish. We also neglect the fourth term assuming that $v_z \simeq 0$

$$0 = \partial_t \int_0^{2\pi} \int_{-\infty}^{\infty} \rho dz d\phi + \frac{1}{r} \partial_r \int_0^{2\pi} \int_{-\infty}^{\infty} r \rho v_r dz d\phi. \quad (2.6)$$

Performing this integration assuming the disk to be axisymmetric and that v_r is independent of z yields

$$\partial_t \Sigma + \frac{1}{r} \partial_r (r \Sigma v_r) = 0, \quad (2.7)$$

where the *surface density* Σ is defined as

$$\Sigma \equiv \int_{-\infty}^{\infty} \rho dz. \quad (2.8)$$

The resultant Equation (2.7) expresses that the total mass of the disk is conserved, even as material moves between adjacent annuli. To find the other conservation equation we take the ϕ component of the momentum Equation (2.4)

$$\partial_t v_\phi + (\mathbf{v} \cdot \nabla) v_\phi = \frac{1}{\rho} ([\nabla \cdot \mathcal{T}]_\phi - \nabla_\phi P) - \nabla_\phi \Phi_\star. \quad (2.9)$$

Equation (2.1) gives that $\nabla_\phi \Phi_\star = 0$, and under disk axisymmetry $\partial_t v_\phi = 0$ and $\nabla_\phi P = 0$. The ϕ components of the remaining terms are given by

$$[(\mathbf{v} \cdot \nabla) \mathbf{v}]_\phi = v_r \frac{dv_\phi}{dr} + \frac{v_\phi v_r}{r}, \quad (2.10)$$

$$[\nabla \cdot \mathcal{T}]_\phi = \frac{1}{r^2} \partial_r (r^2 T_{r\phi}) + \partial_z T_{\phi z}, \quad (2.11)$$

giving

$$\rho v_r \frac{dh}{dr} = \frac{1}{r} \partial_r (r^2 T_{r\phi}) + r \partial_z T_{\phi z}, \quad (2.12)$$

where we have substituted Equation (2.2) and multiplied through by $r\rho$. Assuming that $T_{\phi z}$ vanishes as $z \rightarrow \pm\infty$, we can integrate out the ϕ and z dependence to find

$$2\pi \frac{dh}{dr} r v_r \Sigma = \partial_r \left(r^2 \int_0^{2\pi} \int_{-\infty}^{\infty} T_{r\phi} dz d\phi \right). \quad (2.13)$$

For a thin disk the $T_{r\phi} = \mu r d\Omega/dr$ where μ is the fluid viscosity (see review by Papaloizou and Lin, 1995). We then define the *kinematic viscosity* ν as

$$\nu \equiv \frac{1}{2\pi\Sigma} \int_0^{2\pi} \int_{-\infty}^{\infty} \mu dz d\phi. \quad (2.14)$$

Equation (2.13) then becomes

$$\Sigma v_r \frac{dh}{dr} = \frac{1}{r} \partial_r \left(\Sigma r^3 \nu \frac{d\Omega}{dr} \right), \quad (2.15)$$

which expresses total angular momentum conservation for a thin accretion disk governed by internal forces (Pringle, 1981)

2.2 Theoretical Structure

2.2.1 Vertical density structure

The vertical density structure of the disk is derived following the seminal review by Pringle (1981). Assuming v_z to be negligible, the z component of the momentum Equation (2.4) gives

$$\frac{1}{\rho} \partial_z P = -\partial_z \Phi_\star, \quad (2.16)$$

which expresses vertical hydrostatic equilibrium. Assuming that the pressure is gas-dominated (radiation pressure should be negligible for circumstellar disks), and assuming a locally isothermal equation of state $P = c^2 \rho$ where c is the sound speed⁴, we find

$$\frac{c^2}{\rho} \partial_z \rho = -\frac{GM_\star z}{(r^2 + z^2)^{3/2}} \simeq -\Omega_K^2 z. \quad (2.17)$$

⁴Recently this approximation has been criticised as we have begun to observationally constrain the vertical temperature structure of circumstellar disks, see for example Pinte et al. (2018a) and Calahan et al. (2021).

where the approximate equality relies on the condition that $z \ll r$. Equation (2.17) is solved by

$$\rho(r, z) = \rho_0(r) \exp\left(-\frac{z^2}{2H^2}\right), \quad (2.18)$$

where $\rho_0(r)$ is the density in the mid-plane at $z = 0$, and we define the disk *scale height*

$$H \equiv \frac{c}{\Omega_K}. \quad (2.19)$$

Equation (2.18) expresses that the vertical density structure is essentially Gaussian, with a standard deviation given by the scale height H . We can also find the relationship between Σ and ρ for this structure by integrating Equation (2.18) over all z , giving

$$\rho_0(r) = \frac{1}{\sqrt{2\pi}H} \Sigma(r). \quad (2.20)$$

2.2.2 Rotation

Now taking the radial component of the momentum Equation (2.4), assuming axisymmetry, neglecting viscosity and assuming only small radial motions $v_r \ll v_\phi$, we find

$$\frac{v_\phi^2}{r} = \frac{GM_\star r}{(r^2 + z^2)^{3/2}} + \frac{1}{\rho} \partial_r P \simeq \frac{GM_\star}{r^2} + \frac{1}{\rho} \partial_r P, \quad (2.21)$$

where the approximate equality once again assumes $z \ll r$. Dividing by r and substituting $c^2 = dP/d\rho$ gives

$$\Omega^2 = \Omega_K^2 + \left(\frac{c^2}{r^2}\right) \frac{r}{\rho} \frac{d\rho}{dr}, \quad (2.22)$$

$$= \Omega_K \left[1 + \left(\frac{H}{r}\right)^2 \frac{d \ln \rho}{d \ln r} \right]^{1/2}. \quad (2.23)$$

and so we find that for pressure supported circumstellar disks, Keplerian rotation is a good approximation provided that the disk *aspect ratio* $H/r \ll 1$, with the correction being of order $(H/r)^2$. For circumstellar disks, and indeed for most astrophysical disks, $d \ln \rho / d \ln r$ is negative. This is because both the density and the temperature will typically decrease with disk radius. Thus including the correction results in a smaller Ω and so the true rotation is slightly *sub-Keplerian*.

2.2.3 Disk flaring

The definition of a *flared* accretion disk is one whose aspect ratio fulfils the condition

$$\frac{H}{r} \propto r^\gamma; \quad \gamma > 0, \quad (2.24)$$

such that the scale height H increases with radius at a rate greater than linear $H \propto r^{1+\gamma}$. A *flat* disk then has an aspect ratio independent of radius so $\gamma = 0$. Physically the condition for flaring is related to the effective temperature T_{eff} of the disk. For an ideal gas $c^2 \propto T_{\text{eff}}$ (e.g. Pringle and King, 2007), and so

$$\frac{H}{r} = \frac{c}{r\Omega_K} \propto \frac{T_{\text{eff}}^{1/2}}{r^{-1/2}}. \quad (2.25)$$

All disks irradiated by a central object are flared (Kenyon and Hartmann, 1987) and for passive circumstellar disks modelling suggests that $T_{\text{eff}} \propto r^{-1/2}$ (Chiang and Goldreich, 1997), giving $\gamma \simeq 1/4$. Figure 2.2 shows a scattered light image of the disk around the young star IM Lupi, and the flared nature of the structure is clearly seen in the illuminated top and bottom surfaces of the disk. Equation (2.23) suggests that flared disks become increasingly sub-Keplerian with radius.

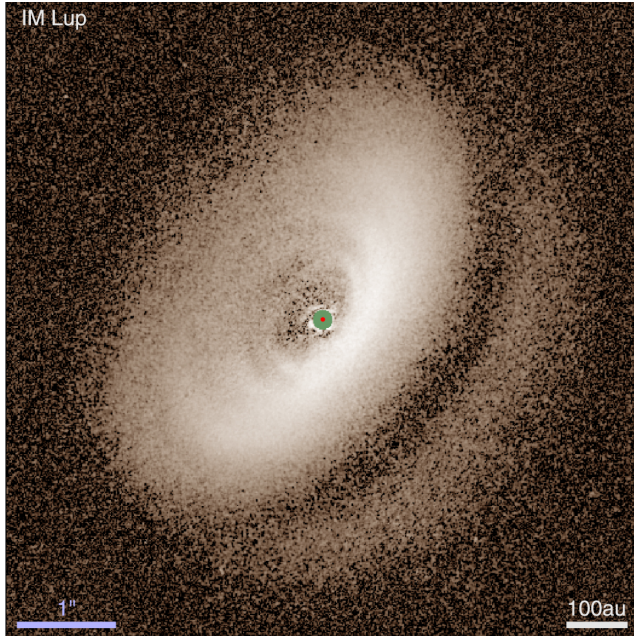


Figure 2.2: H-band image showing the light scattered off the top and bottom surfaces of the disk around the T-Tauri star IM Lupi, taken with the extreme adaptive optics SPHERE instrument at the Very Large Telescope (Avenhaus et al., 2018). The data has been rescaled with a logarithmic stretch to improve contrast. The green dot in the centre of the image corresponds to a region where no data was taken due to the coronagraph, the red dot is the star position. 1 arcsecond and 100 au scales are in the bottom left and right of the image respectively. The disk clearly exhibits the flared structure expected for centrally illuminated disks.

2.3 Viscous Evolution

Combining the mass and angular momentum conservation Equations (2.7) and (2.15), and substituting the Keplerian forms for Ω and h in Equations (2.1) and (2.2), we find

$$\partial_t \Sigma = \frac{3}{r} \partial_r [\sqrt{r} \partial_r (\nu \sqrt{r} \Sigma)], \quad (2.26)$$

which gives the evolution in the surface density for a thin, Keplerian disk. The Equation (2.26) has the form of the one-dimensional heat or diffusion equation, and its diffusive properties are evident in the *ring spreading* solution derived by Lynden-Bell and Pringle (1974) in the case of constant ν . The initial condition for this solution is the Dirac delta centred at $r/r_0 = 1$, representing a thin ring of material orbiting at some radius. The solution is shown in Figure 2.3, and we see that the diffusion results in the movement of a lot of mass to small radii, while small amounts of mass carry angular momentum away to very large radii.

The analysis here and in Section 2.1.1 relies on viscous disk theory as previously stated. In this, we consider that although angular momentum may be physically transferred by mechanisms such as the magnetorotational instability (Sano et al., 2000), self-gravity (Kratter and Lodato, 2016), turbulent eddies (Klahr and Bodenheimer, 2003), or others, we assume that all of the physics can be captured by the kinematic viscosity ν . Modelling disk evolution accurately therefore relies on determining the value of ν . Shakura and Sunyaev (1973) argued that it is physically consistent to parametrise the viscosity in terms of some constant $\alpha \lesssim 1$ as⁵

$$\nu = \alpha c H. \quad (2.27)$$

This is known as the α -prescription. If $\nu \propto r^\beta$ for some constant real number β , then Equation (2.26)

⁵Strictly there is also a factor of 2/3 on the right-hand side but this is typically ignored in the literature and absorbed into the value of α .

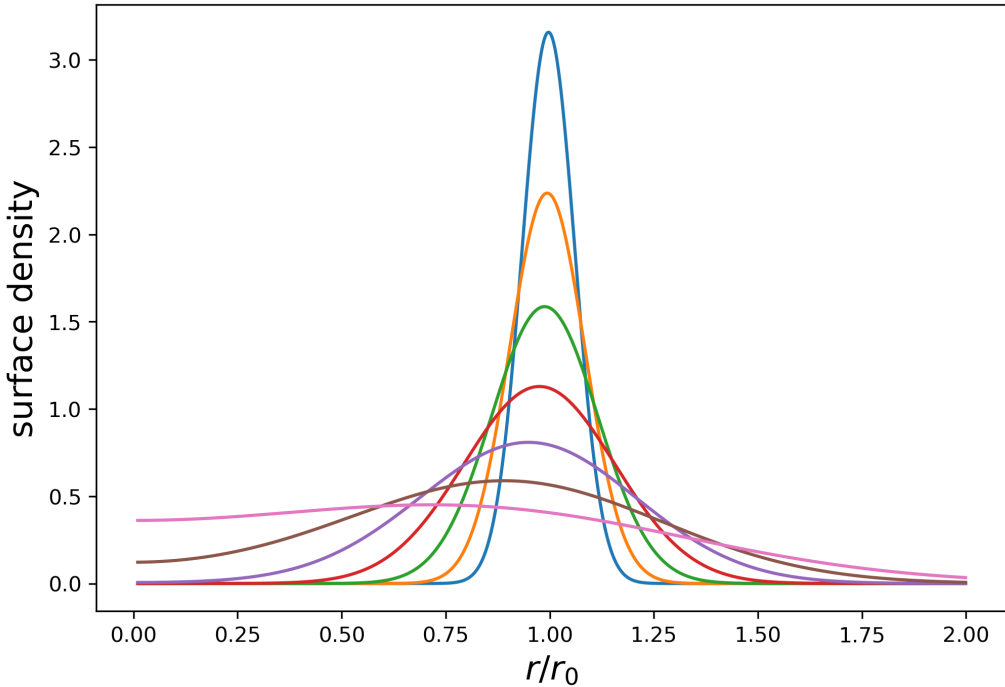


Figure 2.3: The evolution of a ring of gas centred initially at $r = r_0$ according to Equation (2.26), as derived by Lynden-Bell and Pringle (1974). Each curve is plotted from $\tau = 0.008$ to $\tau = 0.512$ with interval 0.084, where τ is dimensionless time (figure from lecture notes by Armitage, 2022). The diffusive nature of the evolution is clearly evident, with the overdense ring spreading out over time.

has solution (Lynden-Bell and Pringle, 1974)

$$\Sigma(r) = (2 - \beta) \frac{M_d}{2\pi r_c^2} \left(\frac{r}{r_c} \right)^{-\beta} \exp \left[- \left(\frac{r}{r_c} \right)^{2-\beta} \right], \quad (2.28)$$

which is a so-called *exponentially tapered* power law in Σ . That is, the density roughly obeys a negative power law with index $-\beta$ at radii less than the critical radius r_c , while dropping off exponentially at radii greater than r_c . Using the α -prescription and the definition of γ given in Equation (2.24) gives $\beta = 2\gamma + \frac{1}{2}$. More commonly this is parameterised in terms of the effective temperature profile or the sound speed profile $T \propto c^2 \propto r^{-2q}$ for some constant real number q , yielding $\beta = \frac{3}{2} - 2q$ (Hartmann et al., 1998). If we take $q = 1/4$ as in Section 2.2.3, then $\beta = 1$ (Chiang and Goldreich, 1997).

The exponentially tapered power law picture for the surface density profile (2.28), combined with the vertically Gaussian density structure (2.18), provide the typical parameterisation used to fit the density structure of observed disks (Andrews et al., 2011; Zhang et al., 2021). The high-resolution MAPS survey found remarkably consistent best fitting parameters of $\beta = 1$ and $\gamma = 0.2$, with variation of only $\simeq 20\%$ and $\simeq 10\%$ respectively across the 5 disks in the sample.

2.4 Observed Properties

2.4.1 Components

Figure 2.4 presents a cartoon overview of the modern understanding of the structural components of protoplanetary disks (Andrews, 2020). The disk is comprised of both gas and dust, where dust is taken to mean any solid material. The gas component is pressure supported and so exhibits the expected flared structure discussed in Section 2.2.3. The dust grains however do not feel any pressure and their behaviour depends on their size. Small dust grains, those on the order of a few microns or less, couple strongly to the gas and thus trace the gas structure. Larger grains experience drag forces and thus settle to the disk mid-plane (Weidenschilling, 1977a). These different components are probed

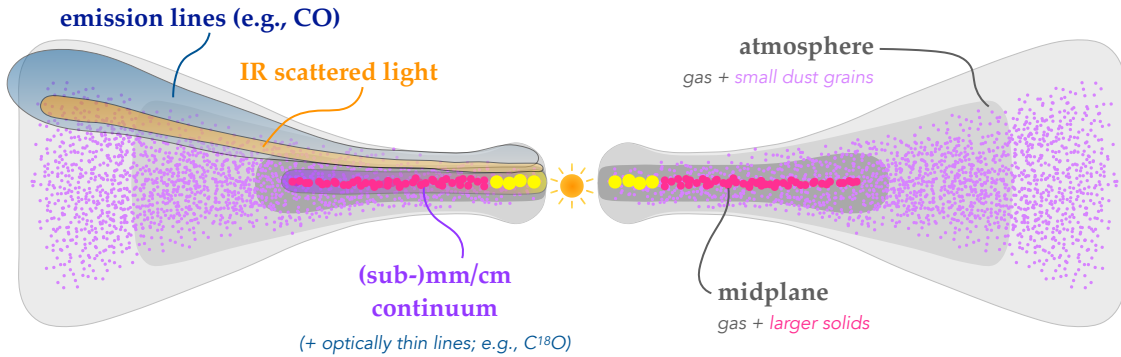


Figure 2.4: A cross section schematic of a typical protoplanetary disk. The location of gas is shown in grey while dust grains and larger solids are shown in purple. Labels on the left outline key observational tracers of disk structure while the labels on the right identify the corresponding features probed. The figure is intended as a rough outline and is not to scale (see review by [Andrews, 2020](#)). The pressure support of the gas results in a thick disk extended in the vertical direction, while the large dust grains settle to a thin layer in the mid-plane.

via different observational tracers. The distribution of small dust grains may be examined through scattered light, while the larger grains can be traced with millimetre thermal continuum observations ([ALMA Partnership et al., 2015](#); [Andrews et al., 2016](#); [Ansdell et al., 2016](#)). The gas component on the other hand may be studied through spectral emission lines of different molecules. These kinds of observations can be used to constrain the gas gas distribution ([van der Marel et al., 2015](#); [Ansdell et al., 2016](#); [Zhang et al., 2021](#)), kinematics ([Perez et al., 2015](#); [Pinte et al., 2018b](#); [Teague et al., 2018](#); [Pinte et al., 2019](#); [Yu et al., 2021](#); [Calcino et al., 2022](#)) and temperature ([Pinte et al., 2018a](#); [Calahan et al., 2021](#)).

2.4.2 Size

The size of a disk is typically defined as the radius within which 90% of the total luminosity is contained. This is in general a function of the observational tracer and so for example R_{mm} may be different to R_{CO} , where the subscripts signify millimetre continuum and molecular carbon monoxide (CO) line emission respectively. Furthermore, each of these sizes may be used as a proxy for the size of a certain component of the disk based on what the component of the disk it probes. Thus R_{mm} is essentially the size of the dust disk comprised of millimetre sized grains and larger, while R_{CO} gives the size of the gas disk. In general the size of the dust disk is smaller than the gas disk for the same system, as demonstrated in Figure 2.5. Medium resolution population studies that resolved almost 200 disks to scales of 25 – 50 au suggest that the typical dust disk size is in the $\simeq 10 - 250$ au ([Tripathi et al., 2017](#); [Andrews et al., 2018b](#); [Hendler et al., 2020](#)). This range is supported by surveys of many fewer disks, around 30, taken at the much higher resolution of ~ 5 au ([Long et al., 2018](#); [Huang et al., 2018a](#)). The gas disks are typically larger with radii of 100 – 500 au, with a few extending out even farther ([Ansdell et al., 2018](#); [Zhang et al., 2021](#)).

2.4.3 Mass

Observational disk mass measurements are something of a problem child. We split the total disk mass M_d into two components, the gas mass M_g and the dust or solids mass M_s where $M_d = M_g + M_s$. Measurements of M_s rely on assumptions of the optical properties of dust grains and so are intrinsically uncertain. M_g measurements are even worse off. Molecular hydrogen is too faint in disks to be of use, no instruments operating or planned can observe the hydrogen deuteride 1 – 0 transition that may be of use, and most other molecules are not very abundant. CO is the next most abundant molecule after H_2 and is readily detectable at wavelengths available to ALMA. Measurements of M_g via CO are unfortunately complicated by uncertainty in the C/H ratio in disks (see the review by [Miotello](#)

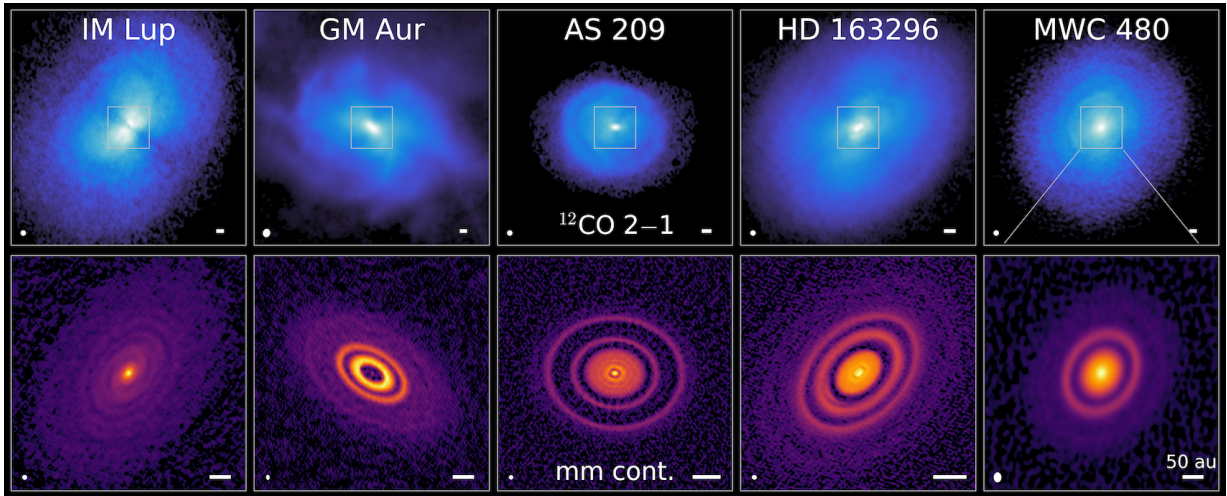


Figure 2.5: Top row: ^{12}CO 2 – 1 Line emission integrated intensity images taken of the five protoplanetary disks as part of MAPS (Öberg et al., 2021). The bottom row shows continuum millimetre observations of the same disks, zoomed in on the box shown on each figure in the top row (Andrews et al., 2018a; Huang et al., 2020; Öberg et al., 2021). We see that in each case the spatial extent of the dust disk probed in mm is much less than that for the gas disk probed with ^{12}CO . Figure retrieved from <https://www.alma-maps.info/disks.html>.

et al., 2022, for in-depth discussion of difficulties with disk mass measurements).

These measurements are crucial to understanding planet formation as they constrain the possible bodies that may be created from a disk as it continues to evolve. The *Minimum Mass Solar Nebula* (MMSN) is the hypothesised disk that the solar system formed from, with just enough mass to create each of the planets (Hayashi, 1981). Modern measurements place the MMSN at $M_s \gtrsim 40 M_{\oplus}$ (where M_{\oplus} is an Earth mass), $M_g \gtrsim 3000 M_{\oplus}$, where M_{\oplus} is an Earth mass (see review by Andrews, 2020). If planets are formed from protoplanetary disks then the mass of said disks should be comparable to, or larger than, the MMSN. Figure 2.6 shows the distribution of dust mass measurements for disks in the regions of Ophiuchus, Lupus, Upper Scorpius, Chamaeleon I, σ Ori, IC 348 and Taurus (Cieza et al., 2019, and references therin), compared with the MMSN. Even in the youngest regions of the sample, fewer than 20% of the disks contain a dust mass greater than the MMSN value of $M_s \gtrsim 40 M_{\oplus}$. This result does not seem to be compatible with the known population of exoplanets, a conundrum known as the *missing mass problem* (e.g. Najita and Kenyon, 2014).

One possible resolution to the missing mass problem is that protoplanetary disks are planet-hosting disks rather than planet-forming disks. In this scenario planet formation occurs during the protostellar stage while the star is still embedded in a envelope, since massive disks are more common (Greaves and Rice, 2010). This scenario is supported by the growing body of evidence that protoplanetary disks contain planets when the system is as young as 1-2 Myr (ALMA Partnership et al., 2015; Zhang et al., 2018; Verriros et al., 2022). On the other hand planet formation may be incredibly efficient during the very early protoplanetary stage (Najita and Kenyon, 2014; Manara et al., 2018; Tychoniec et al., 2020). A final possibility is that derived dust disk masses suffer from systematic underestimation. Zhu (2019) argued that if disks are not optically thin, as assumed in calculations of disk mass from continuum observations, then the true dust mass may be a factor of 2 or more larger. Whatever the case may be, it is likely that detecting young planets and constraining their masses through kinematic observations will be a key part of determining which scenario is correct.

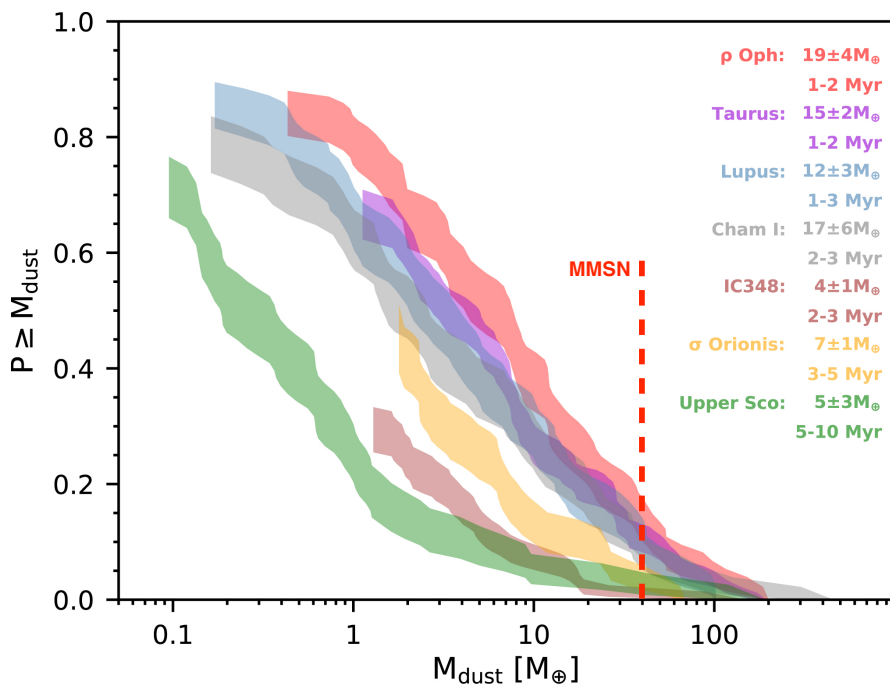


Figure 2.6: Cumulative mass distributions for disks found in various nearby young stellar regions. The shaded regions represent the 1σ confidence intervals (van Terwisga et al., 2019). Plotted in red is the dust mass of the MMSN (Weidenschilling, 1977b). According to this analysis, very few of the disks in the sample have enough mass to create the planets of the solar system.

3

Planet-Disk Interaction

The tidal forces induced by a planet embedded in a gas disk result in the excitation of sound waves ([Goldreich and Tremaine, 1980](#)). These waves propagate freely through the disk, interfering with one another and eventually steepening into shock waves ([Goodman and Rafikov, 2001](#)). The overall result is the formation of a coherent, one-armed spiral density wave connected to the planet, known as the *planet wake* ([Ogilvie and Lubow, 2002](#)). This chapter provides an outline of the theory behind this interaction, and introduces the method with which we will go on to construct semi-analytic models of the planet wake. These ideas also provide the necessary foundation that will allow us to go on to detecting and measuring young planets through kinematic observations.

3.1 Spiral Density Waves

Perhaps the most well known examples of spiral structures in astrophysics are the grand design spirals of galaxies like Messier 81 (M81), shown in Figure 3.1. The disk of a galaxy rotates differentially, similarly to a circumstellar disk, resulting in an initially puzzling state of affairs. If the material making up the spiral structure remains in the arm, then the pattern should be quickly destroyed since material in the inner disk orbits at a much greater rate than that in the outer disk. This is known as the *winding problem*, and it proved to be a serious challenge for early attempts to explain spiral structure in galaxies ([Wilczynski, 1896](#); [Oort, 1962](#)).

The first major advance in our understanding of the origins of galactic spiral structure was made by Bertil Lindblad in the early 1960s. Lindblad proposed that spiral structure may be a quasi-stationary wave resulting from the superposition of multiple spiral modes. In Lindblad's model, these modes were excited through the interaction of orbital motions and gravitational forces of the stars in the disk ([Lindblad, 1963](#)). This was a radical view at the time, as it was widely believed that spiral structure was induced by galactic-scale magnetic fields (e.g. [Hoyle and Ireland, 1961](#); [Öki et al., 1964](#)). The paradigm-shift would come shortly after with the seminal work by [Lin and Shu \(1964\)](#), pioneering the *density wave theory* picture of spiral structure. In their view, spiral arms are quasi-static overdense regions of the disk resulting from periodic compression and rarefaction of disk material, similar to a traffic jam. This, in combination with Lindblad's findings make up the *Lin-Shu Hypothesis*, which states that galactic spiral structure is a stationary density wave, and that the spiral pattern is unchanged over long timescales apart from the overall rotation of the galaxy. A more precise statement of the hypothesis is that the spiral is a marginally stable wave mode of the disk.

The Lin-Shu hypothesis is however not correct ([Toomre, 1969](#); [Dobbs and Baba, 2014](#)) The spiral structure found in galaxies is indeed a density wave, but the wave is not a stationary, stable mode of the disk. Instead the spiral arms are the result of the disk responding to a variety of gravitational disturbances such as nearby galaxies ([Goldreich and Lynden-Bell, 1965](#); [Julian and Toomre, 1966](#)).



Figure 3.1: Long exposure image of Messier 81 taken through a 20 inch telescope by astrophotographer Michael Adler with LRGB filters, and a Hydrogen- α filter that was assigned to red. Overall 20 hours of exposures were taken. Image taken from https://commons.wikimedia.org/wiki/File:Bode%27s_Galaxy.jpg.

Indeed, the grand design spirals in M81 are thought to be the result of tidal-interactions with its companion galaxy Messier 82 (Yun, 1999).

Spiral arms similar to those found in galaxies have been observed in the disks around the stars HD 142529 (Christiaens et al., 2014), MWC 758 (Benisty et al., 2015), Elias 27 (Pérez et al., 2016; Huang et al., 2018b), IM Lupi (Avenhaus et al., 2018; Huang et al., 2018b), WaOph 6 (Huang et al., 2018b), HD 163296 (Calcino et al., 2022), TW Hya (Teague et al., 2022) and others (Dong et al., 2018, and references therin). Figure 3.2 shows the double-armed spiral of MWC 758 in scattered light. The origin of most of these spirals is still unknown (e.g. Zhang et al., 2018). Of particular interest to us here are kinematic detections of planets located inside dust gaps (Pinte et al., 2018b, 2019, 2020; Teague et al., 2021, 2022), since they are well explained by the planet wake scenario, as we will see.

3.1.1 Spiral structure preliminaries

We now introduce the following concepts:

1. The *pitch angle* α : of a spiral arm is defined as the angle between the tangent to the spiral at some radius r and the circle with the same radius. Thus α is in general a function of radius and $0 < \alpha < \pi/2$ by definition.
2. *m-fold rotational symmetry*: if a rotation of $2\pi/m$ radians results in no change to the disk surface density, that is $\Sigma(r, \phi) = \Sigma(r, \phi + \frac{2\pi}{m})$, then the disk is said to contain m spiral arms and exhibits an m -fold rotational symmetry. For example, a disk containing two spiral arms will be unchanged under a rotation of 180° and so has 2-fold rotational symmetry.
3. *Leading* and *trailing* spiral arms: the tip of a leading spiral arm points in the direction of the bulk rotation of the disk, while the tip of a trailing arm points in the opposite direction to the rotation. While it seems that leading arms may indeed be physically realised in the universe (e.g. Väistönen et al., 2008), they are at minimum very rare. We will be concerned only with trailing spirals in this thesis.

Consider a disk containing a set of m spiral arms such that it has m -fold symmetry. We may

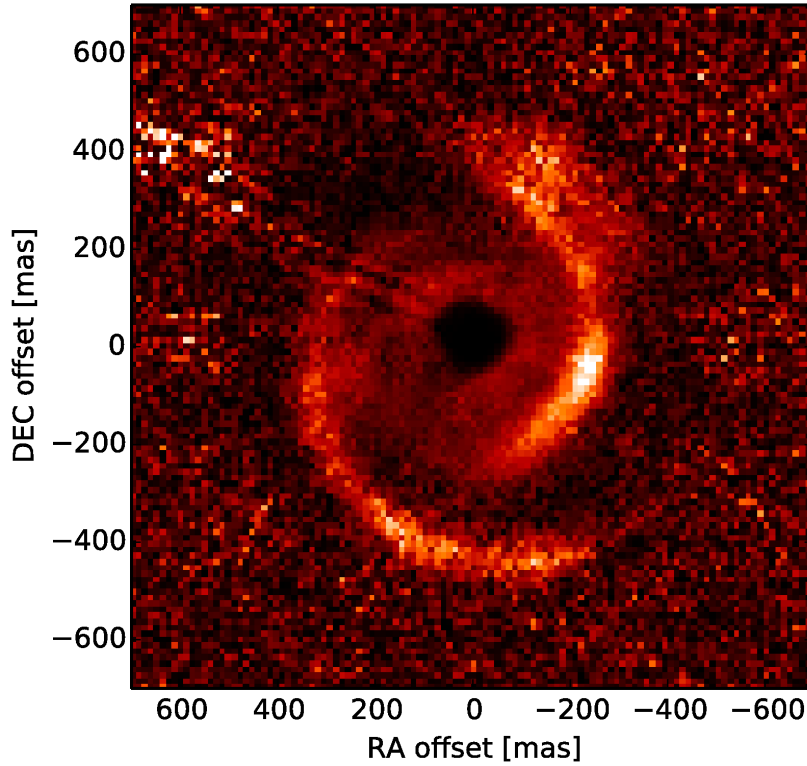


Figure 3.2: Polarised intensity image of the disk MWC 758 obtained in December 2014 with SPHERE (e.g. Beuzit et al., 2019). The colour scale is arbitrary. Two large spiral arms are clearly present in the disk (Benisty et al., 2015). The origin of these spiral arms is still unknown.

parameterise the curves defined by the centre of each of the spiral arms as

$$m\phi + f(r, t) = C \bmod 2\pi, \quad (3.1)$$

where C is a constant real number and f is known as the *shape function*. The *radial wavenumber* k is defined in terms of f and is given by

$$k(r, t) \equiv \partial_r f(r, t). \quad (3.2)$$

For a counter-clockwise rotating disk we have $m > 0$ and so $k > 0$ corresponds to trailing arms while $k < 0$ gives leading arms. The opposite is true for clockwise rotating disks with $m < 0$. We will always assume both k and m are positive, corresponding to tailing arms in a counter-clockwise rotating disk. The pitch angle α of a spiral arm is given by

$$\cot \alpha = |r \partial_r \phi|, \quad (3.3)$$

where $r \partial_r \phi$ is evaluated along the curve that defines the spiral. In terms of the parameterisation (3.1) we have $\partial_r[m\phi + f(r, t)] = m\partial_r \phi + k = 0$ giving

$$\alpha = \arctan \left(\frac{m}{kr} \right). \quad (3.4)$$

3.1.2 No leading spirals

In the previous section we stated that while leading spirals may exist in nature, they are at least much rarer than trailing spirals; there are **no** known examples of leading spirals in circumstellar disks. This is at least initially surprising. If the trailing spiral arms seen in astrophysical disks are steady-state solutions governed by Newtonian physics, which is fully time-reversible, surely the corresponding leading spirals solution is entirely equivalent? Lynden-Bell and Ostriker (1967) followed this argument to prove the *anti-spiral* theorem, which states that if trailing spirals constitute a steady-state solution

to time-reversible equations, then there necessarily exists an equivalent leading spiral solution. Thus the apparent ubiquity of trailing spirals in nature tells us that either the governing physics is not time-reversible, or the spirals are not true steady-state solutions. In the latter case spiral structure may be the result of a recent disturbance, or may be continuously regenerated for example by period tidal forcing. This mimics the failing of the Lin-Shu hypothesis for galaxies, where spiral structure turned out to be the response of the disk to disturbances (Julian and Toomre, 1966). In Section 3.3 we will see that the perturbations driven periodically by a gravitating body embedded in a circumstellar disk result in a trailing spiral structure.

3.2 The Linear Disk Response

Before determining how the periodic forcing of the planet potential perturbs the disk, we must first determine how the disk responds to some small, generic disturbance. The 2D inviscid equations of momentum and continuity expressed in terms of surface density are given by (Landau and Lifshitz, 1987)

$$\partial_t u + u \partial_r u + \frac{v}{r} \partial_\phi u - \frac{v^2}{r} = -\partial_r \Phi - \frac{1}{\Sigma} \partial_r P, \quad (3.5)$$

$$\partial_t v + u \partial_r v + \frac{v}{r} \partial_\phi v - \frac{uv}{r} = -\frac{1}{r} \partial_\phi \Phi - \frac{1}{r\Sigma} \partial_\phi P, \quad (3.6)$$

$$\partial_t \Sigma + \frac{1}{r} \partial_r(r\Sigma u) + \frac{1}{r} \partial_\phi(\Sigma v) = 0, \quad (3.7)$$

where u and v are the radial and azimuthal velocity components⁶. Assuming a polytropic equation of state

$$P = K\Sigma^\gamma, \quad (3.8)$$

where K is a constant and γ is the adiabatic index. We then find the sound speed c to be

$$c^2 = \partial_\Sigma P = \gamma K \Sigma^{\gamma-1}. \quad (3.9)$$

To simplify the equations we introduce the specific enthalpy h . Since the equation of state we are using is isentropic, we have $dh = dP/\Sigma$ giving

$$h = \int \frac{1}{\Sigma} dP = \int \frac{c^2}{\Sigma} d\Sigma = \frac{\gamma}{\gamma-1} K \Sigma^{\gamma-1}. \quad (3.10)$$

Note that

$$\partial_x h = \frac{\gamma}{\gamma-1} K \partial_\Sigma (\Sigma^{\gamma-1}) \partial_x \Sigma = \gamma K \Sigma^{\gamma-2} \partial_x \Sigma, \quad (3.11)$$

such that the right-hand sides of Equations (3.5) and (3.6) become

$$-\partial_r \Phi - \frac{1}{\Sigma} \partial_r P = -\partial_r \Phi - \gamma K \Sigma^{\gamma-2} \partial_r \Sigma = -\partial_r(\Phi + h), \quad (3.12)$$

and

$$-\frac{1}{r} \partial_\phi \Phi - \frac{1}{r\Sigma} \partial_\phi P = -\frac{1}{r} \partial_\phi(\Phi + h), \quad (3.13)$$

respectively.

We now perform a linear perturbation study; we assume that the spiral waves in the disk constitute only a small perturbation from some background steady-state, and that the background state is axisymmetric. We rewrite the quantities Σ, Φ, h, u, v as a combination of the background value (denoted

⁶Later we will use the same symbols to denote perturbations, but it should be clear which we mean from context.

by subscript 0) and a small perturbation (denoted by δ)

$$\Sigma = \Sigma_0 + \delta\Sigma, \quad (3.14)$$

$$\Phi = \Phi_0 + \delta\Phi, \quad (3.15)$$

$$h = h_0 + \delta h, \quad (3.16)$$

$$v = v_0 + \delta v, \quad (3.17)$$

$$u = \delta u, \quad (3.18)$$

where we note that $u_0 = 0$ since we assume no radial motion in the background state. From Equations (3.5) and (3.12), and making use of the axisymmetry of the background state, we find the equation of motion for the background

$$\frac{v_0^2}{r} = \partial_r (\Phi_0 + h_0), \quad (3.19)$$

which is the 2D equivalent of Equation (2.23). Substituting (3.14)-(3.18) into Equations (3.5), (3.6), (3.12), (3.13), discarding second order terms, and subtracting Equation (3.19) yields the linearised equations of motion

$$\partial_t \delta u + \Omega \partial_\phi \delta u - 2\Omega \delta v = -\partial_r (\delta\Phi + \delta h), \quad (3.20)$$

$$\partial_t \delta v + \Omega \partial_\phi \delta v - 2B \delta u = -\frac{1}{r} \partial_\phi (\delta\Phi + \delta h), \quad (3.21)$$

where we have also substituted $v_0 = \Omega r$ and the second Oort constant $B = -r\partial_r\Omega/2 - \Omega$, which is related to the epicyclic frequency as $\kappa^2 = -4B\Omega$. The linearised equation of continuity is obtained similarly from Equation (3.7)

$$\partial_t \delta\Sigma + \frac{1}{r} \partial_r (r\Sigma_0 \delta u) + \frac{\Sigma_0}{r} \partial_\phi \delta v + \Omega \partial_\phi \delta\Sigma. \quad (3.22)$$

We assume that the equations of motion (3.20) and (3.21) are solved by a summation of plane waves, where each perturbed quantity $a \in \{\Sigma, \Phi, h, v, u\}$ can be written as

$$\delta a = \sum_m \delta a_m = \sum_m a_m(r) \exp[i(m\phi - \omega t)]; \quad m \in \mathbb{Z}^{0+}, \quad (3.23)$$

where each m component of the perturbation has m -fold symmetry and $a_m(r)$ is in general a complex function. The physical perturbation is obtained by taking the real component $\text{Re}(\delta a)$. Substituting the summands of (3.23) in place of the perturbations in our linearised equations yields

$$u_m(r) = \frac{i}{\Delta_m} \left[(\omega - m\Omega) \partial_r (\Phi_m + h_m) - \frac{2m\Omega}{r} (\Phi_m + h_m) \right], \quad (3.24)$$

$$v_m(r) = -\frac{1}{\Delta_m} \left[2B \partial_r (\Phi_m + h_m) + \frac{m(\omega - m\Omega)}{r} (\Phi_m + h_m) \right], \quad (3.25)$$

$$\Sigma_m(r) = \frac{1}{r(\omega - m\Omega)} [m\Sigma_0 v_m - i\partial_r(r u_m \Sigma_0)], \quad (3.26)$$

where

$$\Delta_m \equiv \kappa^2 - (\omega - m\Omega)^2. \quad (3.27)$$

Finally, we must linearise the equation of state. Taking Equation (3.10) and expanding in $\delta\Sigma/\Sigma_0$

$$h_0 + \delta h = \frac{\gamma}{\gamma - 1} K \Sigma_0^{\gamma-1} \left(1 + \frac{\delta\Sigma}{\Sigma_0}\right)^{\gamma-1} = \frac{\gamma}{\gamma - 1} K \Sigma_0^{\gamma-1} + \gamma K \Sigma_0^{\gamma-1} \frac{\delta\Sigma}{\Sigma_0} + \mathcal{O}((\delta\Sigma/\Sigma_0)^2). \quad (3.28)$$

Now substituting Equations (3.9) and (3.10), and taking only one component of the perturbation, we find

$$h_m \simeq c_0^2 \frac{\Sigma_m}{\Sigma_0}, \quad (3.29)$$

where c_0 is the unperturbed sound speed.

With Equations (3.24), (3.25), (3.26) and (3.29) we have four constraints on the five state variables $\Sigma_m, \Phi_m, h_m, v_m$ and u_m . We therefore now have a system of equations describing the *linear response* of the disk Σ_m for the azimuthal wave mode m , to the potential component Φ_m . By summing over all modes, we can calculate the *global* response of the disk to some imposed gravitational potential. This however, cannot be done analytically.

3.2.1 Tightly-wound density waves

We now apply *WKB approximation*, which will allow to find *local* analytic solutions. For spiral density waves this is equivalent to assuming that the spirals are *tightly-wound* and thus is also called the *tight-winding approximation*. For a spiral with shape function f let λ_r be the radial separation between adjacent arms for fixed ϕ , such that

$$2\pi = |f(r + \lambda_r, t) - f(r, t)|. \quad (3.30)$$

If we assume that the spirals are indeed tightly-wound such that $\alpha \rightarrow 0$, then we have that $f(r + \lambda_r, t) = f(r, t) + \lambda_r \partial_r f|_{r,t}$. Recalling that $\partial_r f|_{r,t}$ is none other than the radial wavenumber k , we find

$$2\pi = |f(r, t) + \lambda_r \partial_r f|_{r,t} - f(r, t)|, \quad (3.31)$$

$$= \lambda_r |k|, \quad (3.32)$$

$$\Rightarrow \lambda_r = \frac{2\pi}{|k|}, \quad (3.33)$$

and so we find that the radial wavenumber r has the usual relationship with the radial wavelength λ_r . Substituting Equation (3.4) gives

$$\frac{\lambda_r}{r} = \frac{2\pi}{|rk|} = \frac{2\pi \tan \alpha}{m}, \quad (3.34)$$

and so an equivalent condition for the tight-winding approximation is that $|rk| \gg 2\pi$. This equivalency however does not hold for very large m since the right-hand side above can then approach zero regardless of α , and is also invalid for $m = 0$ i.e. purely radial perturbations.

3.2.2 Perturbed potential under WKB

We can write the perturbed spiral surface density for some mode m in a form similar to (3.23) where we instead separate the rapid variations in density moving from one arm to another, and the slower variation while moving along a particular arm

$$\delta\Sigma_m = \Sigma_m \exp [i(m\phi + f(r, t))]. \quad (3.35)$$

To determine the disk response we must find the gravitational potential due to this perturbed surface density, which is done by solving Poisson's equation

$$\nabla^2 \delta\Phi_m = 4\pi G \delta\Sigma_m \delta(z), \quad (3.36)$$

where $\delta(z)$ is the Dirac delta since we assume the disk is infinitely thin. The solution under the WKB approximation is (e.g. [Binney and Tremaine, 2008](#))

$$\delta\Phi_m = -\frac{2\pi G}{|k|} \Sigma_m \exp [i(m\phi + f(r, t))], \quad (3.37)$$

$$\Rightarrow \Phi_m = -\frac{2\pi G}{|k|} \Sigma_m. \quad (3.38)$$

3.2.3 The Lin-Shu dispersion relation

We now rewrite each coefficient $a_m(r)$ for each term δa_m of some perturbed quantity δa as

$$a_m(r) = A_m(r) \exp [if(r)] = A_m(r) \exp \left[i \int^r k(r') dr' \right], \quad (3.39)$$

where, similarly to (3.35), $F(r)$ is a slowly varying function of radius and the exponential encapsulates more rapid variations. The radial derivative of a_m is then

$$\partial_r a_m(r) = (\partial_r A_m + ikA_m) \exp \left[i \int^r k(r') dr' \right]. \quad (3.40)$$

Under the WKB approximation we have $|kr| \gg 2\pi$. Since $A_m(r)$ is a smoothly varying function of r , $|\partial_r A_m| \sim \mathcal{O}(A_m/r)$, yielding $\partial_r A_m \ll |kA_m|$. We therefore neglect the first term above, giving

$$\partial_r a_m(r) = ikA_m \exp \left[i \int^r k(r') dr' \right] + \mathcal{O} \left(\frac{1}{|kr|} \right) \approx ika_m(r). \quad (3.41)$$

Thus assuming the form (3.39) for the quantities in Equations (3.24) - (3.26) and applying the WKB approximation yields

$$u_m(r) = -\frac{k(\omega - m\Omega)}{\Delta_m} (\Phi_m + h_m), \quad (3.42)$$

$$v_m(r) = -\frac{2ikB}{\Delta_m} (\Phi_m + h_m), \quad (3.43)$$

$$\Sigma_m(r) = \frac{k\Sigma_0}{\omega - m\Omega} u_m, \quad (3.44)$$

where the error is for all cases $\mathcal{O}(1/|kr|)$, as we have approximated the radial derivatives by (3.41) and dropped terms proportional to $1/r$ in favour of terms proportional to k . Finally, we may combine Equations (3.29), (3.38), (3.42) and (3.44) to find the dispersion relation for tightly-wound density waves in a rotating gas disk

$$(\omega - m\Omega)^2 = \kappa^2 - 2\pi G|k|\Sigma_0 + c_0^2 k^2. \quad (3.45)$$

This result is known as the *Lin-Shu Dispersion Relation* (Lin and Shu, 1964).

3.2.4 Stability

If the right-hand side of the Lin-Shu dispersion relation (3.45) is negative, that is $(\omega - m\Omega)^2 < 0$, then ω will become imaginary resulting in the exponential growth of the density perturbation $\delta\Sigma$. By requiring that $(\omega - m\Omega)^2 > 0$ for all possible k , the disk stability criterion Q is derived (Toomre, 1964)

$$Q(r) \equiv \frac{c_0 \kappa}{\pi G \Sigma} > 1. \quad (3.46)$$

Disk regions where $Q(r) < 1$ are subject to local unstable growth for certain values of k . This can result in the fragmentation of the disk, and may be a pathway to the formation of giant planets (Boss, 1997).

3.3 Planet Forcing

Armed with the Lin-Shu dispersion relation that encodes the linear disk response to a disturbance in terms of density wave theory, we are ready to investigate the effects of the gravitational perturbation induced by an embedded planet. This will in turn allow us to study the generation and propagation of the resultant spiral structure.

3.3.1 Lindblad resonances

Let (r, ϕ) be polar coordinates centred on some star with mass M_* . We place a planet of mass $M_p \ll M_*$ on a circular orbit of radius r_p around the star. The angular velocity of the planet Ω_p will be given by

$$\Omega_p^2 = \Omega_K(r_p) = \frac{GM_*}{r_p^3} = \frac{1}{r_p} \left(\frac{d\Phi_*}{dr} \right)_{r_p}, \quad (3.47)$$

where Φ_* is the gravitational potential for a point mass

$$\Phi_* = -\frac{Gm_*}{r}. \quad (3.48)$$

Similarly, the angular velocity of some other test particle on a circular orbit (neglecting the influence of the planet) will be

$$\Omega_0^2 = \frac{1}{r} \frac{d\Phi_*}{dr}. \quad (3.49)$$

Now consider the problem in a rotating frame such that the planet is always at $\phi = 0$, which will remove the time dependence from the planet potential. The corresponding transformation will be given by $\phi \rightarrow \phi - \Omega_p t$. The Lagrangian for a test particle in such a frame is

$$\mathcal{L} = \frac{1}{2} \left[\dot{r}^2 + r^2 (\dot{\phi} + \Omega_p)^2 \right] - \Phi(r, \phi), \quad (3.50)$$

where $\Phi(r, \phi) = \Phi_*(r) + \Phi_p(r, \phi)$ is the total potential from both the star and planet. From the Euler-Lagrange equations we find the equations of motion to be

$$\ddot{r} = r (\dot{\phi} + \Omega_p)^2 - \partial_r \Phi, \quad (3.51)$$

$$r^2 \ddot{\phi} = -2r\dot{r} (\dot{\phi} + \Omega_p) - \partial_\phi \Phi. \quad (3.52)$$

We now perform a perturbation study using the change of variables $r(t) \rightarrow r + \delta r(t)$ and $\phi(t) \rightarrow \phi(t) + \delta\phi(t)$ where we assume that $\delta r \ll r$ and $\delta\phi \ll \phi$. We will similarly assume that $\Phi_p \ll \Phi_*$. Thus the derivatives transform to first order as

$$\partial_r \rightarrow \partial_r + \delta r \partial_r^2 r, \quad (3.53)$$

$$\partial_\phi \rightarrow \partial_\phi + \delta\phi \partial_r^2 \phi. \quad (3.54)$$

The zeroth order terms of (3.51) and (3.52) give

$$r (\dot{\phi} + \Omega_p)^2 = \frac{d\Phi_*}{dr}, \quad (3.55)$$

$$\ddot{\phi} = 0, \quad (3.56)$$

which are just the usual equations for centripetal acceleration. They are solved simply by associating $\dot{\phi}$ appropriately with Ω by considering the transformation to the rotating frame, yielding

$$\dot{\phi} = \Omega - \Omega_p, \quad (3.57)$$

$$\Rightarrow \phi = (\Omega - \Omega_p) t, \quad (3.58)$$

where the constant of integration is set to zero without loss of generality. We are now free to consider in isolation the first order terms of (3.51) and (3.52), which reduce to

$$\ddot{\delta r} + \left(\frac{d^2\Phi_*}{dr^2} - \Omega^2 \right) \delta r = 2r\Omega\dot{\delta\phi} - \partial_r \Phi_p, \quad (3.59)$$

$$\ddot{\phi} + \frac{2\Omega}{r} \dot{\delta r} = -\frac{1}{r^2} \partial_\phi \Phi_p. \quad (3.60)$$

We will now specify a form for the planet potential Φ_p . Starting with the usual point mass potential centred on the planet we have

$$\Phi_p(r, \phi) = -\frac{GM_p}{|\mathbf{r} - \mathbf{r}_p|}, \quad (3.61)$$

$$= -\frac{GM_p}{\sqrt{(r_p - r \cos \phi)^2 + (r \sin \phi)^2}}, \quad (3.62)$$

$$= -\frac{GM_p}{\sqrt{r^2 - 2rr_p \cos \phi + r_p^2}}, \quad (3.63)$$

$$= -\frac{GM_p}{r_p} [\mathcal{R}^2 - 2\mathcal{R} \cos \phi + 1]^{-\frac{1}{2}}, \quad (3.64)$$

where $\mathcal{R} = r/r_p$. To investigate the influence of this potential perturbing our test particles we will decompose it using a Fourier series. The potential must be invariant under $\phi \rightarrow -\phi$ as well as 2π periodic in ϕ , motivating the form⁷

$$\Phi_p(r, \phi) = \sum_{m=0}^{\infty} \Phi_m(r, \phi) = \sum_{m=0}^{\infty} V_m(r) \cos(m\phi), \quad (3.65)$$

where in our case the Fourier coefficients are given by

$$V_m(r) = -\frac{2}{\pi} \frac{GM_p}{r_p} \int_0^\pi (\mathcal{R}^2 - 2\mathcal{R} \cos \phi + 1)^{-\frac{1}{2}} \cos(m\phi) d\phi, \quad (3.66)$$

$$= \frac{\delta_{m0} - 2}{2} \frac{GM_p}{r_p} b_{1/2}^m(\mathcal{R}), \quad (3.67)$$

where $b_{1/2}^m(\mathcal{R})$ are the Laplace coefficients defined in [Brouwer and Clemence \(1961\)](#). Figure 3.3 shows the first m Fourier components of the planet potential Φ_m , where the star is located at the origin and the planet is at the point $(1, 0)$. Each of these components results in the periodic driving of perturbations in the disk, with a period equal to $2\pi/(m\Omega_p)$.

Here we are primarily concerned with the *form* of the decomposition (3.65) which is actually quite general and can represent a variety of potentials including the bars often found in spiral galaxies. Next we will substitute a single Fourier component in place of the planet potential to determine the response for *each individual component*. Note that we will also ignore the contribution of $\delta\phi$ to Φ_p , assuming that ϕ corresponds to the zeroth order solution where $\phi = (\Omega - \Omega_p)t$.

From Equation (3.65) we find the following derivatives

$$\partial_r \Phi_m(r, \phi) = \frac{dV_m(r)}{dr} \cos(m\phi) \quad (3.68)$$

$$\partial_\phi \Phi_m(r, \phi) = -mV_m(r) \sin(m\phi), \quad (3.69)$$

and so Equation (3.60) becomes

$$\ddot{\phi} = -\frac{2\Omega}{r} \dot{\delta}r + \frac{mV_m}{r^2} \sin(m[\Omega - \Omega_p]t), \quad (3.70)$$

and integrating gives

$$\dot{\phi} = -\frac{2\Omega}{r} \delta r - \frac{V_m}{(\Omega - \Omega_p)r^2} \cos(m[\Omega - \Omega_p]t). \quad (3.71)$$

⁷The origin of our chosen coordinates is the centre of the star, but this point will not be the barycentre of the system. Our frame is therefore non-inertial and results in an additional acceleration which is typically included as the gradient of an additional potential contribution, the so-called indirect potential ([Goldreich and Tremaine, 1980](#)). However the contribution is small and so is neglected even in detailed calculations of the linear disk response to tidal forcing by a planet (see for example [Bae and Zhu, 2018; Miranda and Rafikov, 2019](#)).

⁸<https://github.com/SijmeJan/pylaplace>

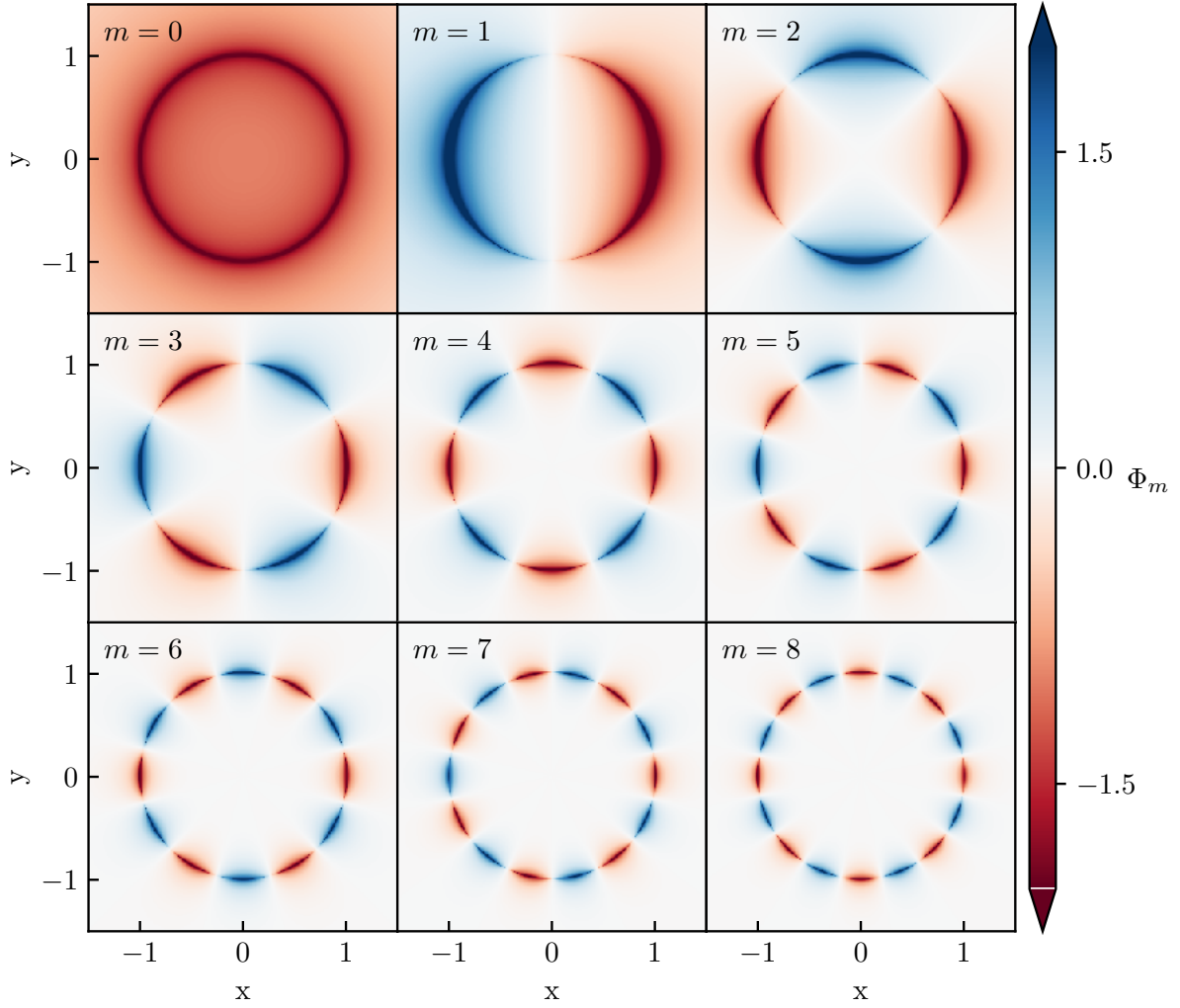


Figure 3.3: The first 9 Fourier components of the planet potential $\Phi_m(r, \phi) = V_m(r) \cos(m\phi)$, where the star is located at $(x, y) = (0, 0)$ and the planet at $(1, 0)$. The units are dimensionless such that $G = M_p = 1$. The Laplace coefficients $b_{1/2}^m$ were calculated using the PYTHON package PYLAPLACE⁸.

Substituting this into (3.59) yields

$$\ddot{\delta r} + \kappa^2 \delta r = \Psi_m(r) \cos(m[\Omega - \Omega_p]t), \quad (3.72)$$

where

$$\kappa^2 \equiv \frac{d^2 \Phi_\star}{dr^2} + 3\Omega^2 = r \frac{d\Omega^2}{dr} + 4\Omega^2, \quad (3.73)$$

is the usual epicyclic frequency already introduced. In addition, we define the forcing function $\Psi_m(r)$ as

$$\Psi_m(r) \equiv - \left(\frac{dV_m}{dr} + \frac{2\Omega}{(\Omega - \Omega_p)r} V_m \right). \quad (3.74)$$

Equation (3.72) is a second order, inhomogeneous differential equation in the form of a driven harmonic oscillator. The general solution $g(t)$ is given by

$$g(t) = A_1 \mathcal{H}(t) + A_2 \mathcal{P}(t), \quad (3.75)$$

where $\mathcal{H}(t)$ is the solution to the homogeneous equation where the right-hand side is zero, $\mathcal{P}(t)$ is a particular solution to the inhomogeneous equation, and A_1 and A_2 are the amplitudes of each.

Physically, $A_1 \mathcal{H}(t)$ corresponds to the “free” solution in the absence of forcing by the planet potential, and a non-zero value of A_1 results in particle orbits that are not closed. $A_2 \mathcal{P}(t)$ corresponds to the driven solution and is what we are interested in here. We solve for the driven solution using the ansatz $\delta r(t) = A \cos(m[\Omega - \Omega_p]t)$, with the result that the amplitude of the response to the planet forcing is given by

$$A = \frac{\Psi_m(r)}{\Delta_m}, \quad (3.76)$$

where Δ_m is as defined in Equation (3.27), and we have $\omega = m\Omega_p$. From this, we see that the forcing amplitude A becomes very large as $\Delta_m \rightarrow 0$. $\Delta_m = 0$ is therefore the condition for a *Lindblad Resonance*; it determines the region where the response to periodic forcing by a particular component of the planet potential is greatest. This is also the condition where the Lin-Shu dispersion relation breaks down as Equations (3.24) and (3.25) become singular.

From Equation (2.23), we have that for material in a gas disk $\kappa = \Omega \approx \Omega_K$. Thus disk material is most effectively excited by the planet potential component Φ_m in the region where

$$\Omega_K^2 = m^2(\Omega_K - \Omega_p)^2. \quad (3.77)$$

By substituting Equation (2.1) we obtain the *Lindblad radii*

$$r_L^\pm(m) = \left(1 \pm \frac{1}{m}\right)^{\frac{2}{3}} r_p, \quad (3.78)$$

which are the positions of the m th Lindblad resonances, where r_L^- is interior to the planets orbit and r_L^+ is exterior to the planets orbit. The Lindblad resonances are spatially segregated but become densely packed near r_p as m becomes large, as shown in Figure 3.4. This segregation allows us to consider each resonance location as driven by only the m th component of the planet potential. This breaks down for large m as the resonances are no longer clearly separated.

The pressure support of the disk results in a slight modification of Ω from Ω_K as seen in Equation (2.23). This results in the radial shifting of the resonance positions (Artynowicz, 1993). Resonance-shifting is important for calculating the total resultant torque on the disk, but affects the structure of excited waves only minimally and so we will ignore it here.

3.3.2 The planet wake

Following closely the work by Ogilvie and Lubow (2002), we will use phase arguments to determine the shape of the planet wake in the linear density wave theory paradigm. However we will not follow exactly their original derivation. We will instead obtain the more general form for the wake shape. Similarly to in Section 3.2.3, we can write linear wave quantities in a 2D gas disk as

$$\delta a_m = A_m(r) \exp i\Theta_m, \quad (3.79)$$

where the amplitude $A_m(r)$ varies slowly with radius and the phase

$$\Theta_m = \int^r k(r') dr' + m(\phi - \Omega_p t), \quad (3.80)$$

varies rapidly with radius. Again only the real component is physically relevant, and we have written $\omega = m\Omega_p$ as we are assuming the waves are generated by an embedded planet. To investigate the shape of the spiral wake we will look for lines of constant phase that are defined by the condition $\frac{d\Theta_m}{dr} = 0$ and so

$$\frac{d\phi}{dr} = -\frac{k}{m}. \quad (3.81)$$

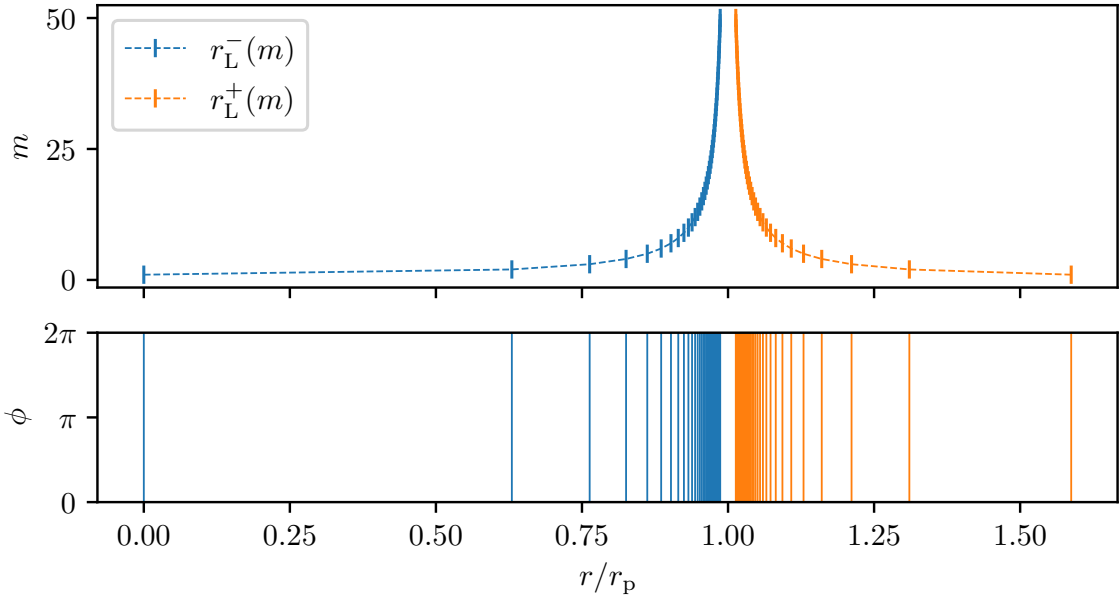


Figure 3.4: Lindblad resonance positions as given by Equation (3.78). The bottom panel shows the physical radial locations in the disk where these resonances occur for different m , with the inner resonances coloured blue and the outer resonances coloured orange. The top panel shows how these position are related to m , and demonstrates the asymptotic behaviour of the resonance position $r_L^\pm \rightarrow r_p$ as $m \rightarrow \infty$.

This is the same as the relation used to find the pitch angle of the spiral shape in Equation (3.4). Assuming Keplerian rotation such that $\kappa = \Omega = \Omega_K$, we can find k from the Lin-Shu Dispersion relation (3.45)

$$k^2 = \frac{m^2 (\Omega - \Omega_p)^2 - \kappa^2}{c^2}, \quad (3.82)$$

$$= \frac{m^2 \Omega_K^2}{c^2} \frac{1}{r_p^3} \left[r^{3/2} - (r_L^+)^{3/2} \right] \left[r^{3/2} - (r_L^-)^{3/2} \right]. \quad (3.83)$$

The tidal forcing of the planet results in density waves launched at the Lindblad resonances, with those launched at r_L^- and r_L^+ propagating inwards and outwards through the disk respectively (Goldreich and Tremaine, 1979, 1980). Figure 3.5 shows the shape of the $m = 3$ spiral waves generated at the $r_L^\pm(m = 3)$ Lindblad resonances as they propagate away from the planet. The shape of these spirals is calculated as follows. Placing ourselves in the frame where the planet is stationary at $\phi = 0$, we can find the phase of the spiral waves simply by integrating Equation (3.81) giving (Bae and Zhu, 2018)

$$\phi_m(r) = \phi_m(r_L^\pm) - \int_{r_L^\pm}^r \frac{k(r')}{m} dr', \quad (3.84)$$

which consists of a constant offset $\phi_m(r_L^\pm)$ term that gives the azimuthal launching location, plus a term that varies with radius. For the waves launched at the Lindblad resonances, the constant offset term can be found from the asymptotic behaviour of the Airy function (Ward, 1986). For the n th arm of the m th mode, where $n = 0, 1, \dots, m - 1$ the offset is given by

$$\phi_{m,n}(r_L^\pm) = -\text{sgn}(r_L^\pm - r_p) \frac{\pi}{4m} + 2\pi \frac{n}{m}. \quad (3.85)$$

Now considering the $n = 0$ arm, we see from the above that it launches closest to $\phi = 0$ and thus closest to the planet. For large m , we find that the constant offset term $\phi_{m,0}(r)$ becomes independent of m . In addition, we have that $r_L^\pm \rightarrow r_p$ as $m \rightarrow \infty$. This results in the formation of a coherent,

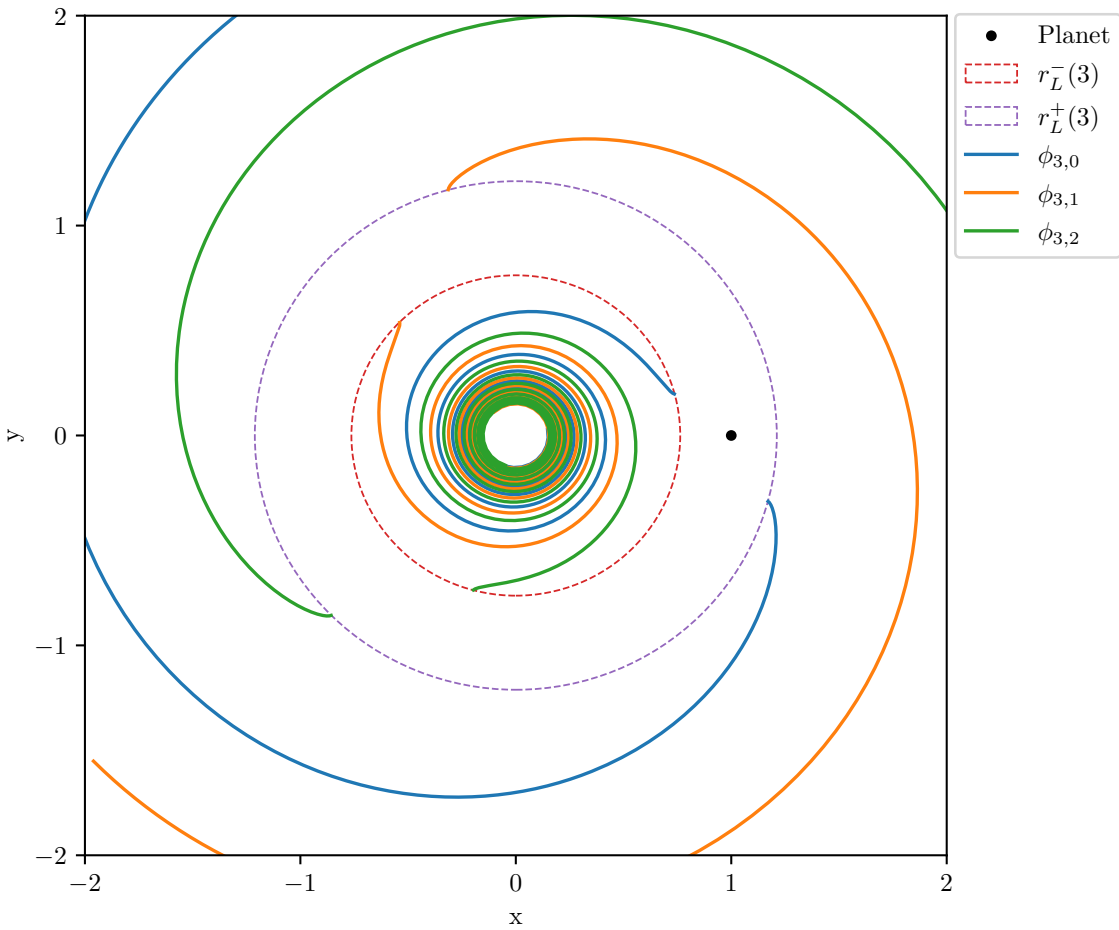


Figure 3.5: Schematic overview of the $m = 3$ mode excited in a Keplerian disk. The disk has sound speed $c \propto r^{-1/4}$ where the aspect ratio at the planet is $(H/r)_p = 0.1$. The planet is placed at $(1, 0)$ and the inner and outer Lindblad resonances are shown by the red and purple dashed lines respectively. The blue, orange and green solid lines show lines of constant phase for the $n = 0, 1, 2$ spiral arms excited at the resonances as they propagate inwards and outwards in the disk. These lines were calculated using Equations (3.84) – (3.86).

one-armed spiral wave centred on the planet, as (3.84) and (3.85) reduces to

$$\phi_{\infty,0}(r) = - \int_{r_p}^r \frac{\Omega(r') - \Omega_p}{c(r')} dr'. \quad (3.86)$$

Because the $n = 0$ waves launch almost in phase nearby the planet, as seen in Figure 3.6, the planet wake is always centred on the planet location. The above result was first found by Ogilvie and Lubow (2002), although they wrote it in a different form. They dubbed the resultant spiral wave the planet “wake” in analogy with the Kelvin wedge produced by a ship moving through water. The form shown above was first given in Rafikov (2002a).

Ogilvie and Lubow also investigated the degree to which the constructive interference along $\phi_{\infty,0}$ fails. To do this they calculated the relative error Δ_m in the phase for each m caused by the approximation we have performed above. Note that this is not the same quantity as we defined in (3.27). Figure 3.7 shows Δ_m in both the outer and inner disk, for multiple values of m . We see that in general, the approximation improves for larger m . Additionally, the behaviour in the inner and outer disk is very different. Ogilvie and Lubow found that $\Delta_m \sim \text{constant}$ as $r \rightarrow \infty$, while Δ_m diverges as $r \rightarrow 0$, and that for any fixed r , $\Delta_m \rightarrow 0$ as $m \rightarrow \infty$. Thus the accuracy of the one-armed wake shape (3.86) is in general better in the outer disk than the inner disk, and also depends on the importance of each mode. If the wave is dominated by large m then (3.86) holds everywhere except for very small disk radii, while always failing if dominated by $m = 1$ or 2 (Ogilvie and Lubow, 2002). The dominating

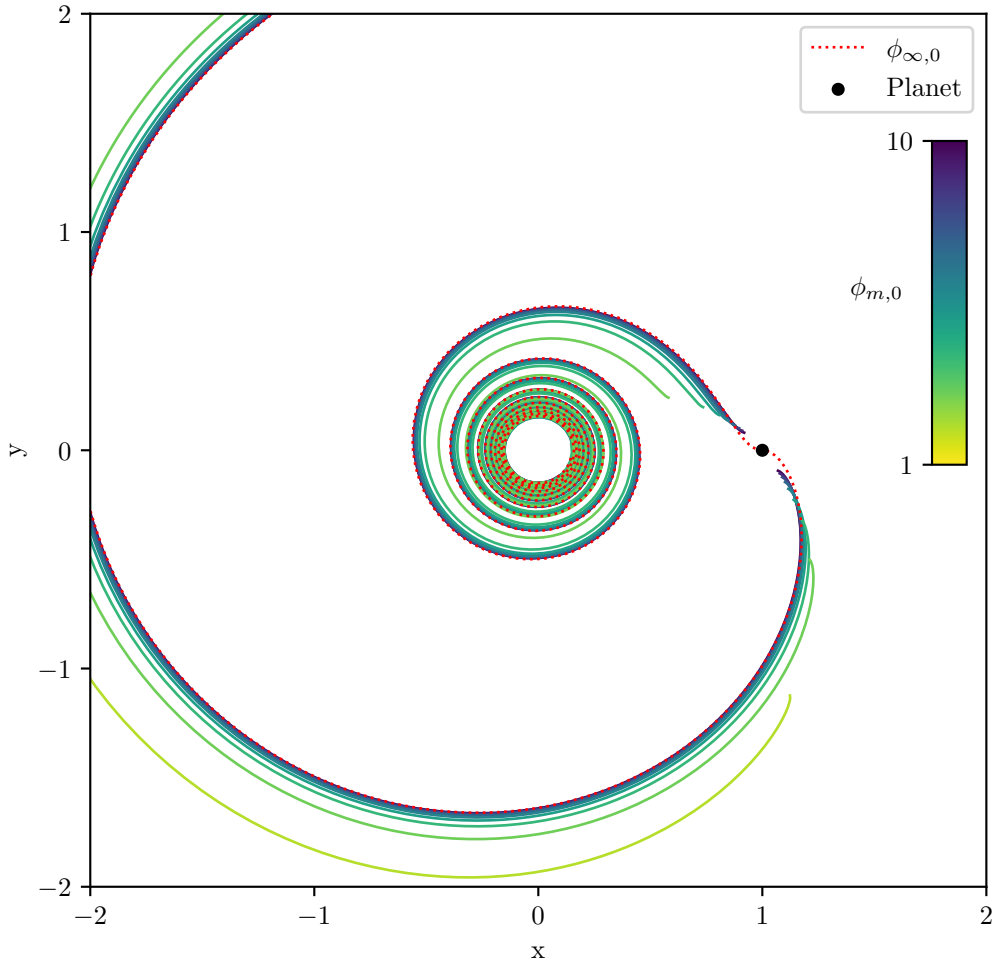


Figure 3.6: Plot of the $n = 0$ spiral arms defined by the lines of constant phase $\phi_{m,0}$ for modes $m = 1, \dots, 10$ (solid lines). $\phi_{\infty,0}$ is shown with the red dotted line. The planet is placed at $(1, 0)$ once again and the disk parameters are as in Figure 3.5. We see that asymptotically $\phi_{m,0}$ approaches the planet wake shape $\phi_{\infty,0}$ as the line of constant phase loses its m dependence for large m .

azimuthal mode for tidal forcing by a planet is $m_D \approx 1/2(H/r)_p^{-1}$ (Goldreich and Tremaine, 1980), and so for observed protoplanetary disks $m_D \gtrsim 5$ (Law et al., 2021b). The coherent planet wake picture should therefore hold well except for at small disk radii.

3.3.3 Additional spiral arms

In addition to constructive interference of the $n = 0$ components causing the planet wake, it is possible for additional spiral arms to form. These *secondary* and *tertiary* spiral arms (where the planet wake described in the previous section is the *primary* arm) were first seen in numerical calculations (Fung and Dong, 2015) and were not very well understood in the context of linear density wave theory until quite recently (Bae and Zhu, 2018; Miranda and Rafikov, 2019). Unlike the primary, these spirals are not centred on the planet position, and are instead generated some distance away in the inner disk.

Figure 3.8 shows the phase of the $n = 1$ and $n = 2$ components in the inner disk. We see that unlike for the $n = 0$ case, the waves are not launched in the vicinity of the planet, or nearby each other. However the overall behaviour of the constant offset launching term (3.85) is the same for non-zero n , namely that it becomes smaller as m increases and so the launching phases become closer for larger m . Furthermore, the modes become more tightly wound as m increases, with the second term of (3.84) also losing its m dependence for very large values. These effects allow the larger m modes launched closer to the planet to catch up to the low m modes. Bae and Zhu (2018) first performed this analysis and proposed that this catching up effect is responsible for the generation of secondary and tertiary

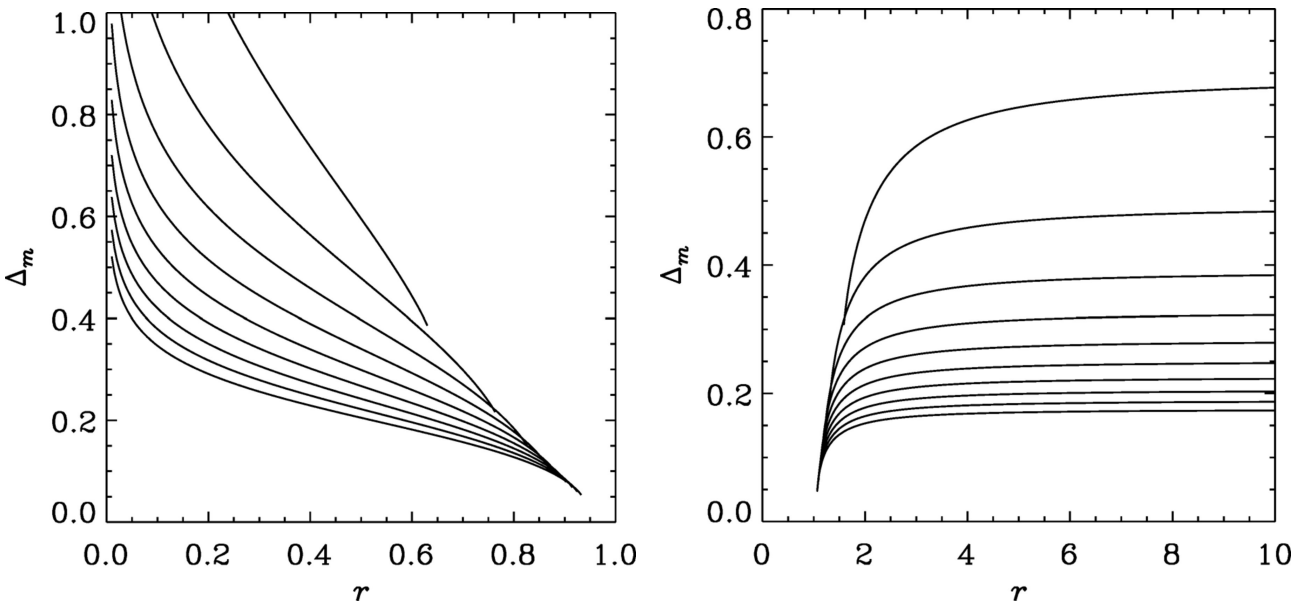


Figure 3.7: The error in the phase Δ_m resulting from neglecting the m dependence in Equation (3.84), plotted for both the inner (left) and outer (right) disk (Ogilvie and Lubow, 2002). The planet is placed at $r = 1$. Modes $m = 1, \dots, 10$ are shown from top to bottom. We see that the approximation improves for large m as expected.

spirals. This also provides a natural explanation as to why the additional arms are not centred on the planet, as the interference only becomes coherent after the large m modes have caught up in phase. Bae and Zhu also found that this effect does not operate in the outer disk, as the difference in phase between small and large m modes becomes constant instead of decreasing.

Miranda and Rafikov (2019) built upon this work through numerical calculations and showed that the formation of additional arms in the inner disk is a robust prediction of the linear theory. They did this by taking into account the global mode structure outside of the WKB approximation as used in Bae and Zhu (2018), and calculated both the phase and amplitude of each mode. They found that their results in general supported the picture of additional arms resultant from coincident phases, but that taking into account the amplitude information changes the level of correspondence and can be important, especially for the tertiary and higher order arms (those formed by $n > 2$).

In this work we will be concerned primarily with the waves generated by the planet in the outer disk and so our models will not include any of the additional arms in the inner disk, only the primary planet wake.

3.4 Linear Planet Wake Excitation

We now move on to calculating the density and velocity perturbations in the vicinity of the planet due to the planet wake. This follows the method presented in Goodman and Rafikov (2001); Rafikov (2002a), which itself is based on the seminal work by Goldreich and Tremaine (1978, 1980). This involves calculating the linear disk response for each of the Fourier modes of the perturbations. The solutions are *global* since the WKB approximation is not used. Historically the interest was first in calculating the Lindblad torque and not the profile of the wake itself, and so the phases of the Fourier harmonics were neglected (Goldreich and Tremaine, 1978, 1980; Artymowicz, 1993; Ward, 1997). Goodman and Rafikov (2001) included these phases to solve directly for the shape of the wake. Their approach for calculating the wake structure splits the problem into two separate regimes:

1. Linear wake *generation*: Provided that M_p is not too large ($\lesssim M_1$ defined in Equation (3.91)), the disturbance of the planet nearby the planet is weak enough that the wake can be calculated from linear theory.

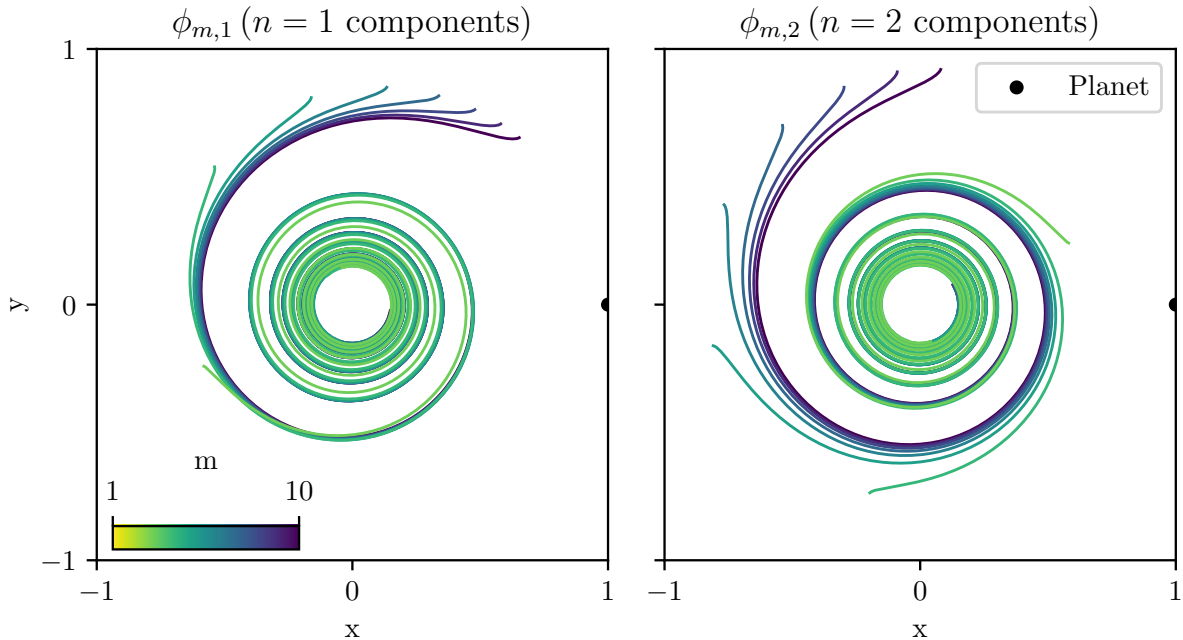


Figure 3.8: Plot of the $n = 1$ (left) and $n = 2$ spiral arms defined by $\phi_{m,n}$ for modes $m = 1, \dots, 10$ (solid lines). We show only the inner disk, with the planet placed at $(1, 0)$ and disk parameters as in Figure 3.5. We see that in both the $n = 1$ and $n = 2$ case, although the spirals start initially out of phase due to different launching positions, the larger m modes are able to catch-up resulting in the formation of the coherent secondary and tertiary spiral arms respectively.

2. Non-linear wake *propagation*: As the wave travels away from the planet it steepens into a shock and non-linear behaviour becomes important.

This approach is agnostic to the rotation, density and sound speed profiles of the disk, assuming only that they are functions of radius. It is also assumed that the disk is locally polytropic (see Section 4.3.5), inviscid, and non-self-gravitating.

It should be noted that the used of the language ‘‘generation’’ and ‘‘propagation’’ are slightly misleading. The solution that we will calculate is mathematically a steady-state and has no time dependence. In a physical sense the language is correct; waves are excited nearby the planet before propagating out into the disk. In a mathematical sense the language is potentially confusing since the solution is independent of time. These two opposing points of view are reconciled by considering that we are working in the frame where the planet is stationary. In reality the spiral pattern is *not* stationary. The remainder of this section is dedicated to outlining the linear wake generation, while the following section describes the non-linear propagation.

Above we stated that nearby the planet the disturbance is weak enough that linear theory is sufficient to describe wake generation provided the planet is not too large. This certainly seems counter-intuitive at first glance, should the disturbance not be largest in the direct vicinity of the planet? This is explained by the fact that a stationary perturber cannot excite density waves in a subsonic flow (Landau and Lifshitz, 1987). Thus no waves are generated within some characteristic distance from the planet, an effect known as the *torque cut-off* (Goldreich and Tremaine, 1980). In a Keplerian disk this distance is $2H_p/3$ (see Equation 3.90). The Lindblad resonances within this region, where m is large, are suppressed and therefore contribute minimally to the torque. In addition the resonances with very low m are not effectively excited due to their distance from the planet. Indeed the dominant mode is of order $(H_p/r_p)^{-1}$, as mentioned in Section 3.3.2. The resonances excited most efficiently are therefore located a few H_p from the planet, far enough to justify the linear approach.

The rest of this subsection directly follows Goodman and Rafikov (2001). The linear calculation is performed in the *shearing-sheet approximation* (Hill, 1878; Goldreich and Lynden-Bell, 1965). This

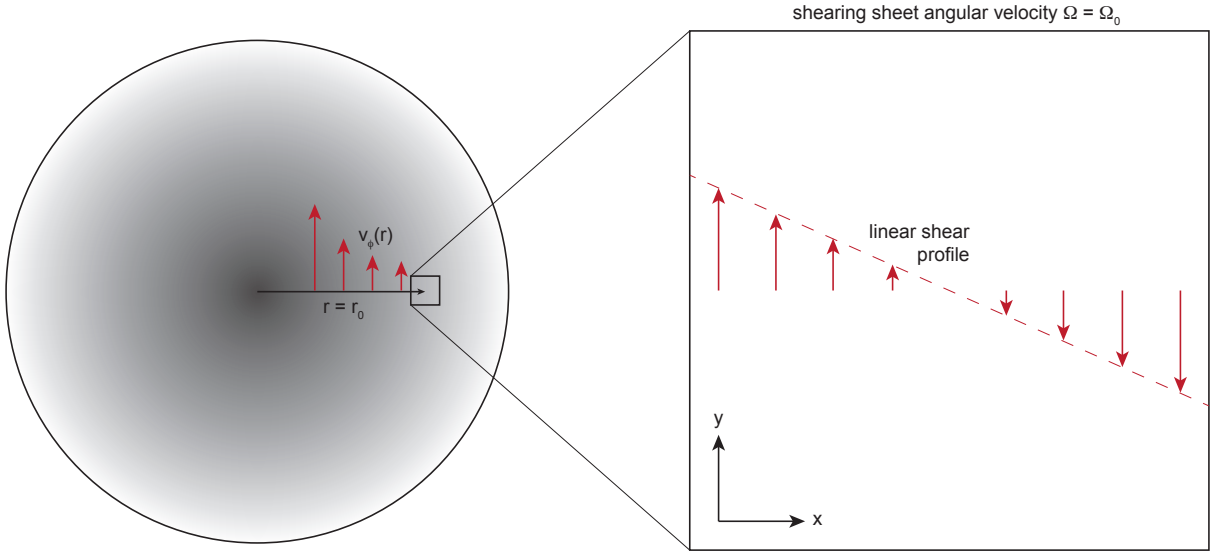


Figure 3.9: Schematic diagram of the shearing-sheet approximation from the lectures notes by Armitage (2022), where in our case $r_0 = r_p$ and $\Omega_0 = \Omega_p$ and so the shearing box is centred on the planet location. Under the approximation the shear nearby the planet is taken to be linear, while the surface density and sound speed are taken to be constant.

involves defining pseudo-cartesian coordinates centred on the planet location

$$x = r - r_p, \quad (3.87)$$

$$y = r_p (\phi - \phi_p), \quad (3.88)$$

where ϕ_p is the azimuthal location of the planet. The differential rotation of the disk is then expanded to lowest order in x/r_p , which reduces the azimuthal component of the flow to

$$v_0 = 2Ax; \quad 2A \equiv r \left. \frac{d\Omega}{dr} \right|_{r_p}, \quad (3.89)$$

where the shear A and rotation Ω rates are treated as constant (that does *not* make the above derivative zero), as is the vorticity $B \equiv A + \Omega$. The unperturbed surface density Σ_p and sound speed c_p are also assumed to be constant. A diagrammatic overview of the shearing-sheet approximation is presented in Figure 3.9.

We adopt as a length unit the Mach-1 length l_p , which is the distance from the planet where the flow becomes supersonic. This requires that $v_0 = 2|Ax| > c_p$ and so

$$l_p \equiv c_p / |2A|. \quad (3.90)$$

For the planet mass we adopt the unit

$$M_1 \equiv \frac{c_0^3}{|2A|G}. \quad (3.91)$$

For a Keplerian disk M_1 is equal to the *thermal mass* defined in Equation (3.130). For $M_p \gtrsim M_1$ the Roche lobe of the planet will become larger than l_p , causing the linear approximation to fail. This is also the gap opening condition for an inviscid disk as discussed in Section 3.6. In the linear regime the amplitude of the wake is directly proportional to the planet mass, and so it is sufficient to carry out the calculation only once and scale it appropriately as needed.

In the frame of the planet the wake is stationary such that the radial velocity, azimuthal velocity and density perturbations, u, v and $\sigma = \delta\Sigma/\Sigma$ respectively, are independent of time. The spatial

Fourier transform of these components $\hat{u}, \hat{v}, \hat{\sigma}$ are functions of the coordinate wavenumbers k_x and k_y , and they satisfy (Goldreich and Tremaine, 1978, 1980)

$$\frac{d^2\hat{v}}{d\tau^2} + [c^2k^2 + \kappa^2] \hat{v} = -ik_y \frac{d\hat{\Phi}_p}{d\tau} + 2ik_x B \hat{\Phi}_p \quad (3.92)$$

$$\hat{u} = -\frac{1}{c^2 k_y^2 + 4B^2} \left(2B \frac{d\hat{v}}{d\tau} - c^2 k_x k_y \hat{v} + 2iB k_y \hat{\Phi}_p \right) \quad (3.93)$$

$$\hat{\sigma} = \frac{i}{c^2 k_y^2 + 4B^2} \left(k_y \frac{d\hat{v}}{d\tau} + 2B k_x \hat{v} + ik_y^2 \hat{\Phi}_p \right), \quad (3.94)$$

where

$$\tau \equiv -\frac{k_x}{2Ak_y}, \quad (3.95)$$

is a pseudo-time variable, $k = \sqrt{k_x^2 + k_y^2}$ is the instantaneous wavenumber, and $\hat{\Phi}_p = -2\pi GM_p/k$ is the Fourier transform of the planet potential. This system of ordinary differential equations, combined with the initial condition that $\hat{v} = 0$ as $\tau \rightarrow -\infty$, constitute a determined system where the unique solution provides the density and velocity perturbations along the wake after Fourier transforming back to coordinate space.

3.5 Non-Linear Planet Wake Evolution

Goodman and Rafikov (2001) first studied the non-linear evolution of the planet wake, neglecting both the disk geometry and variations in density and sound speed, while Rafikov (2002a) updated the analysis to include these effects. We are obviously interested in accounting for these aspects and so we will largely follow Rafikov (2002a) in this section, but we will endeavour to make it clear when a result is originally from Goodman and Rafikov (2001).

After the wake is generated, it propagates away from the planet. At distances $\gg l_p$ the contribution of the planet potential becomes negligible. However unlike in the shearing sheet, we must now consider the evolution of Σ and c with radius, as well as the global geometry of the disk. Rewriting the 2D inviscid fluid Equations (3.5)-(3.7) in a rotating frame such that the planet is stationary at $\phi = \phi_p$, and ϕ is defined such that $\Omega > 0$, we obtain (Landau and Lifshitz, 1987)

$$v_r \partial_r v_r + \frac{v_\phi}{r} \partial_\phi v_r - \frac{v_\phi^2}{r} = -\partial_r \Phi - \frac{1}{\Sigma} \partial_r P + 2\Omega_p v_\phi + \Omega_p^2 r, \quad (3.96)$$

$$v_r \partial_r v_\phi + \frac{v}{r} \partial_\phi v_\phi - \frac{v_r v_\phi}{r} = -\frac{1}{r} \partial_\phi \Phi - \frac{1}{r\Sigma} \partial_\phi P - 2\Omega_p v_r, \quad (3.97)$$

$$\frac{1}{r} \partial_r (r\Sigma v_r) + \frac{1}{r} \partial_\phi (\Sigma v_\phi) = 0, \quad (3.98)$$

where we have also dropped all time dependence, and $\Phi = \Phi_\star$ since we are neglecting the planet potential.

We now perform a perturbative study including weak non-linear behaviour. We rewrite the velocities as

$$v_r = u; \quad v_\phi = v_0(r) + v, \quad (3.99)$$

where

$$v_0(r) = r\Delta\Omega \equiv r(\Omega - \Omega_p). \quad (3.100)$$

u and v are thus the radial and azimuthal velocity perturbations. We assume that the shock formed is weak (we will refer to this as the *weak shock approximation*) such that $|u|, |v| \ll |v_0|$. $\Delta\Omega \neq 0$ since we are working in region away from the planet. In addition, the WKB approximation is applied such that

$v \ll u$ and $\partial_\phi \ll r\partial_r$ as shown in the appendix of Rafikov (2002a). With the above considerations, Equations (3.96) - (3.98) are transformed to

$$\Delta\Omega\partial_\phi u + u\partial_r u - 2\Omega v = -\frac{1}{\Sigma}(\partial_r P - \partial_r P_0) + \frac{v^2}{r}, \quad (3.101)$$

$$\Delta\Omega\partial_\phi v + u\partial_r v + 2Bu = -\frac{1}{r}\left(\frac{1}{\Sigma}\partial_\phi P + uv\right), \quad (3.102)$$

$$\Delta\Omega\partial_\phi\Sigma + u\partial_r\Sigma + \Sigma\partial_r u = -\frac{1}{r}(\Sigma u + v\partial_\phi\Sigma + \Sigma\partial_\phi v). \quad (3.103)$$

We have kept terms up to second order in u and v . The radial coordinate ξ is now introduced, consisting of an integral transformation that essentially encodes the differential rotation of the disk and simplifies the spatial propagation of the wake (note the similarity to Equation (3.86)). It is defined by

$$\xi = \int_{r_p}^r [\Omega(r') - \Omega_p] dr', \quad (3.104)$$

and results in the transformation of the Equations (3.101) - (3.103) to

$$\partial_\phi u + u\partial_\xi u + \frac{1}{\Sigma}\partial_\xi P - \frac{1}{\Sigma_0}\partial_\xi P_0 = \frac{1}{\Delta\Omega r}(2\Omega rv + v^2), \quad (3.105)$$

$$\partial_\phi v + u\partial_\xi v + \frac{c^2}{\Delta\Omega r\Sigma}\partial_\phi\Sigma = -\frac{1}{\Delta\Omega r}(2Bru + uv), \quad (3.106)$$

$$\partial_\phi\Sigma + u\partial_\xi\Sigma + \Sigma\partial_\xi u = -\frac{1}{\Delta\Omega r}(\Sigma u + v\partial_\phi\Sigma + \Sigma\partial_\phi v). \quad (3.107)$$

The left-hand side of the equations above are similar to the usual system of equations that describe the motion of a one-dimensional isentropic gas (Landau and Lifshitz, 1987), except that we have an azimuthal coordinate ϕ in place of the time coordinate t and the ξ coordinate in place of the spatial coordinate x . We exploit this similarity to simplify the above equations using the *method of characteristics*. The 1D isentropic gas flow system possesses two *Riemann invariants* that are each conserved along a curve in the xt plane. These curves are called the *characteristics*. This is reviewed briefly in appendix A. In our case the non-zero right-hand sides of the equations causes the Riemann invariants R_\pm to no longer be conserved exactly along each of the characteristics C_\pm . Instead, R_\pm evolve in a predictable manner. Following similar analysis to that in appendix A, we find that Equations (3.105) and (3.107) reduce to

$$[\partial_\phi + (u \pm c)\partial_\xi] R_\pm = -\left(\frac{1}{\Sigma}\partial_\xi P - \frac{1}{\Sigma_0}\partial_\xi P_0 - c\partial_\xi\frac{2c}{\gamma-1} \pm cu\frac{\partial_\xi\Sigma}{\Sigma} \mp u\partial_\xi\frac{2c}{\gamma-1}\right) + \frac{1}{\Delta\Omega r}(2\Omega rv + v^2 \mp cu \mp cv\partial_\phi\ln\Sigma \mp c\partial_\phi v), \quad (3.108)$$

where the Riemann invariants are

$$R_\pm = u \pm \frac{2c}{\gamma-1}, \quad (3.109)$$

and the characteristics are

$$C_\pm : \frac{d\xi}{d\phi} = u \pm c. \quad (3.110)$$

The C_- characteristic follows the planet wake, while the C_+ characteristic crosses it (Goodman and Rafikov, 2001). Therefore C_- is always in the perturbed region while C_+ is predominantly in the unperturbed region. By assuming that the wake-crossings affect the value of R_+ minimally and approximating its value as constant, we find that

$$R_+ = \frac{2c_0}{\gamma-1}, \quad (3.111)$$

everywhere. Since we are assuming R_+ is exactly conserved, this implies

$$u = \frac{2(c_0 - c)}{\gamma - 1}, \quad (3.112)$$

and so

$$R_- = \frac{2(c_0 - 2c)}{\gamma - 1}. \quad (3.113)$$

Based on these results it is possible to show that the system further reduces to a simple partial differential equation, the inviscid Burger's Equation (see appendix A of [Rafikov, 2002a](#))

$$\partial_t \chi - \chi \partial_\eta \chi = 0, \quad (3.114)$$

where χ is a remapping of the surface density perturbation defined as

$$\chi \equiv \frac{\gamma + 1}{2} \frac{\Sigma - \Sigma_0}{\Sigma_0} g(r), \quad (3.115)$$

$$\text{where } g(r) \equiv \frac{2^{1/4}}{r_p c_p \Sigma_p^{1/2}} \sqrt{\frac{r \Sigma_0 c_0^3}{|\Omega - \Omega_p|}}, \quad (3.116)$$

and the coordinates t and η are defined as

$$t(r) \equiv -\frac{r_p}{l_p} \int_{r_p}^r \frac{\Omega(r') - \Omega_p}{c_0(r') g(r')} dr', \quad (3.117)$$

$$\eta(r, \phi) \equiv \frac{r_p}{l_p} \left(\phi - \phi_p + \int_{r_p}^r \frac{\Omega(r') - \Omega_p}{c_0(r')} dr' \right) \quad (3.118)$$

where l_p is the Mach-1 length (3.90) and ϕ_p is the azimuthal coordinate of the planet. The η coordinate can be written in a clearer form by comparing the third term with Equation (3.86):

$$\eta(r, \phi) \equiv \frac{r_p}{l_p} (\phi - \phi_{\text{wake}}), \quad (3.119)$$

$$\text{where } \phi_{\text{wake}} \equiv \phi_p - \int_{r_p}^r \frac{\Omega(r') - \Omega_p}{c_0(r')} dr'. \quad (3.120)$$

Intuitively, t can be thought of a coordinate that travels *along* the wake, while η is a rescaled angular coordinate that *crosses* the wake.

3.5.1 Wave dissipation

Burger's equation generically produces shocks from smooth waveforms due to the crossing of characteristics ([Whitham, 1999](#)). Figure 3.10 shows the evolution of the wave profile taken at different t values. We see that at the edge of the linear regime the waveform is initially smooth. As the wake evolves away from the planet its amplitude decays but areas above and below $\chi = 0$ steepen and form two shocks, one moving in the $+\eta$ direction and one moving in the $-\eta$ direction. The resultant waveform is called an *N-wave* ([Landau and Lifshitz, 1987](#)). [Goodman and Rafikov \(2001\)](#) found numerically that the shock forms at

$$t_{\text{shock}} = t_0 + 0.79 \left(\frac{M_p}{M_1} \right)^{-1}, \quad (3.121)$$

and so more massive planets produce a shock closer to the planet.

After the shock is formed the wave becomes dissipative; its amplitude begins to decay as angular momentum is deposited into the disk. Prior to shock formation the *angular momentum flux* (AMF),

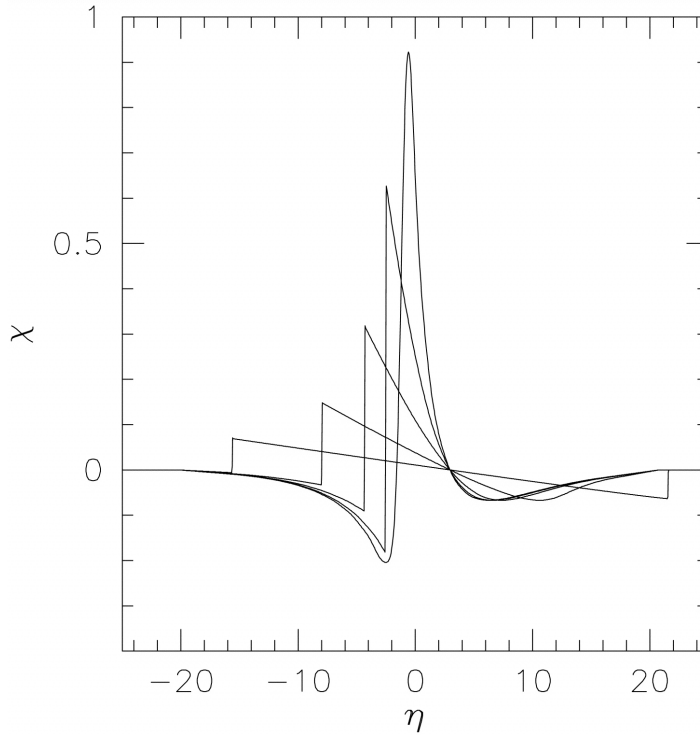


Figure 3.10: Evolution of the wake profile under the Burger’s Equation (3.114) from [Goodman and Rafikov \(2001\)](#). They solved the equation using a second order advection scheme with initial conditions taken from the linear regime at a distance of $2l_p$ from the planet, corresponding to $t = t_0$. χ profiles are shown as slices in t and as a function of η . These profiles were taken at $t - t_0 = 0, 4, 16, 64, 256$ in order of greatest to lowest amplitude.

the amount of angular momentum transported along the wake, is perfectly conserved. The AMF f_J can be calculated as ([Rafikov, 2002a](#))

$$f_J(r) = \frac{c_0^3(r)r}{\Delta\Omega(r)\Sigma_0(r)} \int_0^{2\pi} (\Sigma - \Sigma_0)^2 d\phi, \quad (3.122)$$

which we can rewrite as a function of t using the transformations (3.115)–(3.118) giving

$$f_J(t) = \frac{2^{3/2} c_p^3 r_p \Sigma_p}{(\gamma + 1)^2 |2A(r_p)|} \Phi(t), \quad (3.123)$$

$$\text{where } \Phi(t) = \oint \chi^2(t, \eta) d\eta \quad (3.124)$$

is the dimensionless AMF, which we will always write as a function of t to avoid confusion with the potential. After shock formation the resultant dissipation results in the non-conservation of the AMF, as shown in Figure 3.11.

Recently [Cimerman and Rafikov \(2021\)](#) performed a numerical study to validate the weakly non-linear wake evolution theory. They compared the Burger’s equation evolution with hydrodynamical simulations performed with the grid code ATHENA++ ([Stone et al., 2020](#)). They found that the transformation to t, η, χ space performs well for a range of planet masses, but also that Burger’s equation actually overestimates the wave damping. This effect however was less severe for larger planet masses. They also found that it is relatively straightforward to calibrate the theory to account for this discrepancy. See in particular Sections 5.1, 5.2 and 8.1 of [Cimerman and Rafikov \(2021\)](#) for greater detail.

3.5.2 Asymptotic planet mass scaling

While the AMF is no longer conserved in the dissipative wake evolution regime, Burger’s equation does encode the perfect conservation of a quantity both before and after shock formation, which is the

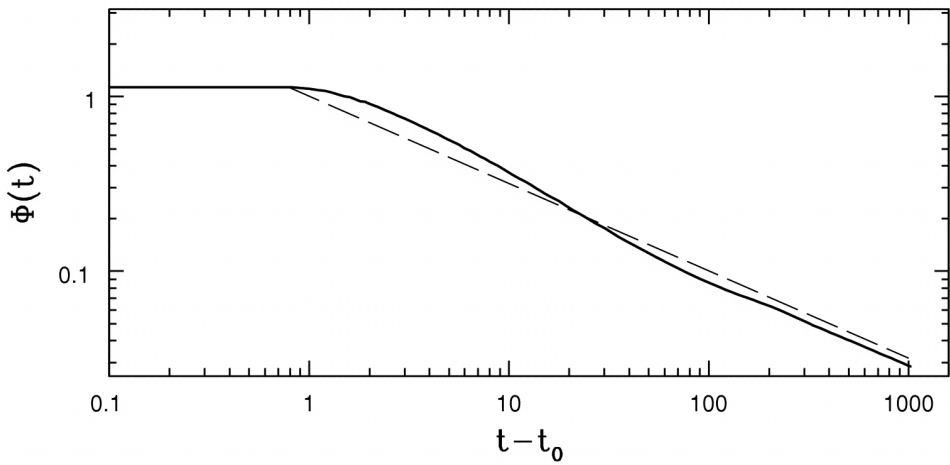


Figure 3.11: Behaviour of the dimensionless AMF $\Phi(t)$ in the non-linear regime as a function of t using $M_p = M_1$ (solid line; [Rafikov, 2002a](#)). Before the shock is formed at approximately $t - t_0 \approx 1$ we see that $\Phi(t)$ is conserved, while decaying steadily after the shock is formed. The dashed line demonstrates that the AMF asymptotically scales as $\Phi(t) \propto t^{-1/2}$.

area under the curve χ ([Landau and Lifshitz, 1987](#); [Whitham, 1999](#)). We will show that physically this corresponds to conservation of mass in the disk. The area \mathcal{A} under the curve at a “time” t is given by

$$\mathcal{A} = \oint \chi d\eta = \frac{(\gamma + 1)g(r)r_p}{2\Sigma_0 l_p} \int_0^{2\pi} (\Sigma - \Sigma_0) d\phi, \quad (3.125)$$

where in the second equality we have used transformations (3.115) and (3.118). The second integral in the above must evaluate to zero by physical argument, since the perturbed density profile must have the same mass as the unperturbed profile $\int_0^{2\pi} \Sigma d\phi = \int_0^{2\pi} \Sigma_0 d\phi$. Therefore the conservative properties of Burger’s equation, that $\frac{d\mathcal{A}}{dt} = 0$, ensures that the mass of each annulus in the disk is unchanged by the density perturbation.

Using this area conservation property [Bollati et al. \(2021\)](#) derived an asymptotic solution for the N-wave profile of the planet wake in the limit of $t \rightarrow \infty$:

$$\chi(t, \eta) \sim \begin{cases} \frac{\operatorname{sgn}(r - r_p)\eta + \tilde{\eta}}{t - t_0} & \text{if } \eta \in [\eta_-, \eta_+], \\ 0 & \text{else,} \end{cases} \quad (3.126)$$

where $\tilde{\eta} \approx 2.96$ is the value of η where the N-wave intersects the η -axis. Additionally

$$\eta_{\pm} = -\operatorname{sgn}(r - r_p)\tilde{\eta} \pm \sqrt{2\mathcal{A}(t - t_0)}, \quad (3.127)$$

$$\text{where } \mathcal{A} = |C_0| \frac{\gamma + 1}{2^{3/4}} \frac{M_p}{M_1}, \quad (3.128)$$

and $C_0 \approx -0.4$ is a numerically determined constant ([Bollati, 2020](#)).

From this asymptotic solution one may determine a scaling relation for the planet mass in terms of only the distance the wake has propagated from the planet $t - t_0$ and the width of the wake $\eta_+ - \eta_-$, given by

$$\frac{M_p}{M_1} \propto \frac{(\eta_+ - \eta_-)^2}{t - t_0}. \quad (3.129)$$

This scaling relation tells us the fundamental information that must be determined in order to constrain a planet mass from its wake observationally. We see that we must know the reference mass M_1 , as well as the transformations $t(r)$ and $\eta(r, \phi)$. From this we may use Equations (3.91), (3.117) and (3.118) to produce a full list of basic quantities of the disk and planet system that must be determined:

1. The rotation profile of the disk $\Omega(r)$ (although Keplerian is likely a good approximation),
2. The unperturbed sound speed profile $c_0(r)$ OR the pressure scale height $H(r)$,
3. The unperturbed surface density profile $\Sigma_0(r)$,
4. The planet orbital radius r_p ,
5. The planet azimuth ϕ_p .

However, we note that from Equation (3.120) that $c_0(r)$, r_p and ϕ_p are all determined by the shape of the wake. Therefore if we assume a disk to be Keplerian and fit the wake shape, all that remains is to determine Σ_0 and then M_p will be determined. The most straightforward way to constrain this is through determining the size of the perturbation in χ which depends on $g(r)$ and so on Σ_0 . While at this stage it is not clear on how to extract the information from observations, this at least shows that the planet mass is determined entirely by the wake shape and amplitude.

Finally, while it is possible to calculate the scale factor for the proportionality relation (3.129) from theory, the work of [Cimerman and Rafikov \(2021\)](#) suggests that this is better done through comparison with hydrodynamical simulations.

3.6 Gap Opening

For sufficiently large planets, the non-linear effects are such that the planet wake shocks immediately after formation and the solution can no longer be neatly separated into the linear generation and non-linear propagation regimes. As already hinted at, the condition under which this occurs in an inviscid disk is that the planet mass M_p exceeds the characteristic mass M_1 defined in Equation (3.91). For a Keplerian disk the minimum gap-opening mass is the thermal mass ([Lin and Papaloizou, 1993](#)), defined as ([Goodman and Rafikov, 2001](#))

$$M_{\text{th}} \equiv \frac{2}{3} \left(\frac{H_p}{r_p} \right)^3 M_* . \quad (3.130)$$

Thus the wake solution approach presented in Sections 3.4 and 3.5 is only *strictly* valid for sub-thermal mass planets. It is not clear however, that the non-linear Burger's equation evolution is invalid for planets greater than the thermal mass. The non-linear evolution prescription's strictest requirement is that the shock is sufficiently weak, such that the perturbative approach is still valid.

Gap opening occurs because the dissipative shock fronts allow angular momentum from the material nearby the disk to be deposited elsewhere ([Lin and Papaloizou, 1979](#); [Goldreich and Tremaine, 1979, 1980](#)). The rough physical criterion for a gap to open depends on two conditions. Firstly the Hill radius of the planet r_H ([Hill, 1878](#)) must fulfil $r_H \gtrsim H$, known as the *thermal condition*. Secondly the transfer rate of angular momentum between the wake and disk must exceed the local transport rate from effective viscosity ([Lin and Papaloizou, 1993](#)). The thermal condition is equivalent to $M_p = M_{\text{th}}$ while the second is irrelevant to discussions of inviscid disks.

[Kanagawa et al. \(2015a\)](#) found an analytic relation between planet mass M_p , central star mass M_* , viscosity α ([Shakura and Sunyaev, 1973](#)), and gap depth Σ_p/Σ_0 in the case of an axisymmetric and geometrically thin gas disk subject to viscous evolution

$$\frac{M_p}{M_*} = 5 \times 10^{-4} \left(\frac{\Sigma_0}{\Sigma_p} - 1 \right)^{\frac{1}{2}} \left(\frac{(H/r)_p}{0.1} \right)^{\frac{5}{2}} \left(\frac{\alpha}{10^{-3}} \right)^{\frac{1}{2}}, \quad (3.131)$$

where the gap depth Σ_p/Σ_0 is written in terms of the surface density in the gap Σ_p , and the unperturbed surface density Σ_0 .

The modern understanding of gap opening, considering both the effects of viscosity and non-linear planet wake evolution, states that the thermal condition is unnecessary. Instead planets $\lesssim M_{\text{th}}$ may

be capable of opening a gap depending on the disk conditions (Rafikov, 2002b). The opening criterion is given by (Kanagawa et al., 2015b)

$$M_p \gtrsim 5 \left(\frac{H_p}{r_p} \right)^{\frac{5}{2}} \alpha^{\frac{1}{2}} M_{\star}. \quad (3.132)$$

Hydrodynamical simulations have confirmed the ability of sub-thermal mass planets to open gaps (Duffell and MacFadyen, 2013).

Finally, gap-opening occurs not only in the gas component of disks, but also the dust component. Dust gaps are actually far more pervasive observationally (e.g. ALMA Partnership et al., 2015; Andrews et al., 2016; Isella et al., 2016; Andrews et al., 2018a; Huang et al., 2018a), since the gas structure of a disk is less straightforward to probe (see review by Miotello et al., 2022). Dust gaps can be created through the mechanisms already discussed, since the grains will migrate to the pressure maxima induced at the edges of the gas gap (Paardekooper and Mellema, 2004). The large and weakly-coupled grains become trapped at these maxima. Smaller grains couple to the gas strongly and so flow with it into the vicinity of the planet before being accreted (Paardekooper and Mellema, 2006; Fouchet et al., 2007). Additionally, gaps may be induced only in the dust component. Drag acts on dust grains interior and exterior to the planet's orbit resulting in inward radial migration. Exterior to the orbit the tidal torque induced by the planet resists the inward drift (Dipierro et al., 2016). Dust grains are therefore cleared from near the planet's orbit resulting in a dust gap.

4

Semi-Analytic Models of Planet Wakes

This chapter is concerned with the method that we have used to create semi-analytic⁹ models of planet wakes. These models encompass both the linear and non-linear disk response caused by a perturbing planet as described in the previous chapter. This work builds on that presented in [Bollati et al. \(2021\)](#) and so we will be predominantly concerned with the differences between our methods. However we aim to provide enough detail to be understandable without having read the aforementioned paper.

4.1 Wakeflow: A Python Package For Semi-Analytic Models of Planet Wakes

This section has been submitted to the Journal of Open Source Science and is currently in review. The preprint is publicly available here: <https://github.com/TomHilder/wakeflow/blob/master/paper/paper.md>

Summary

WAKEFLOW is a Python package for generating semi-analytic models of the perturbations induced by planets embedded in gaseous circumstellar disks. These perturbations take the form of a spiral shock wave ([Ogilvie and Lubow, 2002](#)), and are often called a “planet wake” in analogy with that produced by a boat in a lake.

Statement of need

Detecting newly formed planets embedded in their disk is a challenging problem in the field of planet formation. A major area of progress in recent years is the detection of planets by the gravitationally induced disturbance in their host disks. This disturbance, caused by the planet wake, manifests as a deviation in velocity from the bulk flow which may be measured through the Doppler shift of molecular lines (e.g. [Perez et al., 2015](#); [Pinte et al., 2018b](#)). Such kinematic observations have been accurately reproduced through 3D fluid simulations of the planet-disk interaction, allowing for the inference of planet and disk properties ([Pinte et al., 2018b, 2019](#)). However, these studies are computationally expensive.

WAKEFLOW eases this computational cost by applying the theory of planet wake generation and propagation ([Goldreich and Tremaine, 1979](#); [Goodman and Rafikov, 2001](#); [Rafikov, 2002a](#); [Bollati et al., 2021](#)) to create semi-analytic models of planet wakes. WAKEFLOW models are readily created in a few seconds on a modern laptop, as opposed to the hours of supercomputer time needed for

⁹We will use the terms analytic and semi-analytic interchangeably from now on.

3D hydrodynamical simulations. The relatively low computational cost of WAKEFLOW means that researchers can get an idea of whether planet-disk interactions can explain their observations, and the disk and planet parameters needed, before spending computer time on more detailed simulations.

WAKEFLOW can interface with the radiative transfer code MCFOST (Pinte et al., 2006, 2009) in order to create synthetic observations of the semi-analytic models for direct comparison with observed continuum or line emission.

WAKEFLOW is partially adapted from a previous Python code also written by us called ANALYTICAL_KINKS¹⁰. WAKEFLOW is intended to be a more complete, versatile and easy to use version of that code, and it obeys standard Python packaging conventions. In addition, WAKEFLOW can directly interface with MCFOST while ANALYTICAL_KINKS cannot. At the time of writing, no other open source software packages exist to generate the perturbations induced by an embedded planet in a circumstellar disk using the semi-analytic theory of planet wakes.

Existing scientific publications focusing on detecting the kinematic signatures of planets that have used WAKEFLOW or its predecessor ANALYTICAL_KINKS include Bollati et al. (2021), Calcino et al. (2022), Teague et al. (2022), Garg et al. (2022) and Fasano et al.(in prep.).

Acknowledgements

WAKEFLOW relies on the following scientific Python packages: NUMPY (Harris et al., 2020), MATPLOTLIB (Hunter, 2007), SciPy (Virtanen et al., 2020) and ASTROPY (Astropy Collaboration et al., 2022).

4.2 Semi-Analytic Solution Algorithm

Here we provide an overview of the algorithm used by WAKEFLOW to generate models. For stages that are sufficiently different to Bollati et al. (2021), further detail will be provided in Section 4.3. The algorithm proceeds as:

1. The global grid is generated based on the user’s choice of grid geometry and number of grid points. Both cylindrical and cartesian grid geometries are supported, as well as the MCFOST grid geometry.

The run time for WAKEFLOW scales linearly in the number of grid points $n_x \times n_y$ or $n_r \times n_\phi$, but is roughly independent of the number of points in the vertical direction n_z .

2. The unperturbed disk density and velocity structure is calculated based on the user’s choice of disk parameters as outlined in Section 4.3.1.
3. The linear perturbations are calculated and mapped onto the global disk geometry, following Section 4.3.2. The perturbations σ, u and v are assumed to be independent of vertical height z .
4. The initial conditions for the non-linear evolution are extracted from the edge of the linear regime along a slice of constant t , as described in 4.3.3.
5. Burger’s equation is solved in (t, η) space until $t_f = 300$ using a vectorised Godunov solver (LeVeque et al., 1998). Unlike in Bollati et al. (2021) we use make use of adaptive time-steps, which both ensures the stability of the solution (especially for large planet masses that shock quickly), as well as improves efficiency as large time-steps are taken when appropriate. After t_f , the asymptotic solution is taken as described in Bollati et al. (2021).
6. The solution $\chi(t, \eta)$ is transformed to $\chi(r, \phi)$ as described in Section 4.3.3.
7. The density perturbations in the non-linear regime are calculated from χ using Equations (3.115) and (4.11). The velocity perturbations are calculated from χ as described in Section 4.3.5. Again, all perturbations σ, u and v are assumed to be independent of z .

¹⁰https://github.com/DanieleFasano/Analytical_Kinks

¹¹<https://wakeflow.readthedocs.io/en/latest/tutorials/quickstart.html>

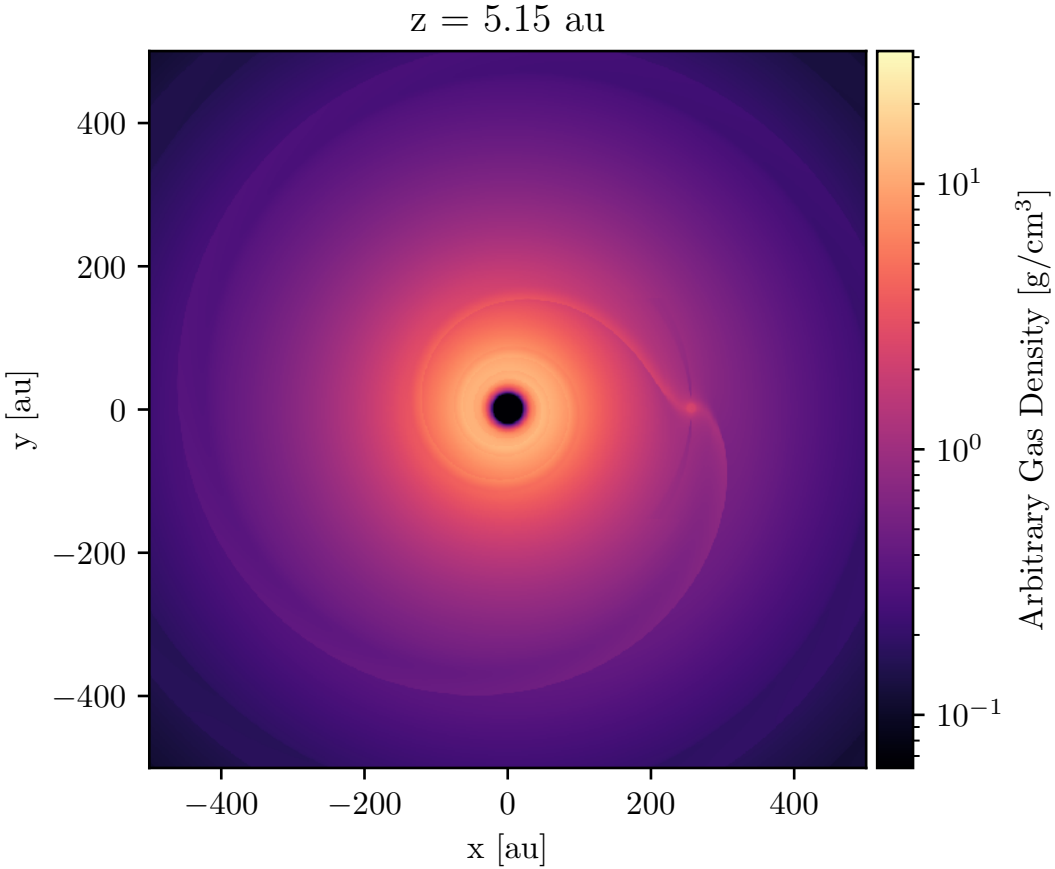


Figure 4.1: Density slice of a WAKEFLOW model at constant height $z = 5.15$ au, plotted with a logarithmic colourbar. The model contains a $0.5 M_J$ planet, placed at a separation of 256 au from the central star. These results were generated following the quickstart tutorial publicly available on the WAKEFLOW documentation¹¹, and are meant as a model of the planet wake in the disk of HD 163296, with disk parameters chosen following Pinte et al. (2018b) and Calcino et al. (2022).

8. The results are written to the disk. This output may be a `.fits` file if desired.

A density slice of an example WAKEFLOW model is shown in Figure 4.1. This model was calculated on a $1000 \times 1000 \times 30$ grid in x, y and z respectively, and took in 19.1 seconds to compute on an Apple M1 processor.

4.3 Theoretical and Numerical Considerations

4.3.1 Unperturbed disk structure

Here we outline the unperturbed disk model used in WAKEFLOW onto which the perturbations are added.

Temperature

We assume that the sound speed c obeys a simple radial power law

$$c \propto r^{-q}, \quad (4.1)$$

where q is some real number. Thus the disk temperature scales as

$$T \propto c^2 \propto r^{-2q}. \quad (4.2)$$

The constant of proportionality for these relations is determined by the user specified value of the disk aspect ratio H/r at $r = r_{\text{ref}}$

Density

We use a density structure derived by assuming that the disk is in vertical hydrostatic equilibrium (Pringle, 1981), but unlike in Equation (2.18) we will not assume that $z \ll r$. The density ρ is given by

$$\rho(r, z) \propto \left(\frac{r}{r_{\text{ref}}}\right)^{-p} \exp\left(\frac{GM_{\star}}{c^2} \left[\frac{1}{\sqrt{r^2 + z^2}} - \frac{1}{r}\right]\right), \quad (4.3)$$

where p is some real number. The constant of proportionality is set directly by the user, or calculated by MCFOST based on the total gas mass.

Very commonly the density profile is parameterised in terms of the surface density Σ , not the actual density ρ as above. If the surface density is parameterised as $\Sigma \propto r^{-\delta}$ where δ is some real number, then Equation (2.20) gives the approximate relation

$$p \simeq \frac{3}{2} - q + \delta, \quad (4.4)$$

which can be used to convert between density parameterisations. This conversion is only approximate in our context, since it does assume that $z \ll r$ and our density profile does not. However this turns out not to matter since δ will only show up in the $t(r)$ mapping which we will assume is the same for all z .

Velocities

The radial and vertical motions in the unperturbed disk are set to zero. The rotation is derived assuming radial force balance (e.g. Nelson et al., 2013) and is given by

$$\Omega(r, z) = \Omega_K \left[-(p + 2q) \left(\frac{H}{r}\right)^2 + (1 - 2q) + \frac{2qr}{\sqrt{r^2 + z^2}} \right]^{1/2}, \quad (4.5)$$

where Ω_K is as defined in Equation (2.1).

4.3.2 Linear box

The solution in the linear regime nearby the planet used in WAKEFLOW was calculated by Bollati (2020) and Bollati et al. (2021) by solving Equations (3.92) – (3.94) numerically, following the procedure outlined in Goodman and Rafikov (2001). Here, we simply read in their dimensionless calculations and scale them accordingly for our purposes. Figure 4.2 shows the u and v solutions presented in Bollati et al. (2021), in local cartesian coordinates x, y centred on the planet location. The x, y coordinates are scaled by the Mach-1 length $l_p = 2H_p/3$, while the perturbation are scaled by the planet mass in units of the thermal mass M_p/M_{th} .

Unlike Bollati et al. (2021), we do not include the linear regime results as a square box in the global solution. Instead, we take seriously the transformation (3.88), and interpret y as an arc-length instead of a true Cartesian coordinate, giving us an *annulus segment* instead of a *square box* (we will from now on refer to the former simply as the *linear box*). Indeed, when the χ initial condition is extracted from the edge of the box, this is the treatment used for y . It is therefore more honest to take this approach when mapping the linear solution onto the global grid, and has the added benefit of resulting in a more continuous solution. In addition, we allow for separate variation of the height (angular extent) and width (radial extent) of the box. This is motivated by considering that the box size was originally chosen as the Mach-1 length through an argument about resonance location (see Section 3.4). Since these locations are constant as ϕ varies, it is perfectly acceptable to extend the linear regime in the angular direction. The caveat to this is that the linear solution was derived in the shearing sheet approximation where the global geometry of the disk is not considered. The curvature of the y coordinate becomes more extreme as the box size increases angularly. By default, WAKEFLOW chooses the angular extent of the box to be the same as the radial extent, with a height of $4H_p/3$.

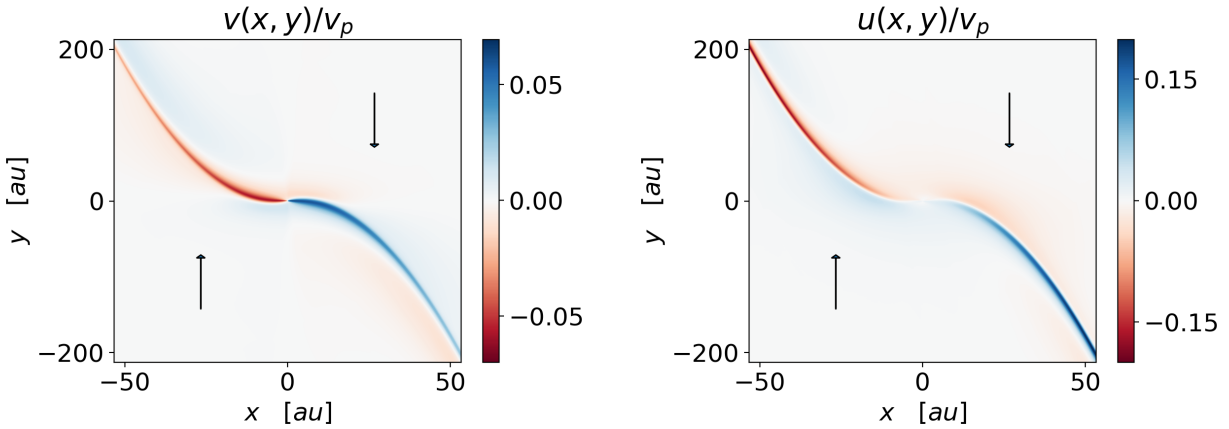


Figure 4.2: Linear azimuthal (left) and radial (right) velocity perturbations v and u centred on the planet in local cartesian coordinates as defined in Equations (3.87) and (3.88), and calculated by Bollati et al. (2021). The velocity is given in units of $v_p = \Omega_K(r_p)$, and the arrows denote the direction of the shearing gas flow in a frame centred on the planet.

4.3.3 Transformations

To perform transformation between the physical coordinates and (t, η) space in calculating our models, we apply the general forms of the transformations (3.116) – (3.118) to so-called *power-law disks* where the sound speed and surface density are parameterised as

$$c(r) = c_p \left(\frac{r}{r_p} \right)^{-q}; \quad \Sigma(r) = \Sigma_p \left(\frac{r}{r_p} \right)^{-\delta}, \quad (4.6)$$

where c_p and Σ_p are the sound speed and surface density at r_p . Assuming also that $\Omega = \Omega_K$, then Equation (3.120) becomes (Rafikov, 2002a)

$$\phi_{\text{wake}}(r) = \phi_p + \text{sgn}(r - r_p) \frac{r_p}{H_p} \left[\frac{2}{2q - 1} \left(\frac{r}{r_p} \right)^{q - \frac{1}{2}} - \frac{1}{q + 1} \left(\frac{r}{r_p} \right)^{q + 1} - \frac{3}{(2q - 1)(q + 1)} \right]. \quad (4.7)$$

Additionally, the Keplerian rotation implies $|2A| = 3\Omega/2 = 3c/2H$ and so the Mach-1 length becomes

$$l_p = \frac{2H_p}{3}, \quad (4.8)$$

and the η transformation (3.118) reduces to

$$\eta(r, \phi) = \frac{3r_p}{2H_p} [\phi - \phi_{\text{wake}}]. \quad (4.9)$$

Additionally the t transformation becomes (Rafikov, 2002a)

$$t(r) = \frac{3}{2^{5/4}} \left(\frac{r_p}{H_p} \right)^{\frac{5}{2}} \left| \int_1^{r/r_p} |s^{\frac{3}{2}} - 1|^{\frac{3}{2}} s^{\frac{5q+\delta}{2} - \frac{11}{4}} ds \right|, \quad (4.10)$$

where explicitly the g function is given by (Bollati et al., 2021)

$$g(r) = 2^{1/4} \left(\frac{r_p}{H_p} \right)^{\frac{1}{2}} \frac{\left(\frac{r}{r_p} \right)^{\frac{5}{4} - \frac{\delta+3q}{2}}}{\left| 1 - \left(\frac{r}{r_p} \right)^{\frac{3}{2}} \right|^{\frac{1}{2}}} \quad (4.11)$$

This gives us all the tools we need to map from (r, ϕ) space to (t, η) space in a Keplerian power law disk. These are the forms of the transformations used by WAKEFLOW. We are therefore implicitly

assuming that the unperturbed rotation profile is well approximated as Keplerian in the mid-plane, which is reasonable since the correction is of order $(H/r)^2$.

Unlike in Goodman and Rafikov (2001); Rafikov (2002a); Bollati et al. (2021) we do not use approximate forms of the transformations that hold nearby the planet in the shearing sheet approximation to extract the initial condition for the Burger's evolution. We found that the approximate transformation for η (Equations 35 in Rafikov, 2002a) shifted the wake profile in η by a few percent, leading to a discontinuity in the solution at the interface between the linear and non-linear regimes. The approximate t transformation has a similar effect although it is much smaller. For this reason we always use the exact transformations as listed above.

Previously Bollati et al. (2021) assumed that the initial condition for the inner ($r < r_p$) and outer ($r > r_p$) wake propagation were identical and so solved only the outer wake case and copied the solution for the inner wake. This approximation does not hold well except for very small values of $(H/r)_p$, as the radial extent of the box results in different t coordinates at the inner and outer edge of the box in general. For this reason we instead solve separately the inner and outer wake propagation, taking the appropriate initial condition for each (Fasano et al., in prep.).

After Burger's equation is solved numerically, the solution must be mapped from $\chi(t, \eta)$ to $\chi(r, \phi)$. Since $t(r)$ is not invertible, we instead find the (t, η) coordinates of every point on the solution grid (r, ϕ) and interpolate from the Burger's solution in t, η space. We therefore must evaluate the $t(r)$ and $\eta(r, \phi)$ transformations N times, where N is the number of points in the grid. The η transformation is easily vectorised since it is a simply algebraic expression, however the $t(r)$ transformation (4.10) involves an integral which naively must be evaluated N times. This approach is very inefficient, since the integral in the transformation does not actually depend on r , merely the end point does. Re-evaluating the integral each time therefore often involves integrating over the same interval very many times. In WAKEFLOW we instead convert mapping $r \rightarrow t$ into an initial value problem (IVP). Since the integrand of Equation (3.117) is independent of r , we can convert Equation (3.117) into an ordinary differential equation with an appropriate initial condition

$$\frac{dt(s)}{ds} = \frac{r_p}{l_p} \left[\frac{\Omega(s) - \Omega_p}{c_0(s)g(s)} \right]; \quad t(r_p) = 0. \quad (4.12)$$

where obtaining $t(r)$ from the solution $t(s)$ is simply a matter of taking $s = r$. Applying this analysis to the t transformation for a power law disk (4.10) we obtain

$$\frac{dt(s)}{ds} = \frac{3}{2^{5/4}} \left(\frac{r_p}{H_p} \right)^{\frac{5}{2}} \left| s^{\frac{3}{2}} - 1 \right|^{\frac{3}{2}s^{\frac{5q+\delta}{2}-\frac{11}{4}}}; \quad t(1) = 0, \quad (4.13)$$

and $t(r)$ is obtained from the solution taking $s = r/r_p$. WAKEFLOW calculates the t coordinates of the grid points by solving the IVP (4.13) using the SCIPY function `integrate.odeint` (Virtanen et al., 2020).

4.3.4 The high mass regime

Author Statement: This subsection presents a short summary of an upcoming paper, Fasano et al. (in prep.). For this paper I contributed numerous improvements to the code used to generate the semi-analytic models¹², provided the code used to extract relevant quantities from the SPH models¹³ and provided feedback on the manuscript.

Before we discuss our final improvement to the semi-analytic models, a higher order accuracy mapping from χ to the velocity perturbations u and v , we will briefly address the question of the validity of the semi-analytic wake solution for planet masses of order M_{th} . While Cimerman and Rafikov (2021) performed a numerical validation of the models for the mass range $\leq \frac{1}{2}M_{\text{th}}$, we are particularly interested in more massive planets. In Fasano et al. (in prep.) we will present detailed comparisons between simulations performed with the smoothed particle hydrodynamics (SPH) code

¹²https://github.com/DanieleFasano/Analytical_Kinks

¹³https://github.com/TomHilder/wakeflow/blob/legacy-code-format/phantom_chi_extraction.py

PHANTOM (Price et al., 2018) and the semi-analytic models, in the high mass regime with planet masses $\gtrsim M_{\text{th}}$. We will summarise the main findings of that work here.

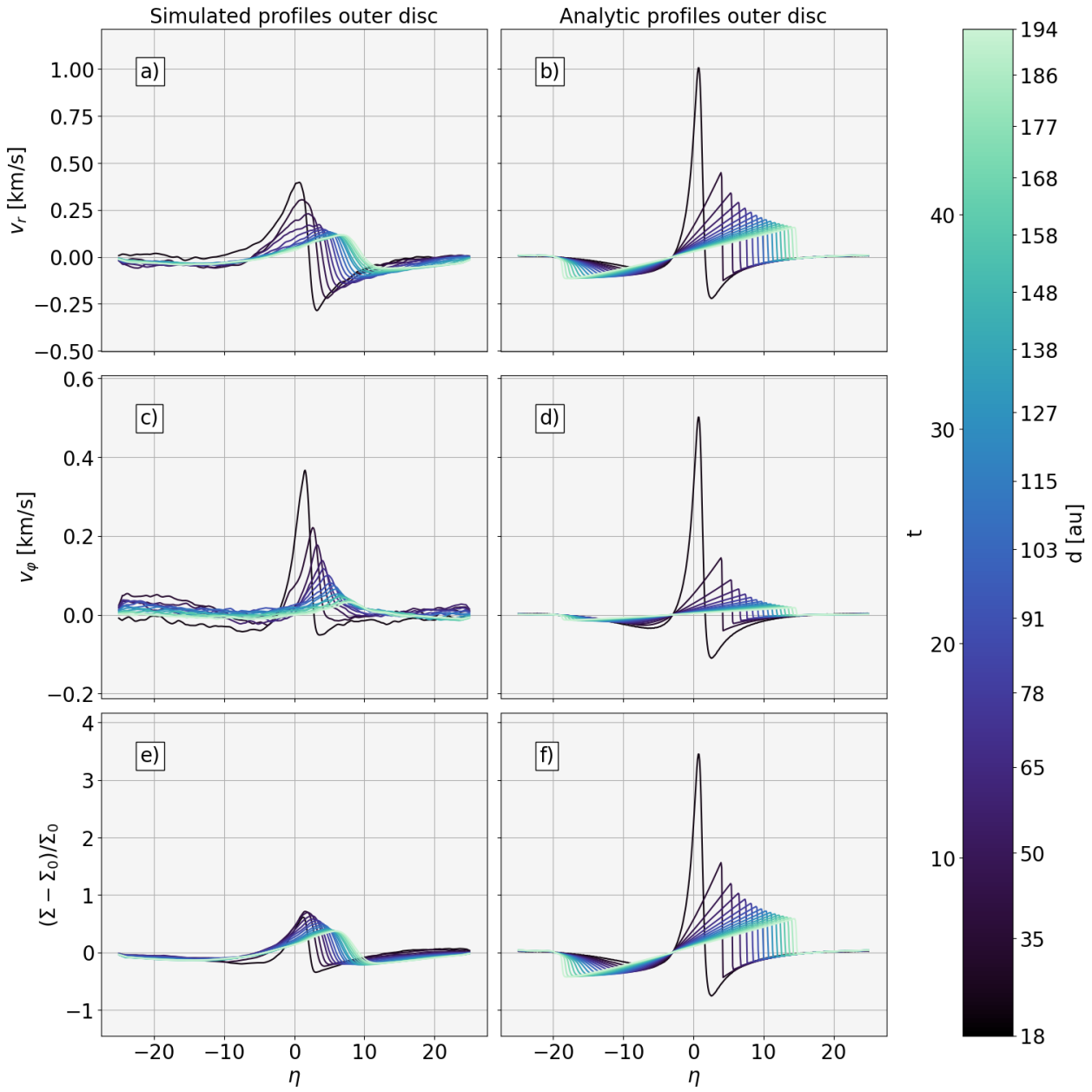


Figure 4.3: Comparison between SPH (left) and semi-analytic (right) solutions for the perturbations induced by a $3.87 M_{\text{th}}$ planet with orbital radius $r_p = 95.7$ au. Wake profiles taken as slices of constant t , or equivalently r are shown. The radial velocity, azimuthal velocity and density perturbations shown from top to bottom. The colourbar indicates the t coordinate for each profile, as well as the physical distance d from the planet location. Figure taken from Fasano et al. (in prep.).

For planet masses greater than M_{th} , the linear solution is no longer valid as the wake should shock before it is fully formed (Goodman and Rafikov, 2001). It is then impossible to spatially separate the wake evolution neatly into the linear and non-linear regimes. Ignoring this issue and calculating the semi-analytic models as usual introduces a few issues that we found to be discrepant with the simulation results. Firstly, the wake structure in the linear box does not match that of the simulated models, and over-predicts the amplitude of the perturbations. A sharp spatial discontinuity is also formed at the boundary between the linear and non-linear regimes, since the very large linear perturbation initial condition results in rapid shock formation in the non-linear regime. This discontinuity is visible in Figure 4.7, and is more extreme for the radial velocity perturbations than for the azimuthal velocity or

density perturbations. We also found an additional discontinuity over the box edge in the amplitude of the velocity perturbations, with the perturbation just outside the linear box being far greater than that just inside.

However, moving away from the planet and deeper into the non-linear regime, the agreement between the analytical and simulated models improves. Figure 4.3 shows the outer wake profile as it evolves in t for $3.87 M_{\text{th}}$, compared between both models. Remarkably, the accuracy in the non-linear regime seems to improve as t increases. The amplitude for each of the perturbations is in good agreement between the models after the wake was propagated only a few tens of au from the planet location. The shocks produced by the inviscid Burger's equation evolution are however steeper than those found in the SPH model, likely due to the finite resolution of the simulation (Lodato and Price, 2010). The wake profiles are more extended in η in the analytics, but we do not seem to recover the over-damping found in the low mass regime by Cimerman and Rafikov (2021). The position of the outer shock in density, and so the shape of the wake, is also different between the models. This is not surprising as the pitch angle of the spiral increases and deviates from the linear shape used in the analytics (3.120) for high mass planets Zhu et al. (2015). It may be possible to calibrate for this increase in pitch angle from non-linear effects, see Section 5.2 of Cimerman and Rafikov (2021) for more details.

The apparent accuracy of the solution in the semi-analytical model far from the planet in the high mass case is perhaps not surprising when considered in the context of the existence of the asymptotic solution given in Section 3.5.2. The more massive planets result in faster shock formation in the Burger's equation evolution, and so it makes at least qualitative sense that the asymptotic solution may also become valid earlier. The agreement between the analytics and simulations for $t \gtrsim 10$ may therefore reflect that the solution quickly becomes independent of the initial condition, and that the asymptotic scaling in χ holds well for high planets resulting in the correct non-linear behaviour at some distance from the planet. We defer further discussions of accuracy, including a full parameter study and a preliminary calibration of the semi-analytic method, to Fasano et al. (in prep.).

4.3.5 Velocity perturbations

Following the method of Bollati et al. (2021) to calculate the velocity perturbations in the non-linear regime results in a discontinuous solution at the edge of the linear box. The calculated amplitude of the velocity perturbations for $t > t_0$ is significantly less than that at the start of the non-linear solution where $t - t_0$ is small¹⁴ (Fasano et al., in prep). To investigate this discontinuity in velocity amplitude we re-derived the mapping from χ to u and v from Rafikov (2002a) and Bollati et al. (2021). As we saw in Section 3.5 the conservation of the Riemann invariant R_+ gives for the radial velocity perturbation

$$u = 2 \frac{c_0 - c}{\gamma - 1} = -2 \frac{c_0}{\gamma + 1} \psi, \quad (4.14)$$

where we define ψ as

$$\psi = \frac{\gamma + 1}{\gamma - 1} \frac{c - c_0}{c_0}, \quad (4.15)$$

which is the sound speed perturbation with a constant scale factor. Following Rafikov (2002a), we then derive an expression for ψ in terms of the density perturbation χ by assuming that the gas obeys a locally polytropic equation of state given by

$$P = P_0(r) \left[\frac{\Sigma}{\Sigma_0(r)} \right]^\gamma. \quad (4.16)$$

The sound speed is then

$$c^2 = \frac{\partial P}{\partial \Sigma} = c_0^2(r) \left[\frac{\Sigma}{\Sigma_0(r)} \right]^{\gamma-1}. \quad (4.17)$$

¹⁴Recall that t_0 is the t coordinate at the transition between the linear and non-linear regimes.

Rafikov then finds a relation between the density and sound speed perturbations, to second order in ψ , by expanding the above expression. This yields

$$\frac{\Sigma - \Sigma_0}{\Sigma_0} = \frac{2}{\gamma + 1} \psi + \frac{3 - \gamma}{(\gamma + 1)^2} \psi^2 + \mathcal{O}(\psi^3). \quad (4.18)$$

Taking this expression to first order only, we write u in terms of the density perturbation, and then in terms of χ by substituting Equation (3.115).

$$u = -c_0 \frac{\Sigma - \Sigma_0}{\Sigma_0} = -2 \frac{c_0}{\gamma + 1} \frac{\chi}{g(r)}. \quad (4.19)$$

Similarly, Rafikov (2002a) finds the azimuthal velocity as

$$v \approx -2 \frac{c_0^2}{\Delta \Omega r} \frac{1}{\gamma + 1} \psi, \quad (4.20)$$

giving to first order in ψ

$$v \approx -\frac{c_0^2}{\Delta \Omega r} \frac{\Sigma - \Sigma_0}{\Sigma_0} = -\frac{2}{\gamma + 1} \frac{c_0^2}{\Delta \Omega r} \frac{\chi}{g(r)}. \quad (4.21)$$

Equations (4.19) and (4.21) are the expressions used in Bollati et al. (2021) to calculate the velocity perturbations in the non-linear regime. Since these are only accurate to first order in ψ , the assumption is made that $\psi \ll 1$, which is the weak shock approximation introduced in Section 3.5. Since we are in particular interested in the velocity perturbations in the context of kinematics, and in planet masses comparable to the thermal mass, we should check if the assumption that $\psi \ll 1$ still holds for planets in the high mass regime.

We can derive an *exact* expression for ψ in terms of the density perturbation simply by rearranging Equation (4.16). We find

$$\psi = \frac{\gamma + 1}{\gamma - 1} \left[\left(\frac{\Sigma - \Sigma_0}{\Sigma_0} + 1 \right)^{(\psi-1)/2} - 1 \right], \quad (4.22)$$

which can be written equivalently in terms of χ using Equation (3.115) giving

$$\psi = \frac{\gamma + 1}{\gamma - 1} \left[\left(\frac{2}{\gamma + 1} \frac{\chi}{g(r)} + 1 \right)^{(\psi-1)/2} - 1 \right]. \quad (4.23)$$

We used Equation (4.23) to check the aforementioned assumption that $\psi \ll 1$ in the non-linear regime solution. We constructed three WAKEFLOW models using dimensionless units, with embedded planet masses of 0.5, 1.0 and 2.0 M_{th} respectively, all placed in orbit around a $1 M_{\odot}$ star at an orbital radius of $r = 1$. For all models, we chose $p = 2.25$ and $q = 0.25$ such that $\Sigma \propto r^{-1}$, and an aspect ratio $H/r = 0.1$ at $r = 1$. Figure 4.4 shows the values of ψ for each of these models, and demonstrates that even for the lowest planet mass model the value of ψ nearby the planet is as large as ~ 0.6 and so the second order terms will clearly be important even in this case. For masses $\geq M_{\text{th}}$ the problem is even worse, as there are regions where $\psi \gtrsim 1$ causing the expansion given in Equation (4.18) to diverge.

The choice of taking (4.18) to first order is justified in Bollati et al. (2021) by noting that terms proportional to ψ^2 are discarded in the derivation of the Burgers evolution (3.114), and thus also in the calculation of χ from which u and v are calculated. The u and v calculated by their method are thus those that are consistent with the solution to Burger's Equation (3.114). However it is not clear that this gives the most physically reasonable results. The argument for the velocities follows by relating the sound speed perturbation to the density perturbation through the equation of state (4.16). However it is not clear that truncating the equation of state for density perturbations calculation *necessitates* that the same truncation must be performed to find physically realistic velocity perturbations.

In order to obtain velocity perturbations that more closely match hydrodynamical simulations, and to reduce the amplitude discontinuity over the box, we derived expressions for both u and v

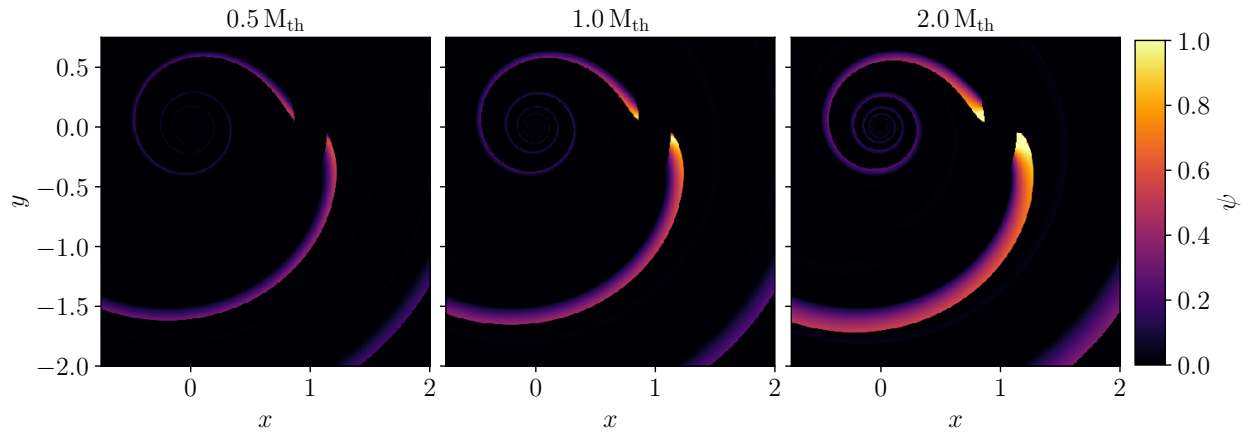


Figure 4.4: Comparison of the values of ψ calculated from Equation (4.23) for three WAKEFLOW models with planet masses of $0.5, 1.0$ and $2.0 M_{\text{th}}$ respectively. Clearly one cannot assume that $\psi \ll 1$ even for the lowest mass model, especially nearby the planet. For the two larger masses, there are even regions where $\psi > 1$.

as functions of χ without truncating the equation of state to first order in ψ . This is as simple as substituting Equation (4.23) into Equations (4.14) and (4.20), yielding

$$u(\chi) = -2 \frac{c_0}{\gamma - 1} \left[\left(\frac{2}{\gamma + 1} \frac{\chi}{g(r)} + 1 \right)^{(\psi-1)/2} - 1 \right] \quad (4.24)$$

$$v(\chi) \approx \frac{c_0}{\Delta \Omega r} u(\chi). \quad (4.25)$$

Figures 4.5, 4.6 and 4.7 show a comparison of the velocities calculated from the above with those calculated to first order in ψ , for planet masses of $0.5, 1.0$ and $2.0 M_{\text{th}}$ respectively. These are the same models as those used to create Figure 4.4. The plots are centred on the planet location, and they show that even for the lowest mass case the amplitude discontinuity is improved significantly for the radial perturbations by the new extraction using Equation (4.24). This affect is increasingly significant for the more massive planets as can be seen in the 1.0 and $2.0 M_{\text{th}}$ cases. The azimuthal velocity case is however minimally affected. It is unclear why the radial perturbation is improved while the azimuthal perturbation is not. However the derivation for $u(\psi)$ in Rafikov (2002a) comes from the conservation of the Riemann invariant R_+ , while $v(\psi)$ is found in terms of u by taking Equation (3.106) and the terms $u \partial_\phi v$ and $uv/(\Delta \Omega r)$. We conjecture that these terms are also important for larger mass planets, and that they could be responsible for the lack of improvement in the v mapping.

Due to the reduction in the amplitude discontinuity, Equations (4.24) and (4.25) are used to calculate the velocity perturbations in the non-linear regime in WAKEFLOW.

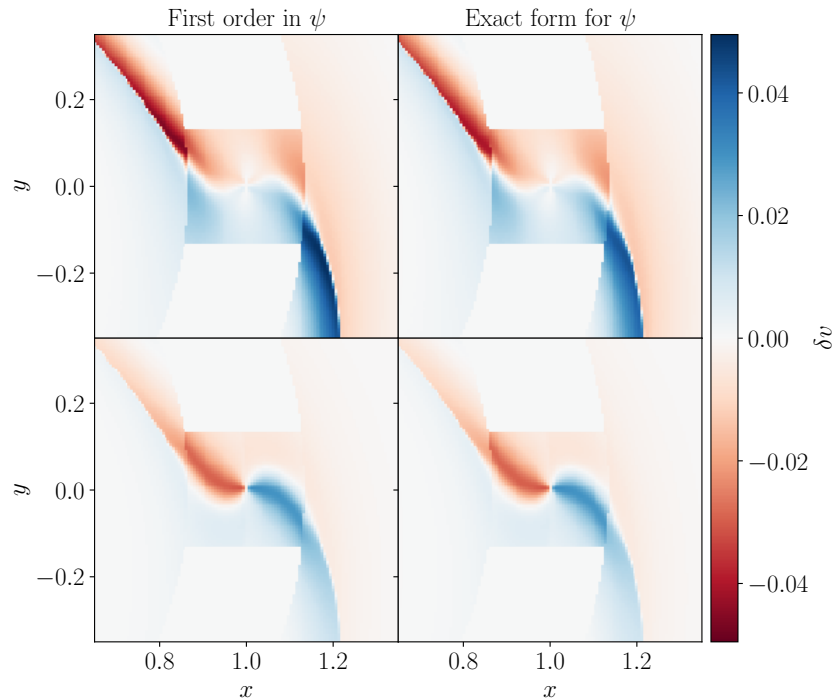


Figure 4.5: Comparison of the velocity perturbations calculated in the non-linear regime between the method of [Bollati et al. \(2021\)](#) which is first order accurate in ψ (left), and by using Equations (4.24) and (4.25) which use the exact form for ψ (right). The dimensionless radial velocity and azimuthal velocities are shown in the top and bottom panels respectively. The planet mass used in the model is $0.5 M_{\text{th}}$. We see that the amplitude discontinuity is improved somewhat for the radial velocities, and basically unaffected for the azimuthal velocities.

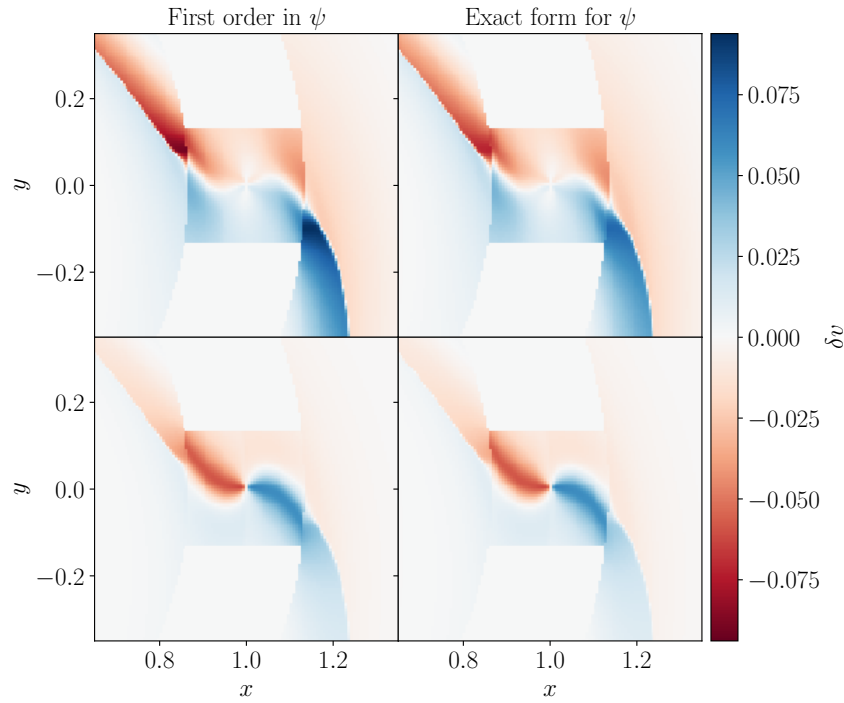


Figure 4.6: As in Figure 4.5, except for a planet mass of $1.0 M_{\text{th}}$. We see that the amplitude discontinuity is significantly improved for the radial velocities, but not for the azimuthal velocities.

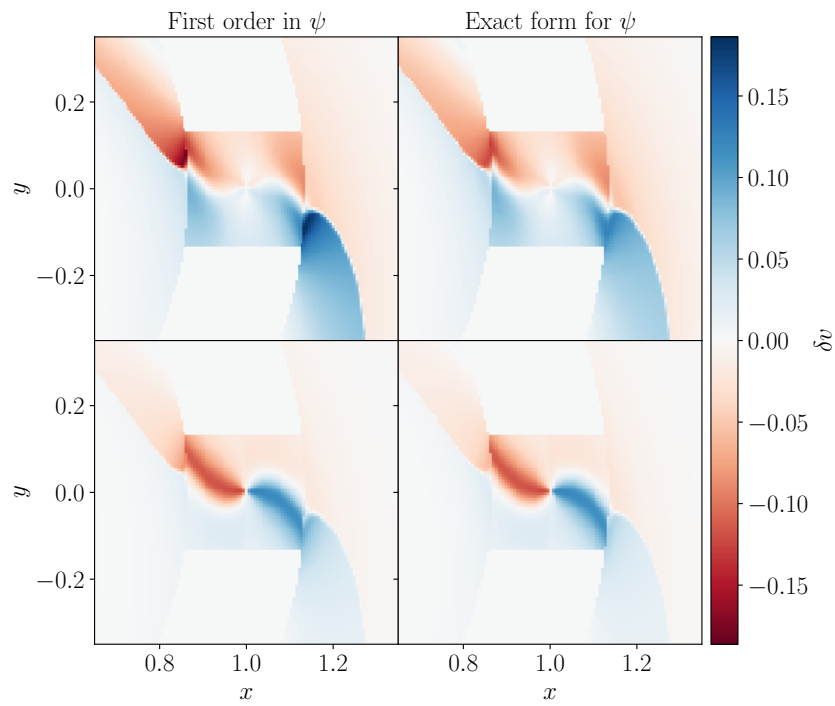


Figure 4.7: As in Figure 4.7, except for a planet mass of $2.0 M_{\text{th}}$. We see that the amplitude discontinuity is again significantly improved for the radial velocities, while unaffected or even slightly worse for the azimuthal velocities.

5

HD 169142 and IM Lupi: Applications of the Models

Here we present two examples of work, led by others, that has already been done making use of the models and ideas developed in chapters 4 and ([Calcino et al., 2022](#)). In the first, we apply the semi-analytic models to test the hypothesis that the kinematic arc detected in the disk of HD 169142 is caused by a planet wake. The second uses the linear wake theory to map the planet wake in the disk of IM Lupi through the peak velocity map from kinematic observations.

5.1 The Kinematic Arc in HD 169142

Author Statement: This section presents the semi-analytical modelling performed as a part of [Garg et al. \(2022\)](#), which is publicly available at [arXiv:2210.10248](https://arxiv.org/abs/2210.10248). For this paper, I contributed the semi-analytic models used, advised the lead author on how to work with them, and provided feedback on the manuscript.

5.1.1 Introduction

HD 169142 is a disk-hosting Herbig Ae star located in the constellation of Sagittarius, at a distance of 117 ± 4 pc ([Gaia Collaboration et al., 2016](#)). The system's circumstellar disk appears almost face-on in the sky with an inclination of just 13° ([Raman et al., 2006](#); [Panić et al., 2008](#)). The disk contains bright dust ring substructures at ~ 25 au and ~ 65 au, as well as a central cavity with radius ~ 22 au. These features have been observed through different tracers including scattered light ([Quanz et al., 2013b](#); [Momose et al., 2015](#); [Pohl et al., 2017](#); [Bertrang et al., 2018](#)) mid-infrared ([Honda et al., 2012](#)), sub-millimetre with ALMA ([Fedele et al., 2017](#); [Macías et al., 2019](#); [Pérez et al., 2019](#)) and centimetre with the Very Large Array ([Osorio et al., 2014](#)). The highest resolution of these studies showed that the outermost ring is actually three distinct rings separated by approximately 10 au. Various candidate point source detections have been made near the $r \approx 25$ au ring ([Biller et al., 2014](#); [Reggiani et al., 2014](#); [Gratton et al., 2019](#)), but are disputed due to the possible confusion with disk material in their analyses ([Ligi et al., 2018](#)).

This paper presents ALMA band 6 observations of the circumstellar disk around HD 169142. We imaged the ^{12}CO , ^{13}CO and C^{18}O $J = 2 - 1$ spectral lines at a resolution of 0.167 km/s, taking into account the Hanning Smoothing caused by the correlator. The obtained angular resolutions of $0.07''$ and $0.1''$ allowed us resolve both density and kinematic substructures in the gas. Here, we will focus on the ^{12}CO observations and on modelling the kinematics with the analytics.

5.1.2 Observations and analysis

We imaged the $J = 2 - 1$ line transitions of ^{12}CO , ^{13}CO and C^{18}O using ALMA band 6 observations from projects [2015.1.00490.S] and [2016.1.00344.S]. For details of the self-calibration and data reduction process, see [Garg et al. \(2022\)](#).

From Equation (2.21), the rotation velocity of the gas in a pressure-supported disk is given by

$$\frac{v_{\text{gas}}^2}{r} = \frac{GM_{\star}r}{(r^2 + z^2)^{3/2}} + \frac{1}{\rho_{\text{gas}}} \partial_r P_{\text{gas}}, \quad (5.1)$$

where the first term is the typical Keplerian rotation and the second is the contribution by the radial pressure gradient. As discussed in section 2.2.2, the second term typically results in sub-Keplerian motions. To find kinematic substructures in the data, we wish remove the background motions of the disk associated with Equation (5.1) to isolate only the deviations from the bulk flow. As a first step, we compute peak velocity v_0 maps by spectrally collapsing the data cube using the PYTHON package BETTERMOMENTS ([Teague and Foreman-Mackey, 2018](#)). We chose specifically to use the *Gaussian* method since it provides also the velocity error for each pixel δv_0 and has minimal statistical uncertainty ([Yu et al., 2021](#)).

To obtain only the deviations from bulk rotation in v_0 , we made use of the PYTHON package EDDY ([Teague, 2019](#)). EDDY subtracts a best-fitting Keplerian rotation profile using a Markov Chain Monte Carlo (MCMC) method ([Foreman-Mackey et al., 2013](#))¹⁵. We fit for the disk position angle (PA), central star mass M_{\star} , central star pixel location (x_0, y_0) and systemic velocity v_{syst} . For the MCMC, we used 250 walkers and ran for 10,000 steps. The data used in the fit were also restricted to within 1.5" from the centre of the image, as outside of this region was noise dominated. The inner 0.2", equal to twice the beam width, was also excluded to avoid any bias resulting from beam smearing in the inner disk. From fitting the ^{12}CO data, we found best-fitting model parameters of $\text{PA} = 5.33^\circ$, $M_{\star} = 1.47 M_{\odot}$, and $v_{\text{syst}} = 6.897 \text{ km/s}$.

To account for the pressure term of Equation (5.1), we need the radial pressure gradient $\partial_r P_{\text{gas}}(r)$. Assuming an ideal gas equation of state, the pressure is given by

$$P_{\text{gas}}(r) = n_{\text{gas}} k_{\text{B}} T(r), \quad (5.2)$$

where n_{gas} is the gas number density, k_{B} is Boltzmann's constant and $T(r)$ is the temperature profile. We calculated n_{gas} and $T(r)$ from the azimuthally averaged gas column density and brightness temperature profiles respectively, see [Garg et al. \(2022\)](#) for further detail.

Finally, we made use of the best-fitting Keplerian rotation model, plus the radial pressure gradient, to subtract the bulk rotation from the peak velocity maps of the data to create kinematic residuals. The result is shown in Figure 5.1, along with the associated statistical significance. We detect a kinematic excess of angular extent $\sim 105^\circ$ and magnitude $\sim 75 \text{ m/s}$ on the north side of the disk. The excess is located between the 26 au and 59 au dust rings thus has a radial extent of approximately 30 au. The kinematic arc feature was however not detected in ^{13}CO and C^{18}O , which may owe to the lower integration time of those observations, or may reflect that the rotation nearer to the mid-plane is less perturbed.

5.1.3 Semi-analytical modelling

Notably, the feature we detected overlaps with the point source found in [Gratton et al. \(2019\)](#) at a PA of 43.8° and radial separation of 38 au. If the point source is indeed a planet, perhaps the kinematic arc is associated with the velocity perturbations induced by the tidal forcing of the planet. To test this scenario, we constructed semi-analytic models of the wake produced by a planet placed in the disk at the location of the [Gratton et al. \(2019\)](#) point source using WAKEFLOW. We chose power law profiles

¹⁵The main point of using MCMC over a traditional optimisation methods is to obtain the uncertainties in the best fitting parameters by estimating the posterior distribution. However, we found that the error-bars we obtained were too small to be physically realistic, and so in appendix C of [Garg et al. \(2022\)](#) we provide a parameter study around the best fit to investigate the true uncertainty.

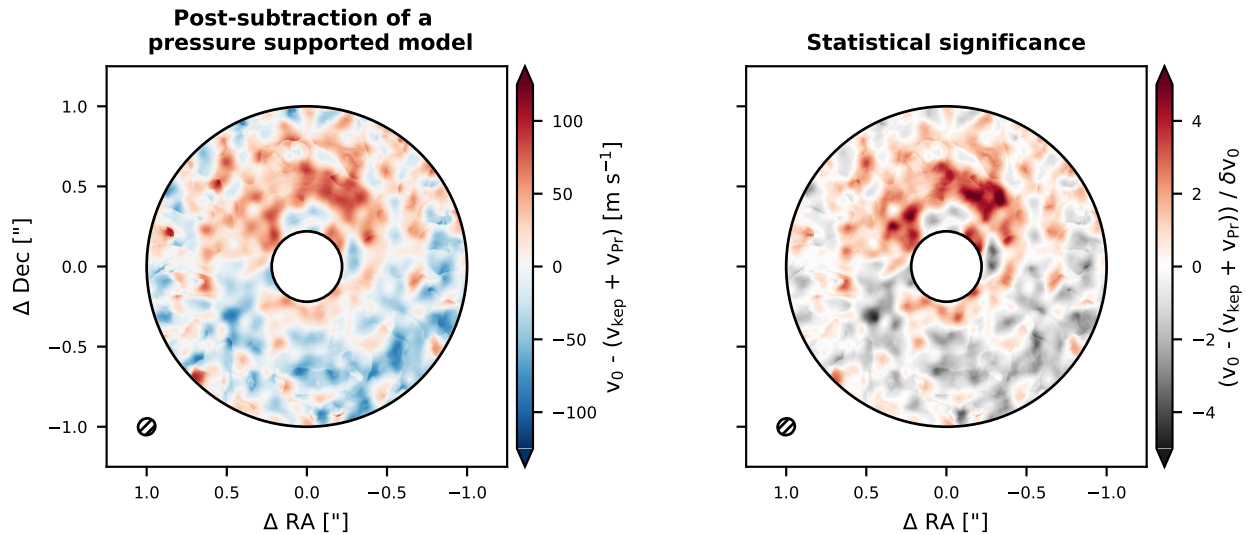


Figure 5.1: Velocity residuals of the ^{12}CO observations of HD 169142 calculated by the subtraction of a rotation profile including pressure support (left). Also shown is the residual velocities divided by the uncertainty in the peak velocity (right). The beam size is plotted in the bottom left corner of each panel, while the masked inner and outer regions are filled white (Garg et al., 2022).

for the unperturbed disk of $c \propto r^{-0.2}$ and $\Sigma \propto r^{-1}$, as well as an aspect ratio of $(H/r)_p = 0.08$. The central star mass was chosen as $M_\star = 1.47 M_\odot$ from the best-fitting model described in the previous section. We used two M_p values of $1 M_J$ and $10 M_J$.

After the WAKEFLOW models were calculated, we used the Monte Carlo radiation transfer code MCFOST (Pinte et al., 2006, 2009) to generate synthetic ^{12}CO $J = 2 - 1$ observations. The total gas mass of the model was set to $10^{-2} M_\odot$ (Toci et al., 2019) and the gas-to-dust ratio was set to 100. We use Mie theory (Mie, 1908) to calculate the optical properties of the dust grains, and assume that their size a is distributed as $dn(a) \propto a^{-3.5} da$ where $n(a)$ is the number density of grains with size a . The range of dust grain sizes used was between $0.03 \mu\text{m}$ and 1 mm, and they were taken to have a silicate composition (Weingartner and Draine, 2001). We assumed equal dust and gas temperatures, as well as local thermodynamic equilibrium. The central star was modelled as an isotropically radiating blackbody, and 12.8×10^6 packets were used to compute the dust temperature structure. The relative CO abundance was taken to be 10^{-4} , and the effects of CO freeze-out at $T < 20\text{ K}$, as well as photodissociation and photodesorption in regions of high UV were included (Pinte et al., 2018a). The resultant channel maps had a channel spacing of 32 m/s, and the synthetic cubes were subsequently convolved spatially with a Gaussian of width 0.1" to replicate the beam size in the observations, as well as spectrally with a Hanning function of width 167 m/s to replicate the effects of the correlator.

To create sky-plane velocity residuals, the cubes were collapsed spectrally in the same way as for the observations. This whole process was then repeated except for models with no planet, and residuals were calculated as the difference between the two velocity maps. These residuals are presented in Figure 5.2. Comparing these with Figure 5.1, we see that in neither case do the analytic models recreate the arc found observationally. The $1 M_J$ planet model contains kinematic deviations that are far smaller than those observed. On the other hand, the $10 M_J$ produces residuals that while similar in amplitude, differ from the observations in shape, location and sign. Of the two models, the $10 M_J$ is more compatible with the observations but it still performs poorly.

Since the disk is nearly face-on, the observed kinematic structure may be dominated by vertical motions which are absent in the analytical models. This may help to explain why the arc was absent in the ^{13}CO and C^{18}O observations, since these trace the disk structure closer to the mid-plane. For example, buoyancy spirals (Zhu et al., 2012; Bae et al., 2021) excited by the planet in a thermally-stratified disk can result in significant vertical motions in the upper layers of the disk. The planet wake in the mid-plane is expected to be dominated by radial motions (Rafikov, 2002a), which would be hard to detect given the orientation of the disk.

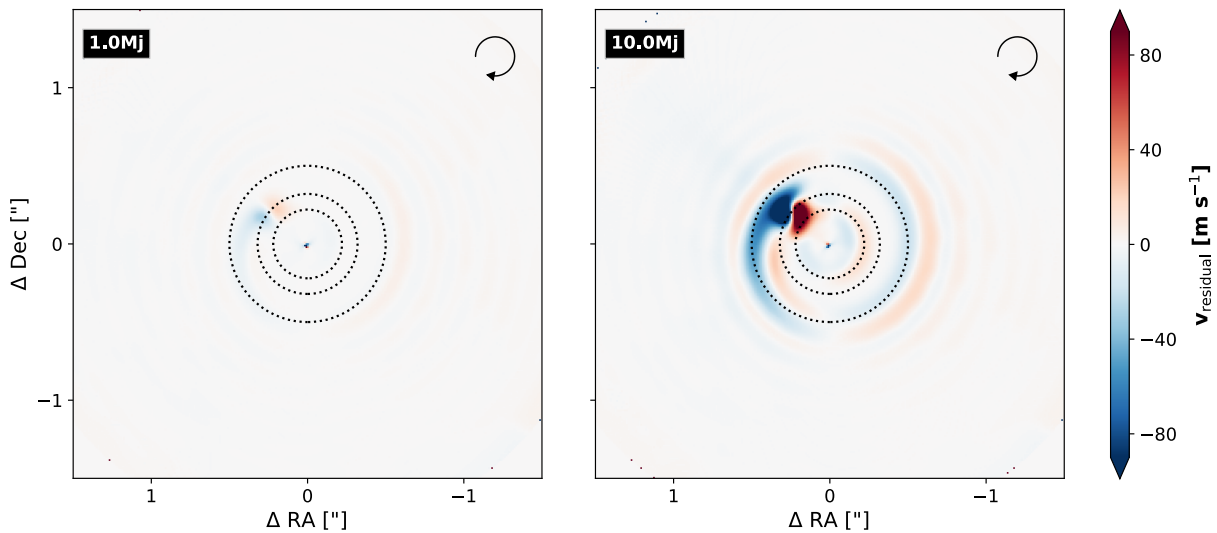


Figure 5.2: Velocity perturbations from bulk rotation resulting from the tidal forcing of an embedded planet, calculated using WAKEFLOW and MCFOST. The $1 M_J$ planet mass model is shown on the left, while the $10 M_J$ model is shown on the right. The rotation direction of the disk is shown in the top-right of each panel (Garg et al., 2022).

A significant limitation to the analysis performed here is the accuracy of the WAKEFLOW models nearby the planet. Given the disk aspect ratio and central star mass, the thermal mass is only $\sim 0.5 M_J$. Thus the two models we have used here contain planets of masses $2 M_{\text{th}}$ and $20 M_{\text{th}}$. In both of these cases the perturbations calculated close to the planet will be overestimated (Fasano et al., in prep.). Unfortunately, in this case that is the region we are specifically interested in. It is therefore only reasonable to interpret these results as upper bounds on the size of the perturbations that may be induced by the planet mass in each model. We thus conclude that to explain the kinematic excess we have detected in the disk through our model requires an embedded planet of no more than $10 M_J$.

5.2 The Planet Wake in IM Lupi

Author Statement: This section presents part of Verrios et al. (2022), which is publicly available at [arXiv:2207.02869](https://arxiv.org/abs/2207.02869). For this paper, I provided the code used to create and project the wake shape to the emitting surface¹⁶, created Figure 4 in collaboration with the lead author (Figure 5.3 here), and provided feedback on the manuscript.

5.2.1 Introduction

The young star IM Lupi is host to a large and spectacular circumstellar disk (Panić et al., 2009; Avenhaus et al., 2018; Cleeves et al., 2016; Pinte et al., 2018a). Localised deviations from Keplerian motion were found across multiple velocity channels in ^{12}CO line emission observations (Pinte et al., 2020) taken as part of DSHARP (Huang et al., 2018b; Andrews et al., 2018a). Higher spatial resolution observations from MAPS (Öberg et al., 2021) confirm the presence of these velocity kinks, which Pinte et al. (2020) hypothesised to be induced by the gravitational disturbance from an embedded planet orbiting at 117 au. This separation is too large to facilitate the detection of such a planet through traditional methods like radial velocities or transits, and the optically thick dust and gas material complicates direct imaging.

Scattered light images of the disk reveal large, tightly-wound spiral structures in the disk surface (see Figure 2.2; Avenhaus et al., 2018), while 1.25 mm continuum observations from DSHARP show also spiral arms and gaps in the dust-disk present in the mid-plane (see row 2 panel 1 of Figure 2.5;

¹⁶<https://github.com/TomHilder/spiralmoments>

Huang et al. 2018b). Are these spirals caused by the embedded protoplanet? An alternative explanation is that they are formed through gravitational instabilities, which produce disordered flocculent spirals and hence “kinks everywhere” (Hall et al., 2020). On the other hand, planets should produce velocity kinks only along the coherent one-armed planet wake. The gravitational instability requires that the disk is self-gravitating and so massive, which is not required by the planet model.

In this letter we investigated whether an embedded planet can produce both the observed spiral structures and the observed kinematic features. Here, we present the portion of the letter concerned with tracing the planet wake in the kinematics, similarly to in Calcino et al. (2022).

5.2.2 Simulated model

We used the PHANTOM SPH code (Price et al., 2018) to create models of the interaction between the disk of IM Lupi and an embedded planet. A disk of mass $0.01 M_{\odot}$ was modelled using ten million SPH particles, set to initially follow the density profile

$$\Sigma(r) \propto \left(\frac{r}{r_{p,i}}\right)^{-p} \exp\left[-\left(\frac{r}{r_c}\right)^{2-p}\right], \quad (5.3)$$

We used $p = 0.48$ (Pinte et al., 2018a) and $r_c = 150$ au. We assumed a locally isothermal equation of state with $c \propto r^{-0.31}$, and a disk aspect ratio of $H/r = 0.129$ at $r = 100$ au. The central star was modelled as a sink particle (Bate et al., 1995), with a mass of $1.12 M_{\odot}$ (Andrews et al., 2018a) and an accretion radius of 1 au. We included dust in the simulations using the MULTIGRAIN one-fluid algorithm (Price and Laibe, 2015; Ballabio et al., 2018; Hutchison et al., 2018; Price et al., 2018). We used 11 distinct grain sizes, logarithmically spaced between $a_{\min} = 1.0 \mu\text{m}$ and $a_{\max} = 2300 \mu\text{m}$ and following a distribution given by $dn(a) \propto a^{-3.5} da$. The gas to dust ratio was set as 57 resulting in a total dust mass of $1.7 \times 10^{-3} M_{\odot}$ following (Pinte et al., 2018a).

The planet was modelled as a non-accreting sink particle with a softened gravitational potential, following a procedure similar to that in Szulágyi et al. (2016). This was done to minimise the fast migration and large mass growth that an accreting particle would experience due to the large number of SPH particles. We performed simulations with varying planet masses of 2, 3, 5 and $7 M_J$, although we will only discuss the $2 M_J$ model here.

Radiation transfer was then performed on the SPH models using MCFOST (Pinte et al., 2006, 2009) following a similar method to that outlined in Section 5.1.3. Refer to Verrios et al. (2022) for further detail.

5.2.3 Tracing the wake

A key prediction of the embedded planet hypothesis is that the one-armed planet wake excited by the planet should create velocity kinks any time it intersects a velocity channel. In Calcino et al. (2022), we found that this may be used to trace the planet wake shape through kinematic observations. The presence of a coherent planet wake in the observations would provide evidence for the embedded planet model over gravitational instability. We also found that the wake is best traced in the peak velocity map.

We therefore use spectrally collapsed both the MAPS ^{12}CO observations (Öberg et al., 2021) and the synthetic observations from our SPH + radiation transfer model to create peak velocity maps. Unlike the peak velocity maps from Section 5.1, we did not use a higher order method. Instead, we just used the standard method (e.g. The CASA Team et al., 2022) of taking the velocity of the channel each pixel is brightest in, giving a discretised map. These are plotted in Figure 5.3, with the data shown in the left panel, and the model in the right. We additionally calculated the expected wake shape using Equation (4.7) (Ogilvie and Lubow, 2002; Rafikov, 2002a), and projected it to the emission surface determined by Law et al. (2021b) following the method of Calcino et al. (2022). This is shown in both panels (grey dashed line). The velocity perturbations, which manifest as distorted contours, are seen to trace the planet wake shape through the outer disk in both the model and the observations. They are particularly obvious in the second passage of the outer wake in the north side of

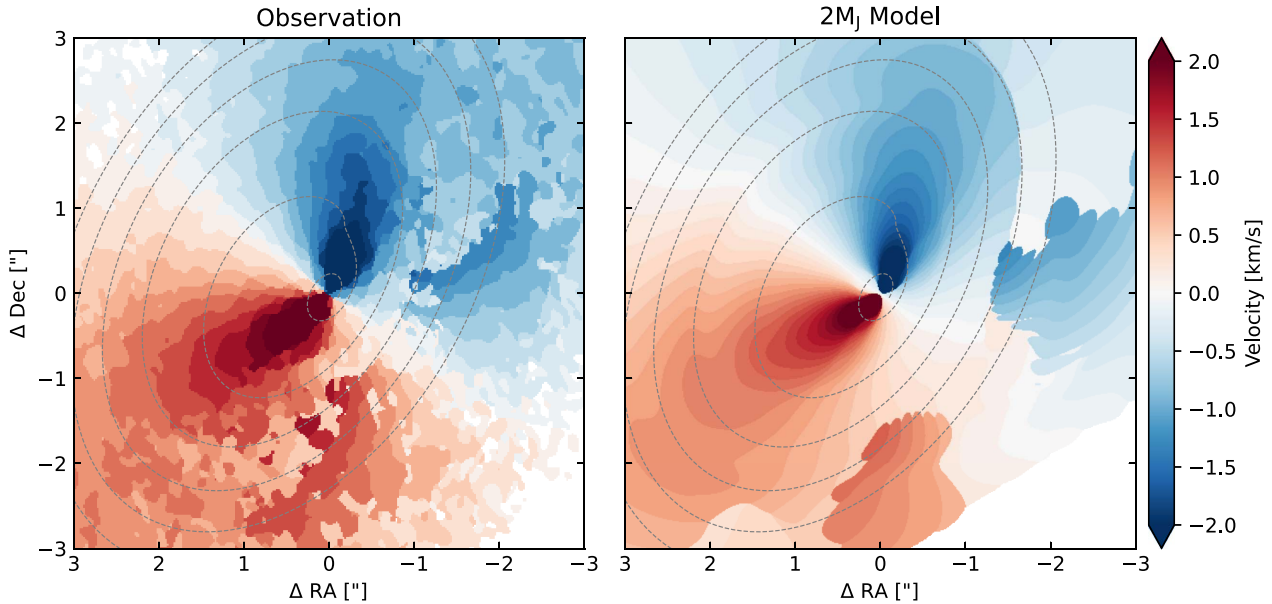


Figure 5.3: The left panel shows the peak velocity map of the ^{12}CO line emission data from MAPS (Öberg et al., 2021). The right panel shows the analogous synthetic map produced with our 2 M_J model. The dotted line in both panels shows the expected location of the planet wake as predicted by linear theory (Ogilvie and Lubow, 2002), projected to the top emitting surface of the disk (Pinte et al., 2018a; Law et al., 2021a).

the disk. In addition, the “N-wave” structure predicted by the semi-analytic models (Goodman and Rafikov 2001; Rafikov 2002a; B21) can be seen in the observations in the same region.

We therefore confirm that the wake from the planet is visible in the peak velocity map of the ^{12}CO observations, as predicted by the embedded planet model.

6

Quantitative Measurements of the Wake

This final section is concerned with trying to constrain the mass of protoplanets embedded in disks by quantitatively extracting the planet wake from kinematic observations. We will build on the work presented in [Calcino et al. \(2022\)](#), where we showed that one can trace the shape of the planet wake, and amplitude of velocity kinks, through the peak velocity map. In Section 6.1 we attempt to create a planet mass fitting procedure using synthetic peak velocity maps generated by projecting WAKEFLOW models to the emitting surface of the disk. Additionally, in Section 6.2, we present a method for locating the wake such as that in [Calcino et al. \(2022\)](#), but that does not rely on identifying patterns by eye.

6.1 Peak velocity fitting

As shown in [Calcino et al. \(2022\)](#), the planet wake manifests in the peak velocity (v_0) map generated from molecular line emission observations as spatially correlated deviations from the expected smooth iso-velocity contour. We additionally created synthetic v_0 maps by projecting semi-analytic models of the planet wake plus background rotation (Equation 2.21) to a the emitting layer, and then calculating the line-of-sight velocities. Here, we will take the same approach to generating v_0 maps, but we will fit them onto the observed peak velocities. The advantage of fitting in this way, instead of first subtracting a best-fitting model for the background rotation and fitting to the residuals, is two-fold. First, creating residuals in this way is known to easily confuse the sign of the perturbations due to the high sensitivity to the background model (see the Appendix of [Calcino et al. 2022](#)). Secondly, fitting simultaneously for the background instead of assuming it allows for the determination of the covariances in the uncertainties between the background and planet perturbation models. The best-fitting parameters for the planet mass and location will therefore not be conditioned on some background model, and we will be able to see any potential degeneracies between the parameters of each model.

6.1.1 Models

To generate our models, we first calculate the height of the emitting layer in the disk using the parameterisation ([Pinte et al., 2018a](#))

$$z(r) = z_0 \left(\frac{r}{r_{\text{ref}}} \right)^\phi \exp \left(- \left[\frac{r}{r_{\text{taper}}} \right]^\psi \right), \quad (6.1)$$

which gives a flared structure with an exponential taper. z_0 , ϕ , r_{taper} and ψ are then all model parameters that determine the height of the emitting layer. r_{ref} simply determines the radius at which the reference height z_0 and other parameters are defined, and we just set it to 100 au. While this is

a lot of freedom, the idea is to eventually use other methods of determining the height in this form such as the code DYNAMITE¹⁷ (Pinte et al., 2018a) to determine best-fitting parameters, and then to place strong priors on the same parameters when fitting for the planet mass.

We then calculate the background velocity $v_{\phi,0}$ for the disk at this emitting layer on a 300×300 Cartesian grid using

$$v_{\phi,0}(r, z) = \sqrt{\frac{GM_{\star}}{r}} \left[- (p + 2q) \left(\frac{H}{r} \right)^2 + (1 - 2q) + \frac{2qr}{\sqrt{r^2 + z^2}} \right]^{1/2}, \quad (6.2)$$

which is just Equation (4.5) rewritten as a velocity. p and q determine the amount of pressure support in the disk, where $\rho \propto r^{-p}$ and $c \propto r^{-q}$ as usual. M_{\star} is the mass of the central star. The scale height H is calculated using

$$H(r) = H_{\text{ref}} \left(\frac{r}{r_{\text{ref}}} \right)^{\frac{3}{2}-q}, \quad (6.3)$$

which comes from Equation (2.19). Thus q , p , H_{ref} and M_{\star} are model parameters that determine the background rotation of the disk.

Next, the planet perturbations are calculated by calling WAKEFLOW using the aforementioned parameters, as well as the planet mass M_p and orbital radius r_p . The calculated azimuthal velocity perturbations $v_{\phi,p}$ and radial velocity perturbations $v_{r,p}$ are then used with the background rotation $v_{\phi,0}$ to calculate the total velocity components v_r and v_{ϕ}

$$v_r = v_{r,p}, \quad v_{\phi} = v_{\phi,0} + v_{\phi,p}. \quad (6.4)$$

These are then mapped to Cartesian components v_x and v_y so that we may use rotation matrices to obtain the line-of-sight velocities

$$v_x = -v_{\phi} \sin \phi + v_r \cos \phi, \quad (6.5)$$

$$v_y = +v_{\phi} \cos \phi + v_r \sin \phi. \quad (6.6)$$

Defining the velocity field in the frame of the disk $\mathbf{v} = (v_x, v_y, v_z)$ where we set $v_z = 0$, we find that the velocity field projected to the sky plane $\mathbf{v}' = (v'_x, v'_y, v'_z)$ is given by

$$\mathbf{v}' = R_z(p)R_x(i)R_z(\phi_p)\mathbf{v} \quad (6.7)$$

where R_x and R_z are the standard Cartesian rotation matrices around the x and z axis respectively, p is the position angle of the disk on the sky, i is the inclination of the disk, and ϕ_p is the azimuthal position of the disk as measured in plane of the disk. The line-of-sight velocity is then simply given by the v'_z component of the above. Likewise, we can find the positions associated with the velocity field by rotating the position scalar field $\mathbf{x} = (x, y, z)$ in the same way to find $\mathbf{x}' = (x', y', z')$. The sky coordinates ΔRA and ΔDec in arcseconds for our projected line-of-sight velocity field is then simply

$$(\Delta \text{RA}, \Delta \text{Dec}) = \frac{1}{D}(x', y'), \quad (6.8)$$

where D is the distance to the source in parsecs.

Figure 6.1 shows an example peak velocity map generated using this method for the disk of HD 163296, using the parameters from Calcino et al. (2022) but with a planet mass of $1 M_J$.

6.1.2 Fitting procedure

Peak velocity maps produced from real kinematic observations are discretised in velocity at a resolution equal to the spacing of the channels¹⁸. We therefore discretise the velocity field from our models using

¹⁷<https://github.com/cpinte/dynamite>

¹⁸Unless using the higher order quadratic method mentioned in Section 5.1.2. Here we choose to use the usual peak velocity so that our uncertainties are related only to the beam size of the observations, and thus the positions of the iso-velocity contours. Using the quadratic method introduces statistical uncertainties in the velocities themselves.

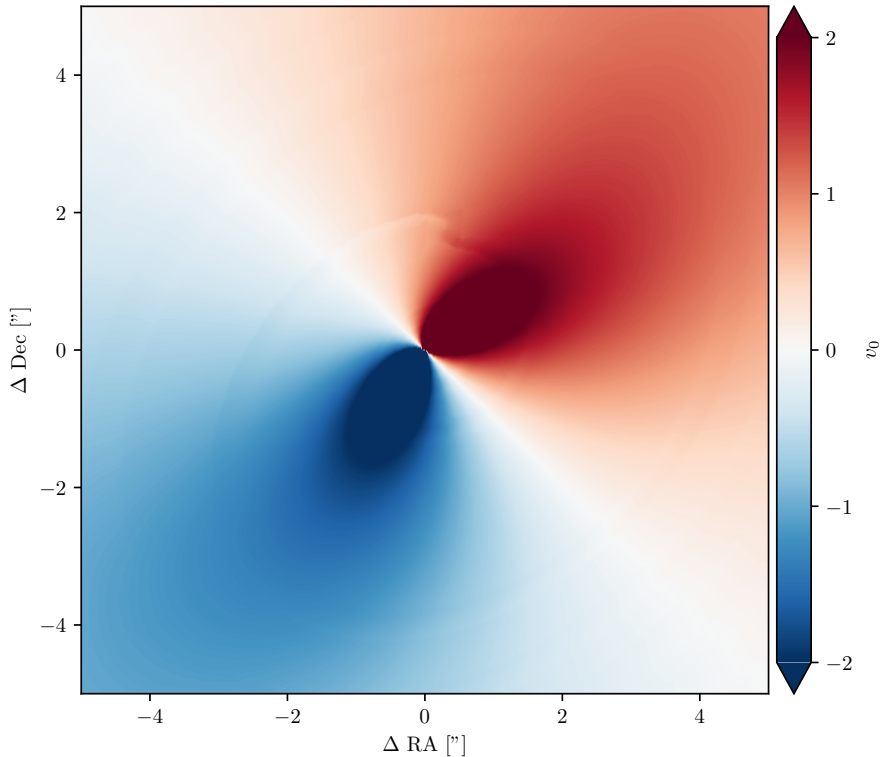


Figure 6.1: Synthetic peak velocity map generated by projecting a semi-analytic model to the emitting layer. Parameters used in the model taken from [Calcino et al. \(2022\)](#), except for the planet mass which was set to $1 M_J$. The planet wake is visible in the map due to the velocity perturbations it causes. The wake is most visible near the semi-major axis as expected for radial-dominated motion ([Rafikov, 2002a](#); [Bollati et al., 2021](#); [Calcino et al., 2022](#)).

the channel spacing. Since the planet induces wiggles in the iso-velocity curves, we performed the fitting by minimising the distance between corresponding curves from the model and observations. In a peak velocity map, we can find these curves by making a contour plot. We therefore extracted the iso-velocity curves from both the observations and models by creating a contour plot with the PYTHON package MATPLOTLIB, which calculates the points along the contours using a marching squares algorithm ([Hunter, 2007](#)). Since peak velocity maps calculated from observations tend to be noisy, and often suffer from contamination by the lower surface of the disk, the calculated contours may be discontinuous towards the edge of the disk. We therefore take only the longest continuous contour returned as representative of the iso-velocity curve for a specific velocity, and discard the others. This can be seen in the left panel of Figure 6.2, which shows the peak velocity map from MAPS ^{12}CO observations ([Öberg et al., 2021](#)) that we used in [Calcino et al. \(2022\)](#). In the top left of the panel, we can see many small blobs due to backside contamination. The grey lines show the contours that we extract, and the blobs are ignored. The middle panel of Figure 6.2 shows the equivalent iso-velocity curves extracted from our example model in the previous section, this time without an embedded planet. The right panel overlays the extracted model contours with the peak velocity map from the left panel.

In order to perform the fitting, we need some notion of distance between the lines of iso-velocity in the model and observations. To do this, we summed the Euclidean distance between nearest points along each contour. That is, for each point $(x_{o,j}, y_{m,j})$ along for example the $\Delta v = 200 \text{ m/s}$ iso-velocity curve in the observations, we found the closest point $(x_{m,j}, y_{m,j})$ on the $\Delta v = -200 \text{ m/s}$ iso-velocity curve in the model, and calculated the distance $d_j^2 = (x_{o,j} - x_{m,j})^2 + (y_{o,j} - y_{m,j})^2$. Summing these distances then yields the total “distance” between the two curves $D = \sum_j d_j$. This distance was calculated for all of the pairs of iso-velocity curves extracted. The uncertainty in this distance is σ_{beam} , which is the angular size of the telescope resolution. We therefore chose our reduced chi

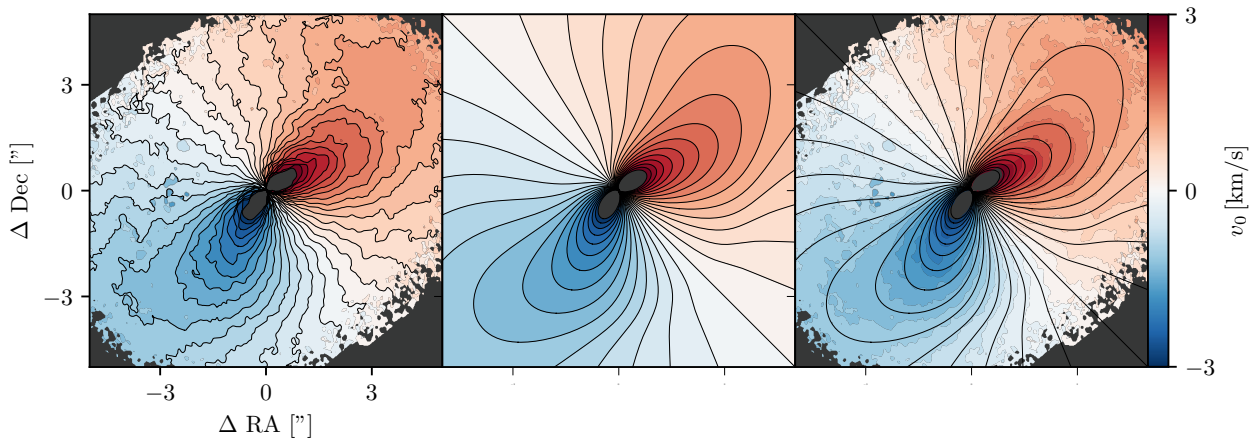


Figure 6.2: The left panel shows a plot of the peak velocity map calculated from the $0.15''$ resolution ^{12}CO line emission observations of the circumstellar disk of HD 163296 (Öberg et al., 2021), with the contours extracted by our algorithm plotted in grey. The middle panel shows our model, with the extracted contours again plotted in grey. The right panel shows the contours extracted from the model plotted over the observed peak velocity.

squared to be

$$\chi^2_{\text{red}} = \left(\sum_i^{N_C} N_i - N_p \right)^{-1} \left(\sum_i^{N_C} \sum_j^{N_i} \frac{(x_{o,ij} - x_{m,ij})^2 + (y_{o,ij} - y_{m,ij})^2}{\sigma_{\text{beam}}^2} \right), \quad (6.9)$$

where the i index sums over each iso-velocity contour of a particular line-of-sight velocity, and the j index sums over all the points along that contour. N_i is therefore the number of points along observed contour i , while N_C is the total number of contours. N_p is the number of parameters in the model.

6.1.3 Background fitting

Before attempting to fit for planet mass, we wanted to confirm that we could obtain χ^2 minima in parameter space for sensible values of a model including only the unperturbed background disk. To do this we used the JvM corrected (Jorsater and van Moorsel, 1995) $^{12}\text{CO } J = 2 - 1$ $robust=0.5$ line emission observations of HD 163296 from the MAPS large program (2018.1.01055.L, Öberg et al. 2021; Czekala et al. 2021)¹⁹, which has a channel spacing of 200m/s, and a beam size of $0.15''$. This is the same data we used in Calcino et al. (2022). We also assumed a systemic velocity of $v_{\text{los}} = 5.76$ km/s (Teague et al., 2021) and a distance of 101.5 pc (Gaia Collaboration et al., 2018).

We then adopted the best-fitting background model parameters used in (Calcino et al., 2022), and varied only parameter one at a time to see whether each found a minimum χ^2 value. The results are shown in Figure 6.3. The top row of the figure shows the parameters that determine the background rotation. We see that for the rotation parameters, both M_\star and H_{ref}/r find minima around approximately $1.8 M_\star$ and 0.11 respectively. These are both compatible with the values from Pinte et al. (2018b), differing by less than 5% in each case. However the p and q indices are both constrained very poorly and neither find a minimum. This is perhaps not surprising when considering that changing either of this has little effect on our model, as they merely change the background rotation very slightly as part of the pressure gradient term. The aspect ratio H/r is also only responsible for the pressure correction, but since it is squared in Equation (6.2) it has a larger effect. It therefore seems unlikely that p , q and H/r could be disentangled from fitting purely our background model. However, both H/r and q are both responsible for determining the shape of the wake once we add a planet (see Equation 4.7), which may allow us to constrain them more effectively.

Turning our attention to the parameters that determine the emission surface, shown in the bottom row of Figure 6.3, we see that all the parameters found a minimum. These minima occur at values

¹⁹The data publicly available at <http://alma-maps.info/>.

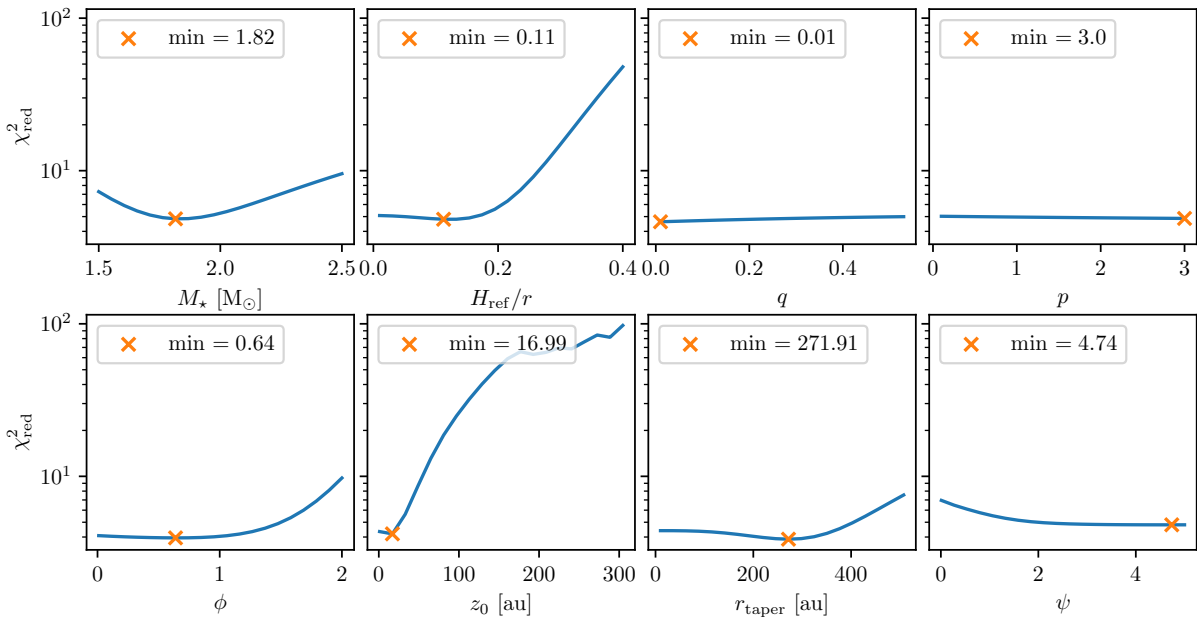


Figure 6.3: χ^2_{red} values fitting an unperturbed disk model to the MAPS ^{12}CO peak velocity map of the HD 163296 disk, calculated by varying each parameter one at a time while keeping the others fixed. The top row is parameters that determine the disk rotation, while the bottom row parameters determine the ^{12}CO emission surface. The parameter values for the best-fit are marked by orange crosses. We see that the parameters that determine the pressure support p and q , as well as the disk taper rate ψ , are poorly constrained.

of $\phi = 0.64$, $z_0 = 16.99$ au, $r_{\text{taper}} = 271.91$ au, and $\psi = 4.74$. Comparing with the values found by Law et al. (2021b), which were $\phi = 1.851$, $z_0 = 39.37$ au, $r_{\text{taper}} = 239.74$ au, and $\psi = 1.182$, we see that ϕ , z_0 and ψ are significantly different. The difference in ψ is not too surprising, as the rate of exponential taper of the height of the disk likely does not effect the model very much. This is because the taper only starts to have an sizeable effect at around 300 au or $\sim 3''$, which is near the edge of the data. The cause of the difference in values we obtained for ϕ and z_0 is less clear. They imply that the inner disk stays flatter for longer than found by Law et al. (2021b), before rising more steeply in the outer disk. This may be due to our method of calculating χ^2 , which relies on Euclidean distances. Changing the height in the inner disk does not result in much change to the iso-velocity contours, and so measuring the height in the inner disk in this way perhaps provides a poor constraint. The results do seem to recover the height in the outer disk more accurately, since r_{taper} is relatively close to the Law et al. (2021b) value. Of course, all this comes with the important caveat that each minimum is conditioned on the other parameters being correct, since we are varying them one at a time here.

6.1.4 Planet fitting

Next, we performed the same analysis as above, except including the perturbations induced by a planet. We used a $2.0 M_J$ planet, placed at an orbital radius of 256 au and a planet azimuth of 55 degrees (Pinte et al., 2018b; Calcino et al., 2022). The results for the background parameters are presented in Figure 6.4, while the results for the planet parameters are shown in Figure 6.5.

For the background parameters shown in the top row, all of the minima are different to those found in Figure 6.3, where a planet was not included. The central star mass has increased by $\sim 10\%$, H_{ref}/r has halved, and p and q show different behaviours. There are multiple possible explanations for this. The first, and more straightforward, is that the kinks we have added to the model contours by including a planet allows for a better fit to background features. Alternatively, it may be due to the effect those parameters have on the planet perturbations. For example, reducing H_{ref}/r will significantly reduce the value of the thermal mass (see Equation 3.130). This in turn increases the value of M_p/M_{th} , resulting in larger kink amplitudes. H_{ref}/r and q both determine the shape of the

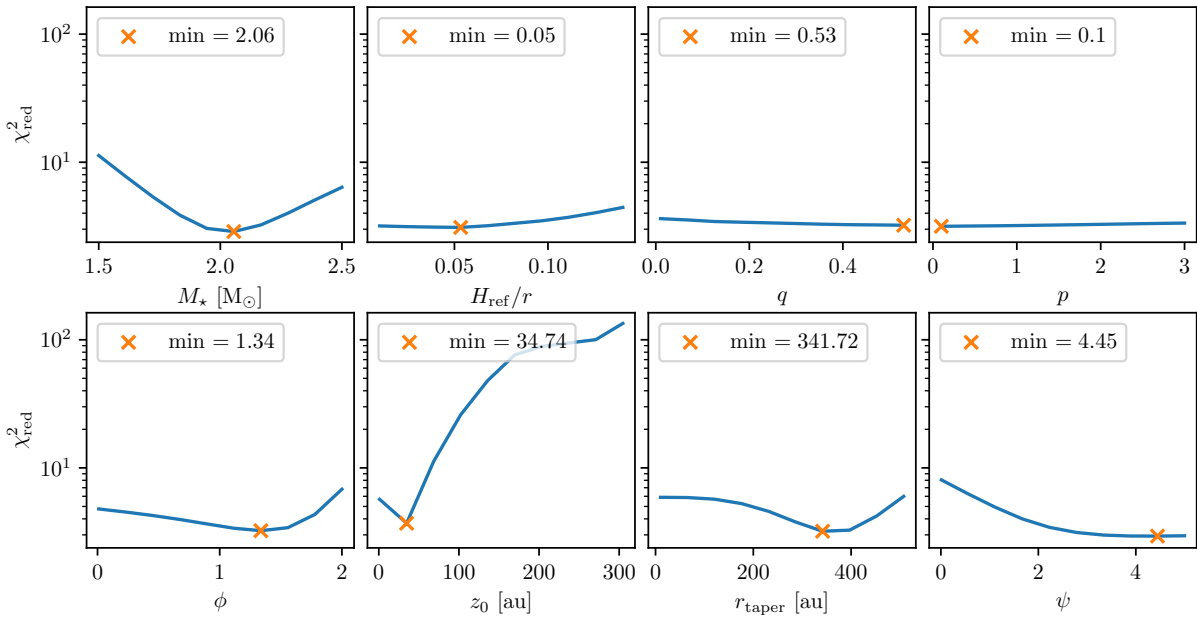


Figure 6.4: χ^2_{red} values fitting an disk model with a $2 M_J$ perturbing planet to the MAPS ^{12}CO peak velocity map of the HD 163296 disk, calculated by varying each parameter one at a time while keeping the others fixed. The top row is parameters that determine the disk rotation, while the bottom row parameters determine the ^{12}CO emission surface. The parameter values for the best-fit are marked by orange crosses. The introduction of a planet results in different local minima for the background disk parameters.

wake (see Equation 4.7), which is likely to change how well the kinks fit the data.

For the emission surface parameters (bottom row of Figure 6.4), we again find differences to the purely background fit. ϕ and z_0 are both larger, which in each case increases the height of the emitting layer²⁰. The radius of the taper is $\sim 25\%$ larger, which has the result of increasing the height of the disk model in the region around 300 au. The result for ψ is not much different, with a similar behaviour to in the background case where any large value of ψ performs well. These differences in height corroborate the idea that adding the planet kinks can result in a different best-fit for just the background as already mentioned. These parameters do not have any effect of the shape of the wake or the amplitude of the kinks, unlike the parameters that determine the rotation.

Figure 6.5 shows the results for the planet parameters themselves. Looking first at the planet mass, we see that the best-fitting value is the largest in the interval that we tried, $12.5 M_J$. We did not allow for planets larger than this as the semi-analytic solution becomes very inaccurate and poorly behaved (see Section 4.3.4). This result is surprising, as it has previously been found that a planet of mass $3 - 4 M_J$ accurately recreates the velocity kink induced nearby the planet. Additionally, r_p actually finds two minima, one at around 240 au, which is close to what we would expect from Calcino et al. (2022). The other minimum at 215 au is intriguing, as there have been claims of an additional planet closer to the star (Teague et al., 2018; Pinte et al., 2020). It may be that this minimum results from the wake attempting to fit the arc feature mentioned in Teague et al. (2021) and Calcino et al. (2022) (see the opaque crosses in Figure 1 of the latter). Finally, ϕ_p finds a minimum at ~ 100 degrees, which is significantly different to the $\phi_p = 55$ degrees that we used in Calcino et al. (2022). Since tightly-wound spiral structure varies rapidly in ϕ as the radius changes slowly, it may be that this is because the value of $r_p = 256$ au we have chosen is not quite correct.

²⁰More precisely, increasing ϕ makes the emitting layer more flared, whereas increases z_0 scales the height by a constant for all r .

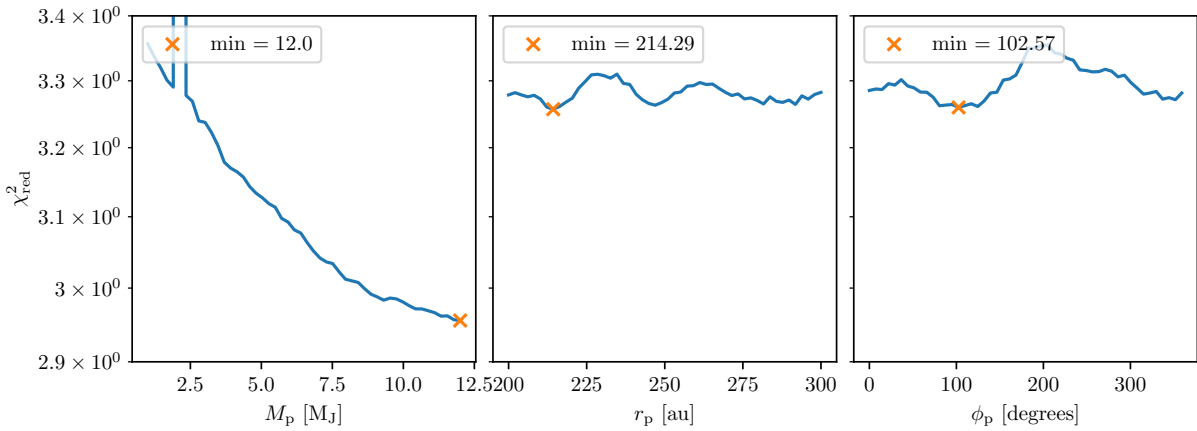


Figure 6.5: χ^2_{red} values fitting an disk model with a $2 M_J$ perturbing planet to the MAPS ^{12}CO peak velocity map of the HD 163296 disk, calculated by varying each parameter one at a time while keeping the others fixed. The left panel shows the result of varying the planet mass, while the middle and right panels show the results for varying r_p and ϕ_p respectively. The parameter values for the best-fit are marked by orange crosses.

6.1.5 Model-model fitting

It is not exactly clear how to interpret the results presented in the previous section. While minima were found for most of the background disk parameters, q and p were both very poorly constrained. Furthermore, the best-fitting parameters changed significantly once a planet was added. Most importantly, we did not find a minimum at a particular planet mass, instead the performance just increased with M_p . This is of particular concern since this is the value we are most interested in constraining.

In order to understand this results better, we generated a synthetic observation using our models, and then performed a grid search in χ^2_{red} . For the synthetic observation, we set the distance, inclination and position angle to 100 pc, -225 degrees, and 45 degrees. We then chose background model parameters of $M_\star = 2.0 M_\odot$, $H_{\text{ref}}/r = 0.1$, $q = 0.35$, $p = 2.25$, $\phi = 1.5$, $\psi = 3.5$, $z_0 = 30$ au and $r_{\text{taper}} = 400$ au. The planet parameters were chosen to be $r_p = 300$ au, $M_p = 0.8 M_J$, and $\phi_p = 45$. All of the parameters are similar to those found by [Pinte et al. \(2018b\)](#) and [Calcino et al. \(2022\)](#) for HD 163295, except that we deliberately chose a low mass planet to rule out any strange effects from the high-mass regime in the semi-analytic model.

We then performed a grid search in M_p and ϕ_p , where all other parameters were set to their true values. We used 20 evenly spaced M_p values in the range $0.5 - 1.5 M_J$, and 20 evenly spaced ϕ_p values in the range $0 - 90$ degrees. For σ_{beam} , we simply kept the value of $0.15''$ from the observations, since it is merely a constant scale factor. The result is shown in Figure 6.6, where the heatmap shows the resultant χ^2_{red} value for each set of M_p and ϕ_p values, while the true values are marked by a red dot. We see that once again the best-fit is provided by the largest M_p , as well as $\phi_p = 0^\circ$. This was surprising as the minimum in χ^2_{red} therefore occurs nowhere near the true values, even for the case where we have every other parameter exactly correct.

6.1.6 Discussion

The results obtained in Section 6.1.5 indicate that our choice of χ^2_{red} is not well suited to the problem, as it does not find a minimum at the true value even in the case that the model matches the data exactly. It is likely that this comes down to how the distance between the individual points are calculated. Say for example we are finding the distance between contours A and B . For some point along A we find the nearest point on B and calculate the distance. This is done iteratively until every point on A has a distance, and then these distances are summed. This works well for the case where our contours vary smoothly, that is there are no planet perturbations. However adding the planet essentially adds “wiggles” in the contour, and adding a larger planet adds larger wiggles. This means that when points along A are looking for the nearest point on B , they just are more likely to find a

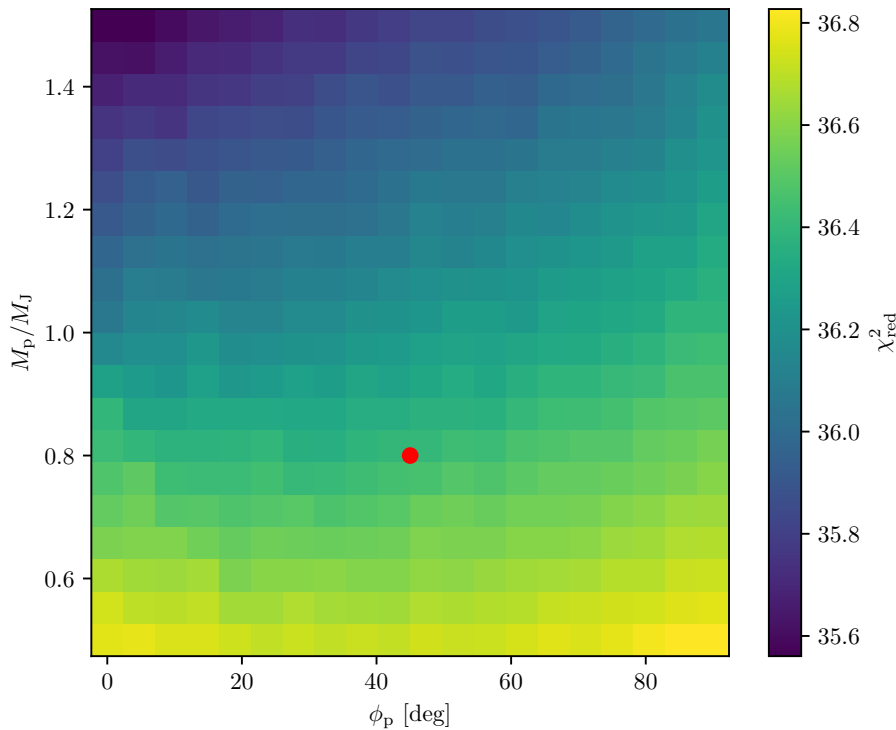


Figure 6.6: Grid search in χ^2_{red} fitting synthetic observations generated with our model. M_p and ϕ_p were both varied around their true values, while all other parameters were set exactly to the values used to generate the synthetic observations. We see that the minimum in χ^2_{red} once again occurs for the highest mass planet provided, and is not centred on the true values shown by the red dot.

close point. Thus providing larger mass planets results in a lower χ^2_{red} .

This problem could be solved by getting rid of the nearest point search, and instead using some other notion of the distance between the contours. For example, the radial distance could be used, or the azimuthal distance. The problem with either of these approaches is that the iso-velocity contours have a butterfly shape, where they go from a fixed azimuthal and varying radius, to a fixed radius but varying azimuth. A different idea would be to project a line perpendicularly from contour A and find the distance needed to intersect contour B. This would work fine in the case of the unperturbed background disk, but adding the planet would result in rays projecting in strange directions due to the N-wave shape of the induced kinks (Goodman and Rafikov, 2001; Bollati et al., 2021). These reasons highlight why we chose the nearest-neighbour search in the first place, and it is not clear how to modify the procedure to do better.

This problem could be avoided completely if we did not have to simultaneously deal with the background disk and the perturbations, since in essence the problem is that the perturbations are being fit to the background. As already discussed, subtracting a model to remove the background has numerous issues that would prevent the fitting of semi-analytic models. It would therefore be valuable to extract the perturbations in a way that is model-independent. This would still provide results that are not conditioned on assuming some model. In the following section we present preliminary results from a method developed to do this.

We also found that the minimum in ϕ_p did not seem to correspond to the true value. This is harder to explain, although close inspection of Figure 6.6 shows that actually the minimum in ϕ_p is approximately centred on the true value if we consider only the row of results with $M_p = 0.8 M_J$ (which is the true planet mass value). The best-fit ϕ_p then seems to decrease as M_p increases. It is possible that this is due to the relative invariance of spiral shape to rotation, since the radial locations change slowly as the azimuth varies.

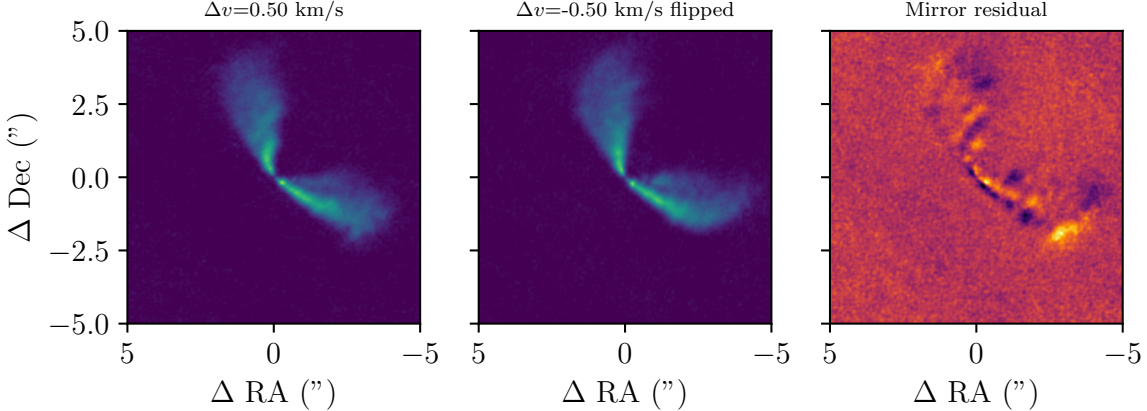


Figure 6.7: The left panel shows the $\Delta v = 0.5$ km/s velocity channel taken from the $0.15''$ resolution MAPS observations of HD 163296. The middle panel shows the corresponding $\Delta v = -0.5$ km/s interpolated from the cube. The right panel shows the residuals calculated by subtracting the middle image from the left image. We see that the bottom right velocity kink from [Calcino et al. \(2022\)](#) shows up in the residuals as a bright blob.

6.2 Mirror Residuals

Another aspect of [Calcino et al. \(2022\)](#) that we would like to build on is the detection of the wake itself. The method we presented there, of mapping the wake through the peak velocity plot through spatially correlated deviations in nearby iso-velocity contours, relies on a by eye inspection and so is subject to human bias. By exploiting the symmetry of channel maps, we can instead extract asymmetries in the disk systematically, and produce an “image” of the planet wake.

Once the systemic velocity has been subtracted, velocity channel maps have both negative and positive velocity channels, with some spacing in velocity Δv . For a perfectly axisymmetric disk, the corresponding curves of iso-velocity on each side of the disk should be symmetric around the semi-major axis. This can be seen in the middle panel of Figure 6.2, where the blue and red sides of the disk are just the reflection of each other. Therefore, the velocity channel $v = -200$ m/s for example, should look the same as the channel $v = +200$ m/s after an appropriate rotation, if the disk were perfectly axisymmetric. By associating channels with their symmetric partner, one can then calculate residuals than show the asymmetries between each side of the disk.

In reality, the systemic channel of the cube is unlikely to have a velocity of zero, and so the velocity of the negative channels will not line up exactly with those from the positive channels. To remedy this, we simply linearly interpolated the cube in the velocity direction (that is, we interpolated along the line-profile of each pixel), to obtain interpolated channels such that they could be paired up exactly. We performed this analysis again on the MAPS ^{12}CO data of HD 163296 ([Öberg et al., 2021](#)). The left panel shows the $v = 0.5$ km/s channel, while the middle panel shows the corresponding $v = -0.5$ km/s channel that has been interpolated from the negative velocity channels. The right panel shows the residuals calculated after subtracting one channel from the other. This process yields a cube of “mirror residuals”.

Collapsing this cube along the velocity axis by taking for each pixel its value in the channel where it is brightest, the so-called peak intensity map or moment-8, yields a map of asymmetries in the disk. This is shown in Figure 6.8. Two large bright arcs can be seen in the figure. The bottom-most arc can be identified as the wake from the planet, which we demonstrate by plotting the wake shape projected to the emitting layer as in [Calcino et al. \(2022\)](#). The other large bright arc does not seem to be associated with the planet wake, and has been previously identified by [Teague et al. \(2021\)](#) and [Calcino et al. \(2022\)](#).

Extracting the perturbations associated with the wake in this way is valuable because unlike other methods ([Teague et al., 2021, 2022](#)) it is completely model-independent. It does however come with

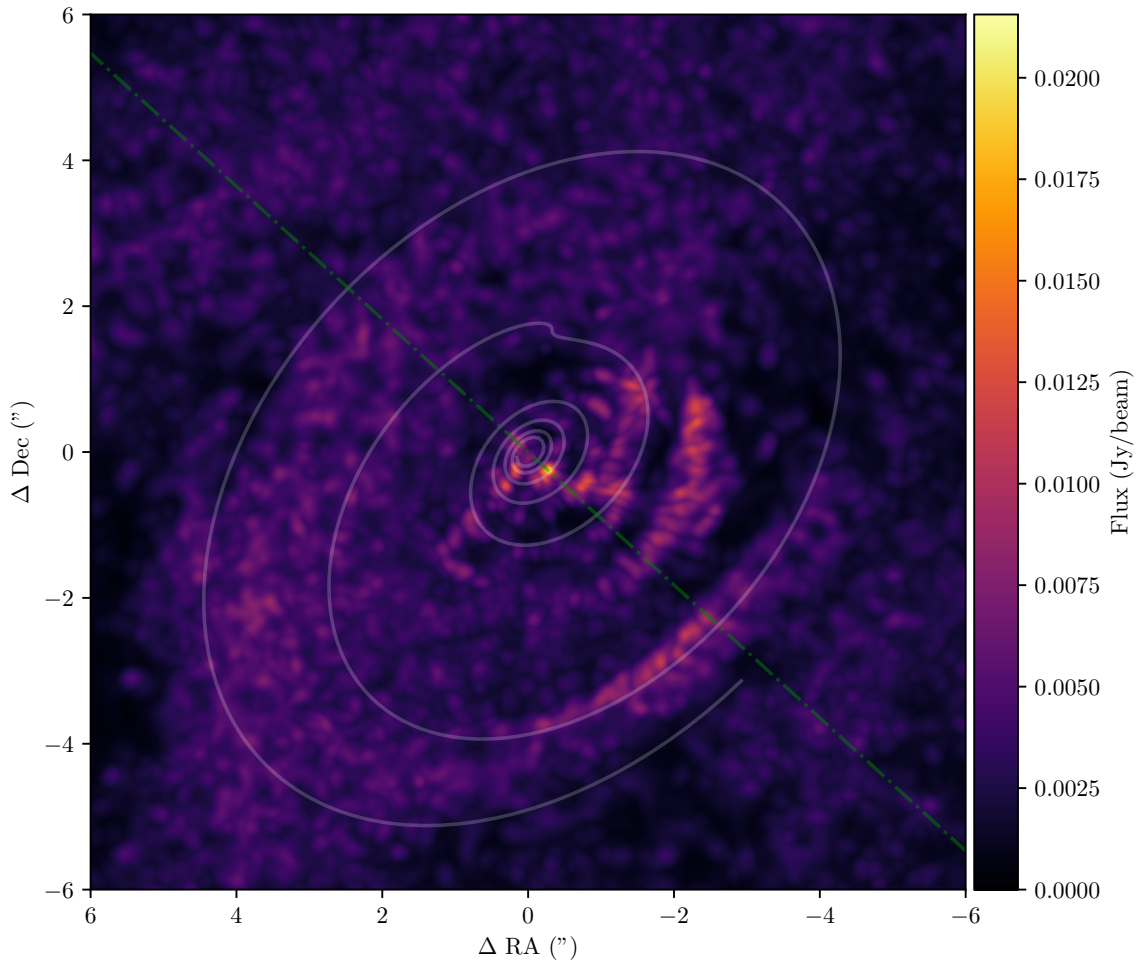


Figure 6.8: Peak intensity plot, generated from the mirror residuals of the MAPS ^{12}CO kinematic observations of HD 163296 ([Öberg et al., 2021](#)). Plotted also is the shape of the planet wake projected to the emitting layer from [Calcino et al. \(2022\)](#). We clearly see the planet wake as a bright arc in the bottom right of the image. Also identified is a further bright arc not associated with the planet wake, which has also been pointed out by [Teague et al. \(2021\)](#) and [Calcino et al. \(2022\)](#). The green dot-dashed line shows the line of symmetry for the plot, since each half of the disk has been used to subtract the other half, it is ambiguous which side of the green line each feature in the map should actually be on.

some important caveats, the first of which is a positional ambiguity in the features identified in the map shown in Figure 6.8. Since the residuals on each half of the disk are found by subtracting the other half, features that show up as positive residuals on one side of the disk will also show up as negative residuals on the other side. One could obtain the symmetric partner of Figure 6.8 by taking instead the lowest intensity value in each channel from the mirror residuals cube.

Finally, it is not clear how this method may be used to extract velocity information, which is ultimately what we need to determine the planet mass. We found that attempting to create a peak velocity map from the mirror residuals cube resulted in essentially just noise, and concluded that it is not very useful. This is probably not surprising since the velocity of the channel where a particular pixel is brightest is not very meaningful for a pixel where there are no asymmetric features.

7

Conclusion

The detection and measurement of protoplanets still embedded in the circumstellar disks they formed from is a vital step in constraining models of planet formation. A promising method for making such measurements is through identifying kinematics features from perturbing planets in observations of molecular line emission in disks. In this thesis we have built upon semi-analytic methods for modelling the interaction between the planet and the gas disk, and applied these methods to observations to constrain potential planets.

In Chapters 2 and 3 we reviewed the relevant physics of both protoplanetary disk structure and planet-disk interactions. We derived the linear disk response to a small perturbation using WKB methods, and found the Lindblad resonance locations where a tidally-forcing body excited density waves. Combining these findings we then used phase arguments to derive the shape of the coherent, one-armed wake that is formed from constructive interference of individual modes. We then reviewed the work of Goodman and Rafikov (2001); Rafikov (2002a) in developing a semi-analytic framework to calculate the density perturbations along the planet wake, in both the linear and non-linear regimes. Lastly, we applied this framework to determine the quantities that we must constrain observationally in order to measure planet masses.

In Chapter 4 we presented our Python package WAKEFLOW for generating semi-analytic models of planet wakes in protoplanetary disks. The package contains both accuracy and efficiency improvements over previous methods. The accuracy improvements include a more accurate treatment of the initial conditions used in the non-linear wake evolution, improved matching between the linear and non-linear solutions, and a high-order method for extracting the velocity perturbations.

In Chapter 5 we presented two applications of the models to the detection of protoplanets, in the disks of HD 169142 and IM Lupi. We found that the kinematic arc identified in HD 169142 is not well explained by the predominantly radial motions in the planet wake. In IM Lupi, we found that a spiral structure could be traced through the peak velocity map, providing evidence of an embedded planet.

Finally, in Chapter 6 we presented preliminary work on the development of a fitting procedure to determine planet masses from kinematic observations. To do this, we fit iso-velocity contours generated by semi-analytic models to the observed peak velocity map. We found that this performed reasonably well for fitting just an unperturbed disk, but failed once a planet was added due to complications with how the distances between the curves in the model and observations were calculated. We then presented a model-independent way of extracting the perturbations present in the kinematics, although it remains unclear how to leverage this to perform fitting of the planet mass. However, this method does allow for quantitative identification of asymmetric features in the disk such as planet wakes, without needing to assume a background model.

7.1 Future Work

Further improvements to the semi-analytic models are likely needed before they can be treated seriously in the high-mass regime of more than a few thermal masses. There are three main issues that need to be addressed in the case of large planet masses:

1. The spatial discontinuity over the edge of the linear box, which becomes worse for increasingly more massive planets (see Section 4.3.4). This effect is not physical, and so limits the application of the results from the models nearby the planets. The exact cause of the discontinuity should be investigated, so that it may be minimised if possible.
2. The shape of the wake diverges from that predicted by purely linear theory ([Ogilvie and Lubow, 2002](#)). [Cimerman and Rafikov \(2021\)](#) introduced a correction term to account for this, and it should be possible to incorporate this into the solution.
3. Large planets open a gap in the gas density profile centred on the planet orbital radius (e.g. [Ward, 1997](#)). This effect is currently not captured in the analytic models but is important for two reasons. Firstly, the resulting pressure gradient at the edge of the gaps results in a change to the azimuthal velocities in the disk ([Teague et al., 2018](#)). Secondly, the t coordinate that determines the rate of evolution along the wake depends on the surface density profile, and so a gap may effect the t coordinate where the shock forms. The planet gap could be added using the analytic prescription from [Kanagawa et al. \(2015a\)](#), and the effects of the pressure gradient included in the resultant velocities.

Additional work also needs to be done for the planet mass fitting. We found that the method attempted here, of fitting a model including both the background disk and planet perturbations projected to the emitting layer, did not produce a minimum in χ^2 at the true planet parameters. We therefore propose that further work should be done investigating model-independent methods of extracting the perturbations in the data, such as the preliminary work on mirror residuals we presented in Section 6.2.

Finally, the semi-analytic plus radiation transfer method presented in Section 5.1 could be used to perform a study on the detectability of planet wakes in kinematic observations. Since rotation curves are steeper towards the centre of a disk, velocity perturbations result in larger spatial deflections of the iso-velocity curves in the outer disk. Furthermore, since the perturbations induced by the wake are predominantly radial ([Rafikov, 2002a; Calcino et al., 2022](#)), the azimuthal location of the planet should also affect detectability. A detailed quantification of the orbital radii, azimuthal location of the planet, disk inclination, disk positive angle, and planet mass should be performed to determine the regions of parameter space which this method may be used to probe.

A

1D Isentropic Gas

Here we derive the Riemann invariants and characteristics for one dimensional isentropic gas flow, following [Landau and Lifshitz \(1987\)](#). The Euler and continuity equations are in this case

$$\partial_t P + v \partial_x P + \rho c^2 \partial_x v = 0, \quad (\text{A.1})$$

$$\partial_t v + v \partial_x v + \rho^{-1} \partial_x P = 0, \quad (\text{A.2})$$

where we have replaced the time derivative of density with that of pressure using

$$\partial_t \rho = \partial_P \rho \partial_t P = c^{-2} \partial_t P. \quad (\text{A.3})$$

Dividing Equation (A.1) by $\pm \rho c$ and adding the result to Equation (A.2) yields

$$\partial_t v \pm \frac{1}{\rho c} \partial_t P + \left(\partial_x v \pm \frac{1}{\rho c} \partial_x P \right) v \pm \left(\partial_x v \pm \frac{1}{\rho c} \partial_x P \right) c = 0, \quad (\text{A.4})$$

$$\Rightarrow \partial_t v \pm \frac{1}{\rho c} \partial_t P + \left(\partial_x v \pm \frac{1}{\rho c} \partial_x P \right) (v \pm c) = 0. \quad (\text{A.5})$$

We define two unknown functions called *Riemann Invariants* as

$$J_{\pm} = v \pm \int \frac{1}{\rho c} dP = v \pm \int \frac{c}{\rho} d\rho. \quad (\text{A.6})$$

For an isentropic flow ρ and c are always definite functions of P . If the equation of state is polytropic $P = K \rho^{\gamma}$ then $c^2 = \gamma K \rho^{\gamma-1}$ giving

$$\int \frac{c}{\rho} d\rho = \sqrt{\gamma K} \int \rho^{(\gamma-3)/2} d\rho = \frac{2c}{\gamma-1}. \quad (\text{A.7})$$

Thus the Riemann invariants in this case are simply

$$J_{\pm} = v \pm \frac{2c}{\gamma-1}. \quad (\text{A.8})$$

We can rewrite Equations (A.1) and (A.2) in terms of J_{\pm} as

$$[\partial_t + (v \pm c) \partial_x] J_{\pm} = 0. \quad (\text{A.9})$$

Now finding the total differential of J_{\pm} and substituting (A.9) gives

$$dJ_{\pm} = \partial_t J_{\pm} dt + \partial_x J_{\pm} dx \quad (\text{A.10})$$

$$= \partial_t J_{\pm} dt - \frac{1}{v \pm c} \partial_t J_{\pm} dx. \quad (\text{A.11})$$

Consider two curves C_{\pm} , defined as

$$C_{\pm} : \frac{dx}{dt} = v \pm c. \quad (\text{A.12})$$

Substituting these into our equation for the total differential of the Riemann invariants dJ_{\pm} in (A.11) gives the result that $dJ_+ = 0$ along C_+ , and $dJ_- = 0$ along C_- . Thus we see that the Riemann invariants J_+ and J_- are constant along C_+ and C_- respectively. C_{\pm} are known as *characteristics*. Additionally, the operators $\partial_t + (v \pm c)\partial_x$ are simply the differentiation operators along the characteristics.

Bibliography

- ALMA Partnership et al.: 2015, ‘The 2014 ALMA Long Baseline Campaign: First Results from High Angular Resolution Observations toward the HL Tau Region’. *The Astrophysical Journal* **808**, L3.
- Andrews, S. M.: 2020, ‘Observations of Protoplanetary Disk Structures’. *Annual Review of Astronomy and Astrophysics* **58**, 483–528.
- Andrews, S. M., J. Huang, L. M. Pérez, A. Isella, C. P. Dullemond, N. T. Kurtovic, V. V. Guzmán, J. M. Carpenter, D. J. Wilner, S. Zhang, Z. Zhu, T. Birnstiel, X.-N. Bai, M. Benisty, A. M. Hughes, K. I. Öberg, and L. Ricci: 2018a, ‘The Disk Substructures at High Angular Resolution Project (DSHARP). I. Motivation, Sample, Calibration, and Overview’. *The Astrophysical Journal* **869**, L41.
- Andrews, S. M., M. Terrell, A. Tripathi, M. Ansdell, J. P. Williams, and D. J. Wilner: 2018b, ‘Scaling Relations Associated with Millimeter Continuum Sizes in Protoplanetary Disks’. *The Astrophysical Journal* **865**, 157.
- Andrews, S. M., D. J. Wilner, C. Espaillat, A. M. Hughes, C. P. Dullemond, M. K. McClure, C. Qi, and J. M. Brown: 2011, ‘Resolved Images of Large Cavities in Protoplanetary Transition Disks’. *The Astrophysical Journal* **732**, 42.
- Andrews, S. M., D. J. Wilner, Z. Zhu, T. Birnstiel, J. M. Carpenter, L. M. Pérez, X.-N. Bai, K. I. Öberg, A. M. Hughes, A. Isella, and L. Ricci: 2016, ‘Ringed Substructure and a Gap at 1 Au in the Nearest Protoplanetary Disk’. *The Astrophysical Journal* **820**, L40.
- Ansdell, M., J. P. Williams, L. Trapman, S. E. van Terwisga, S. Facchini, C. F. Manara, N. van der Marel, A. Miotello, M. Tazzari, M. Hogerheijde, G. Guidi, L. Testi, and E. F. van Dishoeck: 2018, ‘ALMA Survey of Lupus Protoplanetary Disks. II. Gas Disk Radii’. *The Astrophysical Journal* **859**, 21.
- Ansdell, M., J. P. Williams, N. van der Marel, J. M. Carpenter, G. Guidi, M. Hogerheijde, G. S. Mathews, C. F. Manara, A. Miotello, A. Natta, I. Oliveira, M. Tazzari, L. Testi, E. F. van Dishoeck, and S. E. van Terwisga: 2016, ‘ALMA Survey of Lupus Protoplanetary Disks. I. Dust and Gas Masses’. *The Astrophysical Journal* **828**, 46.
- Armitage, P. J.: 2022, ‘Lecture Notes on Accretion Disk Physics’. *arXiv e-prints*.
- Artymowicz, P.: 1993, ‘On the Wave Excitation and a Generalized Torque Formula for Lindblad Resonances Excited by External Potential’. *The Astrophysical Journal* **419**, 155.
- Astropy Collaboration et al.: 2022. *The Astronomical Journal* **935**(2), 167.
- Avenhaus, H., S. P. Quanz, A. Garufi, S. Perez, S. Casassus, C. Pinte, G. H. M. Bertrang, C. Caceres, M. Benisty, and C. Dominik: 2018, ‘Disks around T Tauri Stars with SPHERE (DARTTS-S). I. SPHERE/IRDIS Polarimetric Imaging of Eight Prominent T Tauri Disks’. *The Astrophysical Journal* **863**, 44.
- Bae, J., R. Teague, and Z. Zhu: 2021, ‘Observational Signature of Tightly Wound Spirals Driven by Buoyancy Resonances in Protoplanetary Disks’. *The Astrophysical Journal* **912**, 56.
- Bae, J. and Z. Zhu: 2018, ‘Planet-Driven Spiral Arms in Protoplanetary Disks. I. Formation Mechanism’. *The Astrophysical Journal* **859**, 118.
- Bae, J., Z. Zhu, and L. Hartmann: 2017, ‘On the Formation of Multiple Concentric Rings and Gaps in Protoplanetary Disks’. *The Astrophysical Journal* **850**, 201.
- Ballabio, G., G. Dipierro, B. Veronesi, G. Lodato, M. Hutchison, G. Laibe, and D. J. Price: 2018, ‘Enforcing Dust Mass Conservation in 3D Simulations of Tightly Coupled Grains with the Phantom SPH Code’. *Monthly Notices of the Royal Astronomical Society* **477**(2), 2766–2771.

Bate, M. R., I. A. Bonnell, and N. M. Price: 1995, ‘Modelling Accretion in Protobinary Systems’. *Monthly Notices of the Royal Astronomical Society* **277**, 362–376.

Benisty, M., J. Bae, S. Facchini, M. Keppler, R. Teague, A. Isella, N. T. Kurtovic, L. M. Pérez, A. Sierra, S. M. Andrews, J. Carpenter, I. Czekala, C. Dominik, T. Henning, F. Menard, P. Pinilla, and A. Zurlo: 2021, ‘A Circumplanetary Disk around PDS70c’. *The Astrophysical Journal* **916**, L2.

Benisty, M., A. Juhasz, A. Boccaletti, H. Avenhaus, J. Milli, C. Thalmann, C. Dominik, P. Pinilla, E. Buenzli, A. Pohl, J.-L. Beuzit, T. Birnstiel, J. de Boer, M. Bonnefoy, G. Chauvin, V. Christiaens, A. Garufi, C. Grady, T. Henning, N. Huelamo, A. Isella, M. Langlois, F. Ménard, D. Mouillet, J. Olofsson, E. Pantin, C. Pinte, and L. Pueyo: 2015, ‘Asymmetric Features in the Protoplanetary Disk MWC 758’. *Astronomy and Astrophysics* **578**, L6.

Bertrang, G. H. M., H. Avenhaus, S. Casassus, M. Montesinos, F. Kirchschlager, S. Perez, L. Cieza, and S. Wolf: 2018, ‘HD 169142 in the Eyes of ZIMPOL/SPHERE’. *Monthly Notices of the Royal Astronomical Society* **474**, 5105–5113.

Beuzit, J. L. et al.: 2019, ‘SPHERE: The Exoplanet Imager for the Very Large Telescope’. *Astronomy & Astrophysics* **631**, A155.

Biller, B. A., J. Males, T. Rodigas, K. Morzinski, L. M. Close, A. Juhász, K. B. Follette, S. Lacour, M. Benisty, A. Sicilia-Aguilar, P. M. Hinz, A. Weinberger, T. Henning, J.-U. Pott, M. Bonnefoy, and R. Köhler: 2014, ‘An Enigmatic Point-like Feature within the HD 169142 Transitional Disk’. *The Astrophysical Journal* **792**, L22.

Binney, J. and S. Tremaine: 2008, *Galactic Dynamics: Second Edition*. Princeton: Princeton University Press, second edition.

Bollati, F.: 2020, ‘An Analytical Model for Planet Induced Velocity Perturbations in Protoplanetary Discs’. Master’s thesis, Università degli Studi di Milano.

Bollati, F., G. Lodato, D. J. Price, and C. Pinte: 2021, ‘The Theory of Kinks - I. A Semi-Analytic Model of Velocity Perturbations Due to Planet-Disc Interaction’. *Monthly Notices of the Royal Astronomical Society* **504**, 5444–5454.

Boss, A. P.: 1997, ‘Giant Planet Formation by Gravitational Instability’. *Science* **276**, 1836–1839.

Brouwer, D. and G. M. Clemence: 1961, *Methods of Celestial Mechanics*. New York: Academic Press, 1st edition.

Calahan, J. K. et al.: 2021, ‘Molecules with ALMA at Planet-forming Scales (MAPS). XVII. Determining the 2D Thermal Structure of the HD 163296 Disk’. *The Astrophysical Journal Supplement Series* **257**, 17.

Calcino, J., T. Hilder, D. J. Price, C. Pinte, F. Bollati, G. Lodato, and B. J. Norfolk: 2022, ‘Mapping the Planetary Wake in HD 163296 with Kinematics’. *The Astrophysical Journal* **929**, L25.

Cambrésy, L.: 1999, ‘Mapping of the Extinction in Giant Molecular Clouds Using Optical Star Counts’. *Astronomy and Astrophysics* **345**, 965–976.

Casassus, S. and S. Pérez: 2019, ‘Kinematic Detections of Protoplanets: A Doppler Flip in the Disk of HD 100546’. *The Astrophysical Journal* **883**, L41.

Chiang, E. I. and P. Goldreich: 1997, ‘Spectral Energy Distributions of T Tauri Stars with Passive Circumstellar Disks’. *The Astrophysical Journal* **490**, 368–376.

Christiaens, V., S. Casassus, S. Perez, G. van der Plas, and F. Ménard: 2014, ‘Spiral Arms in the Disk of HD 142527 from CO Emission Lines with ALMA’. *The Astrophysical Journal* **785**(1), L12.

Cieza, L. A. et al.: 2019, ‘The Ophiuchus DISC Survey Employing ALMA (ODISEA) - I: Project Description and Continuum Images at 28 AU Resolution’. *Monthly Notices of the Royal Astronomical Society* **482**, 698–714.

Cimerman, N. P. and R. R. Rafikov: 2021, ‘Planet-Driven Density Waves in Protoplanetary Discs: Numerical Verification of Non-Linear Evolution Theory’. *Monthly Notices of the Royal Astronomical Society* **508**, 2329–2349.

- Cleeves, L. I., K. I. Öberg, D. J. Wilner, J. Huang, R. A. Loomis, S. M. Andrews, and I. Czekala: 2016, ‘THE COUPLED PHYSICAL STRUCTURE OF GAS AND DUST IN THE IM Lup PROTOPLANETARY DISK’. *The Astrophysical Journal* **832**(2), 110.
- Currie, T. et al.: 2019, ‘No Clear, Direct Evidence for Multiple Protoplanets Orbiting LkCa 15: LkCa 15 Bcd Are Likely Inner Disk Signals’. *The Astrophysical Journal* **877**, L3.
- Currie, T. et al.: 2022, ‘Images of Embedded Jovian Planet Formation at a Wide Separation around AB Aurigae’. *Nature Astronomy*.
- Czekala, I. et al.: 2021, ‘Molecules with ALMA at Planet-forming Scales (MAPS). II. CLEAN Strategies for Synthesizing Images of Molecular Line Emission in Protoplanetary Disks’. *The Astrophysical Journal Supplement Series* **257**, 2.
- de Gregorio-Monsalvo, I. et al.: 2013, ‘Unveiling the Gas-and-Dust Disk Structure in HD 163296 Using ALMA Observations’. *Astronomy and Astrophysics* **557**, A133.
- Desort, M., A.-M. Lagrange, F. Galland, S. Udry, and M. Mayor: 2007, ‘Search for Exoplanets with the Radial-Velocity Technique: Quantitative Diagnostics of Stellar Activity’. *Astronomy and Astrophysics* **473**(3), 983–993.
- Dipierro, G., G. Laibe, D. J. Price, and G. Lodato: 2016, ‘Two Mechanisms for Dust Gap Opening in Protoplanetary Discs’. *Monthly Notices of the Royal Astronomical Society* **459**, L1–L5.
- Dipierro, G., D. Price, G. Laibe, K. Hirsh, A. Cerioli, and G. Lodato: 2015, ‘On Planet Formation in HL Tau’. *Monthly Notices of the Royal Astronomical Society* **453**, L73–L77.
- Disk Dynamics Collaboration, P. J. Armitage, J. Bae, M. Benisty, E. A. Bergin, S. Casassus, I. Czekala, S. Faccchini, J. Fung, C. Hall, J. D. Ilee, M. Keppler, A. Kuznetsova, R. Le Gal, R. A. Loomis, W. Lyra, N. Manger, S. Perez, C. Pinte, D. J. Price, G. Rosotti, J. Szulagyi, K. Schwarz, J. B. Simon, R. Teague, and K. Zhang: 2020, ‘Visualizing the Kinematics of Planet Formation’. *arXiv e-prints*.
- Dobbs, C. and J. Baba: 2014, ‘Dawes Review 4: Spiral Structures in Disc Galaxies’. *Publications of the Astronomical Society of Australia* **31**, e035.
- Dong, R., J. R. Najita, and S. Brittain: 2018, ‘Spiral Arms in Disks: Planets or Gravitational Instability?’. *The Astrophysical Journal* **862**, 103.
- Dong, R., Z. Zhu, and B. Whitney: 2015, ‘Observational Signatures of Planets in Protoplanetary Disks I. Gaps Opened by Single and Multiple Young Planets in Disks’. *The Astrophysical Journal* **809**, 93.
- Duffell, P. C. and A. I. MacFadyen: 2013, ‘Gap Opening by Extremely Low-mass Planets in a Viscous Disk’. *The Astrophysical Journal* **769**, 41.
- Edgeworth, K. E.: 1949, ‘The Origin and Evolution of the Solar System’. *Monthly Notices of the Royal Astronomical Society* **109**, 600–609.
- Fedele, D., M. Carney, M. R. Hogerheijde, C. Walsh, A. Miotello, P. Klaassen, S. Bruderer, T. Henning, and E. F. van Dishoeck: 2017, ‘ALMA Unveils Rings and Gaps in the Protoplanetary System HD 169142 Signatures of Two Giant Protoplanets’. *Astronomy & Astrophysics* **600**, A72.
- Fedele, D., M. Tazzari, R. Booth, L. Testi, C. J. Clarke, I. Pascucci, A. Kospal, D. Semenov, S. Bruderer, T. Henning, and R. Teague: 2018, ‘ALMA Continuum Observations of the Protoplanetary Disk AS 209. Evidence of Multiple Gaps Opened by a Single Planet’. *Astronomy & Astrophysics* **610**, A24.
- Ferrière, K. M.: 2001, ‘The Interstellar Environment of Our Galaxy’. *Reviews of Modern Physics* **73**, 1031–1066.
- Foreman-Mackey, D., D. W. Hogg, D. Lang, and J. Goodman: 2013, ‘Emcee: The MCMC Hammer’. *Publications of the Astronomical Society of the Pacific* **125**, 306.
- Fouchet, L., S. T. Maddison, J.-F. Gonzalez, and J. R. Murray: 2007, ‘The Effect of a Planet on the Dust Distribution in a 3D Protoplanetary Disk’. *Astronomy and Astrophysics* **474**(3), 1037–1047.
- Fung, J. and R. Dong: 2015, ‘Inferring Planet Mass from Spiral Structures in Protoplanetary Disks’. *The Astrophysical Journal* **815**, L21.

- Gaia Collaboration et al.: 2016, ‘Gaia Data Release 1. Summary of the Astrometric, Photometric, and Survey Properties’. *Astronomy & Astrophysics* **595**, A2.
- Gaia Collaboration et al.: 2018, ‘Gaia Data Release 2. Summary of the Contents and Survey Properties’. *Astronomy & Astrophysics* **616**, A1.
- Garg, H., C. Pinte, I. Hammond, R. Teague, T. Hilder, D. J. Price, J. Calcino, V. Christiaens, and P. P. Poblete: 2022, ‘A Kinematic Excess in the Annular Gap and Gas Depleted Cavity in the Disc around HD 169142’. *Monthly Notices of the Royal Astronomical Society* (Manuscript in press).
- Goldreich, P. and D. Lynden-Bell: 1965, ‘II. Spiral Arms as Sheared Gravitational Instabilities’. *Monthly Notices of the Royal Astronomical Society* **130**, 125.
- Goldreich, P. and S. Tremaine: 1978, ‘The Excitation and Evolution of Density Waves.’. *The Astrophysical Journal* **222**, 850–858.
- Goldreich, P. and S. Tremaine: 1979, ‘The Excitation of Density Waves at the Lindblad and Corotation Resonances by an External Potential.’. *The Astrophysical Journal* **233**, 857–871.
- Goldreich, P. and S. Tremaine: 1980, ‘Disk-Satellite Interactions.’. *The Astrophysical Journal* **241**, 425–441.
- Goodman, J. and R. R. Rafikov: 2001, ‘Planetary Torques as the Viscosity of Protoplanetary Disks’. *The Astrophysical Journal* **552**, 793–802.
- Gratton, R., R. Ligi, E. Sissa, S. Desidera, D. Mesa, M. Bonnefoy, G. Chauvin, A. Cheetham, M. Feldt, A. M. Lagrange, M. Langlois, M. Meyer, A. Vigan, A. Boccaletti, M. Janson, C. Lazzoni, A. Zurlo, J. De Boer, T. Henning, V. D’Orazi, L. Gluck, F. Madec, M. Jaquet, P. Baudoz, D. Fantinel, A. Pavlov, and F. Wildi: 2019, ‘Blobs, Spiral Arms, and a Possible Planet around HD 169142’. *Astronomy and Astrophysics* **623**, A140.
- Greaves, J. S. and W. K. M. Rice: 2010, ‘Have Protoplanetary Discs Formed Planets?’. *Monthly Notices of the Royal Astronomical Society* **407**, 1981–1988.
- Haffert, S. Y., A. J. Bohn, J. de Boer, I. A. G. Snellen, J. Brinchmann, J. H. Girard, C. U. Keller, and R. Bacon: 2019, ‘Two Accreting Protoplanets around the Young Star PDS 70’. *Nature Astronomy* **3**, 749–754.
- Hall, C., R. Dong, R. Teague, J. Terry, C. Pinte, T. Paneque-Carreño, B. Veronesi, R. D. Alexander, and G. Lodato: 2020, ‘Predicting the Kinematic Evidence of Gravitational Instability’. *The Astrophysical Journal* **904**, 148.
- Harris, C. R., K. J. Millman, S. J. van der Walt, R. Gommers, P. Virtanen, D. Cournapeau, E. Wieser, J. Taylor, S. Berg, N. J. Smith, R. Kern, M. Picus, S. Hoyer, M. H. van Kerkwijk, M. Brett, A. Haldane, J. F. del Río, M. Wiebe, P. Peterson, P. Gérard-Marchant, K. Sheppard, T. Reddy, W. Weckesser, H. Abbasi, C. Gohlke, and T. E. Oliphant: 2020, ‘Array Programming with NumPy’. *Nature* **585**, 357–362.
- Hartmann, L., N. Calvet, E. Gullbring, and P. D’Alessio: 1998, ‘Accretion and the Evolution of T Tauri Disks’. *The Astrophysical Journal* **495**, 385–400.
- Hayashi, C.: 1981, ‘Structure of the Solar Nebula, Growth and Decay of Magnetic Fields and Effects of Magnetic and Turbulent Viscosities on the Nebula’. *Progress of Theoretical Physics Supplement* **70**, 35–53.
- Helled, R., P. Bodenheimer, M. Podolak, A. Boley, F. Meru, S. Nayakshin, J. J. Fortney, L. Mayer, Y. Alibert, and A. P. Boss: 2014, ‘Giant Planet Formation, Evolution, and Internal Structure’. In: H. Beuther, R. S. Klessen, C. P. Dullemond, and T. Henning (eds.): *Protostars and Planets VI*. Germany, p. 643.
- Hendler, N., I. Pascucci, P. Pinilla, M. Tazzari, J. Carpenter, R. Malhotra, and L. Testi: 2020, ‘The Evolution of Dust Disk Sizes from a Homogeneous Analysis of 1-10 Myr Old Stars’. *The Astrophysical Journal* **895**, 126.
- Hill, G. W.: 1878, ‘Researches in the Lunar Theory’. *American Journal of Mathematics* pp. 5–26.
- Honda, M., K. Maaskant, Y. K. Okamoto, H. Kataza, M. Fukagawa, L. B. F. M. Waters, C. Dominik, A. G. G. M. Tielens, G. D. Mulders, M. Min, T. Yamashita, T. Fujiyoshi, T. Miyata, S. Sako, I. Sakon, H. Fujiwara, and T. Onaka: 2012, ‘MID-INFRARED IMAGING OF THE TRANSITIONAL DISK OF HD 169142: MEASURING THE SIZE OF THE GAP*’. *The Astrophysical Journal* **752**(2), 143.
- Hoyle, F.: 1953, ‘On the Fragmentation of Gas Clouds into Galaxies and Stars.’. **118**, 513.

Hoyle, F. and J. G. Ireland: 1961, ‘Note on the Magnetic Structure of the Galaxy’. *Monthly Notices of the Royal Astronomical Society* **122**, 35.

Huang, J., S. M. Andrews, C. P. Dullemond, A. Isella, L. M. Pérez, V. V. Guzmán, K. I. Öberg, Z. Zhu, S. Zhang, X.-N. Bai, M. Benisty, T. Birnstiel, J. M. Carpenter, A. M. Hughes, L. Ricci, E. Weaver, and D. J. Wilner: 2018a, ‘The Disk Substructures at High Angular Resolution Project (DSHARP). II. Characteristics of Annular Substructures’. *The Astrophysical Journal* **869**, L42.

Huang, J., S. M. Andrews, C. P. Dullemond, K. I. Öberg, C. Qi, Z. Zhu, T. Birnstiel, J. M. Carpenter, A. Isella, E. Macías, M. K. McClure, L. M. Pérez, R. Teague, D. J. Wilner, and S. Zhang: 2020, ‘A Multifrequency ALMA Characterization of Substructures in the GM Aur Protoplanetary Disk’. *The Astrophysical Journal* **891**, 48.

Huang, J., S. M. Andrews, L. M. Pérez, Z. Zhu, C. P. Dullemond, A. Isella, M. Benisty, X.-N. Bai, T. Birnstiel, J. M. Carpenter, V. V. Guzmán, A. M. Hughes, K. I. Öberg, L. Ricci, D. J. Wilner, and S. Zhang: 2018b, ‘The Disk Substructures at High Angular Resolution Project (DSHARP). III. Spiral Structures in the Millimeter Continuum of the Elias 27, IM Lup, and WaOph 6 Disks’. *The Astrophysical Journal* **869**, L43.

Hunter, J. D.: 2007, ‘Matplotlib: A 2D Graphics Environment’. *Computing in Science and Engineering* **9**, 90–95.

Hutchison, M., D. J. Price, and G. Laibe: 2018, ‘MULTIGRAIN: A Smoothed Particle Hydrodynamic Algorithm for Multiple Small Dust Grains and Gas’. *Monthly Notices of the Royal Astronomical Society* **476**(2), 2186–2198.

Isella, A., G. Guidi, L. Testi, S. Liu, H. Li, S. Li, E. Weaver, Y. Boehler, J. M. Carpenter, I. De Gregorio-Monsalvo, C. F. Manara, A. Natta, L. M. Pérez, L. Ricci, A. Sargent, M. Tazzari, and N. Turner: 2016, ‘Ringed Structures of the HD 163296 Protoplanetary Disk Revealed by ALMA’. *Physical Review Letters* **117**, 251101.

Izquierdo, A. F., S. Facchini, G. P. Rosotti, E. F. van Dishoeck, and L. Testi: 2022, ‘A New Planet Candidate Detected in a Dust Gap of the Disk around HD 163296 through Localized Kinematic Signatures: An Observational Validation of the DISCMINER’. *The Astrophysical Journal* **928**, 2.

Izquierdo, A. F., L. Testi, S. Facchini, G. P. Rosotti, and E. F. van Dishoeck: 2021, ‘The Disc Miner. I. A Statistical Framework to Detect and Quantify Kinematical Perturbations Driven by Young Planets in Discs’. *Astronomy and Astrophysics* **650**, A179.

Johansen, A., J. Blum, H. Tanaka, C. Ormel, M. Bizzarro, and H. Rickman: 2014, ‘The Multifaceted Planetesimal Formation Process’. In: H. Beuther, R. S. Klessen, C. P. Dullemond, and T. Henning (eds.): *Protostars and Planets VI*. Germany, p. 547.

Jorquera, S., L. M. Pérez, G. Chauvin, M. Benisty, Z. Zhu, A. Isella, J. Huang, L. Ricci, S. M. Andrews, S. Zhang, J. M. Carpenter, N. T. Kurtovic, and T. Birnstiel: 2021, ‘A Search for Companions via Direct Imaging in the DSHARP Planet-forming Disks’. *The Astronomical Journal* **161**, 146.

Jorsater, S. and G. A. van Moorsel: 1995, ‘High Resolution Neutral Hydrogen Observations of the Barred Spiral Galaxy NGC 1365’. *The Astronomical Journal* **110**, 2037.

Julian, W. H. and A. Toomre: 1966, ‘Non-Axisymmetric Responses of Differentially Rotating Disks of Stars’. *The Astrophysical Journal* **146**, 810.

Kanagawa, K. D., T. Muto, H. Tanaka, T. Tanigawa, T. Takeuchi, T. Tsukagoshi, and M. Momose: 2015a, ‘Mass Estimates of a Giant Planet in a Protoplanetary Disk from the Gap Structures’. *The Astrophysical Journal* **806**, L15.

Kanagawa, K. D., H. Tanaka, T. Muto, T. Tanigawa, and T. Takeuchi: 2015b, ‘Formation of a Disc Gap Induced by a Planet: Effect of the Deviation from Keplerian Disc Rotation’. *Monthly Notices of the Royal Astronomical Society* **448**, 994–1006.

Kenyon, S. J. and L. Hartmann: 1987, ‘Spectral Energy Distributions of T Tauri Stars: Disk Flaring and Limits on Accretion’. *The Astrophysical Journal* **323**, 714.

Keppler, M. et al.: 2018, ‘Discovery of a Planetary-Mass Companion within the Gap of the Transition Disk around PDS 70’. *Astronomy & Astrophysics* **617**, A44.

- Klahr, H. H. and P. Bodenheimer: 2003, ‘Turbulence in Accretion Disks: Vorticity Generation and Angular Momentum Transport via the Global Baroclinic Instability’. *The Astrophysical Journal* **582**, 869–892.
- Kratter, K. and G. Lodato: 2016, ‘Gravitational Instabilities in Circumstellar Disks’. *Annual Review of Astronomy and Astrophysics* **54**, 271–311.
- Landau, L. D. and E. M. Lifshitz: 1987, *Fluid Mechanics*. New Youk: Pergamon Press, second edition.
- Law, C. J. et al.: 2021a, ‘Molecules with ALMA at Planet-forming Scales (MAPS). III. Characteristics of Radial Chemical Substructures’. *The Astrophysical Journal Supplement Series* **257**, 3.
- Law, C. J. et al.: 2021b, ‘Molecules with ALMA at Planet-forming Scales (MAPS). IV. Emission Surfaces and Vertical Distribution of Molecules’. *The Astrophysical Journal Supplement Series* **257**, 4.
- LeVeque, R. J., D. Mihalas, E. Dorfi, and E. Müller: 1998, *Computational Methods for Astrophysical Fluid Flow*. Berlin Heidelberg: Springer-Verlag Berlin Heidelberg, first edition.
- Ligi, R. et al.: 2018, ‘Investigation of the Inner Structures around HD 169142 with VLT/SPHERE’. *Monthly Notices of the Royal Astronomical Society* **473**(2), 1774–1783.
- Lin, C. C. and F. H. Shu: 1964, ‘On the Spiral Structure of Disk Galaxies.’. *The Astrophysical Journal* **140**, 646.
- Lin, D. N. C. and J. Papaloizou: 1979, ‘Tidal Torques on Accretion Discs in Binary Systems with Extreme Mass Ratios.’. *Monthly Notices of the Royal Astronomical Society* **186**, 799–812.
- Lin, D. N. C. and J. C. B. Papaloizou: 1993, ‘On the Tidal Interaction between Protostellar Disks and Companions’. In: E. H. Levy and J. I. Lunine (eds.): *Protostars and Planets III*. Tuscan, p. 749.
- Lindblad, B.: 1963, ‘On the Possibility of a Quasi-Stationary Spiral Structure in Galaxies’. *Stockholms Observatoriums Annaler* **5**, 5.
- Lissauer, J. J.: 1993, ‘Planet Formation.’. *Annual Review of Astronomy and Astrophysics* **31**, 129–174.
- Lodato, G. and D. J. Price: 2010, ‘On the Diffusive Propagation of Warps in Thin Accretion Discs’. *Monthly Notices of the Royal Astronomical Society* **405**, 1212–1226.
- Long, F. et al.: 2018, ‘Gaps and Rings in an ALMA Survey of Disks in the Taurus Star-forming Region’. *The Astrophysical Journal* **869**, 17.
- Lynden-Bell, D. and J. P. Ostriker: 1967, ‘On the Stability of Differentially Rotating Bodies’. *Monthly Notices of the Royal Astronomical Society* **136**, 293.
- Lynden-Bell, D. and J. E. Pringle: 1974, ‘The Evolution of Viscous Discs and the Origin of the Nebular Variables.’. *Monthly Notices of the Royal Astronomical Society* **168**, 603–637.
- Lyra, W. and M. Kuchner: 2013, ‘Formation of Sharp Eccentric Rings in Debris Disks with Gas but without Planets’. *Nature* **499**, 184–187.
- Mac Low, M.-M. and R. S. Klessen: 2004, ‘Control of Star Formation by Supersonic Turbulence’. *Reviews of Modern Physics* **76**(1), 125–194.
- Macías, E., C. C. Espaillat, M. Osorio, G. Anglada, J. M. Torrelles, C. Carrasco-González, M. Flock, H. Linz, G. H.-M. Bertrang, T. Henning, J. F. Gómez, N. Calvet, and W. R. F. Dent: 2019, ‘Characterization of Ring Substructures in the Protoplanetary Disk of HD 169142 from Multiwavelength Atacama Large Millimeter/Submillimeter Array Observations’. *The Astrophysical Journal* **881**(2), 159.
- Mamajek, E. E.: 2009, ‘Initial Conditions of Planet Formation: Lifetimes of Primordial Disks’. In: T. Usuda, M. Tamura, and M. Ishii (eds.): *Exoplanets and Disks: Their Formation and Diversity*, Vol. 1158 of *American Institute of Physics Conference Series*. Hawaii, pp. 3–10.
- Manara, C. F., A. Morbidelli, and T. Guillot: 2018, ‘Why Do Protoplanetary Disks Appear Not Massive Enough to Form the Known Exoplanet Population?’. *Astronomy and Astrophysics* **618**, L3.
- Mayor, M. and D. Queloz: 1995, ‘A Jupiter-mass Companion to a Solar-Type Star’. *Nature* **378**, 355–359.

- Mie, G.: 1908, ‘Beiträge Zur Optik Trüber Medien, Speziell Kolloidaler Metallösungen’. *Annalen der Physik* **330**(3), 377–445.
- Miotello, A., I. Kamp, T. Birnstiel, L. I. Cleeves, and A. Kataoka: 2022, ‘Setting the Stage for Planet Formation: Measurements and Implications of the Fundamental Disk Properties’. *arXiv e-prints*.
- Miranda, R. and R. R. Rafikov: 2019, ‘Multiple Spiral Arms in Protoplanetary Disks: Linear Theory’. *The Astrophysical Journal* **875**, 37.
- Momose, M. et al.: 2015, ‘Detailed Structure of the Outer Disk around HD 169142 with Polarized Light in H-band’. *Publications of the Astronomical Society of Japan* **67**(5), 83.
- Najita, J. R. and S. J. Kenyon: 2014, ‘The Mass Budget of Planet-Forming Discs: Isolating the Epoch of Planetesimal Formation’. *Monthly Notices of the Royal Astronomical Society* **445**, 3315–3329.
- Nelson, R. P., O. Gressel, and O. M. Umurhan: 2013, ‘Linear and Non-Linear Evolution of the Vertical Shear Instability in Accretion Discs’. *Monthly Notices of the Royal Astronomical Society* **435**, 2610–2632.
- Öberg, K. I. et al.: 2021, ‘Molecules with ALMA at Planet-forming Scales (MAPS). I. Program Overview and Highlights’. *The Astrophysical Journal Supplement Series* **257**, 1.
- Ogilvie, G. I. and S. H. Lubow: 2002, ‘On the Wake Generated by a Planet in a Disc’. *Monthly Notices of the Royal Astronomical Society* **330**, 950–954.
- Ōki, T., M. Fujimoto, and Z. Hitotuyanagi: 1964, ‘Part III. Formation of Spiral Arms and Dynamical Model of Barred Galaxies’. *Progress of Theoretical Physics Supplement* **31**, 77–115.
- Oort, J. H.: 1962, ‘Spiral Structure’. In: L. Woltjer (ed.): *The Distribution and Motion of Interstellar Matter in Galaxies*. Princeton, p. 234.
- Osorio, M., G. Anglada, C. Carrasco-González, J. M. Torrelles, E. Macías, L. F. Rodríguez, J. F. Gómez, P. D’Alessio, N. Calvet, E. Nagel, W. R. F. Dent, S. P. Quanz, M. Reggiani, and J. M. Mayen-Gijon: 2014, ‘IMAGING THE INNER AND OUTER GAPS OF THE PRE-TRANSITIONAL DISK OF HD 169142 AT 7 Mm’. *The Astrophysical Journal Letters* **791**(2), L36.
- Paardekooper, S.-J. and G. Mellema: 2004, ‘Planets Opening Dust Gaps in Gas Disks’. *Astronomy and Astrophysics* **425**, L9–L12.
- Paardekooper, S.-J. and G. Mellema: 2006, ‘Dust Flow in Gas Disks in the Presence of Embedded Planets’. *Astronomy and Astrophysics* **453**(3), 1129–1140.
- Panić, O., M. R. Hogerheijde, D. Wilner, and C. Qi: 2008, ‘Gas and Dust Mass in the Disc around the Herbig Ae Star HD 169142’. *Astronomy & Astrophysics* **491**(1), 219–227.
- Panić, O., M. R. Hogerheijde, D. Wilner, and C. Qi: 2009, ‘A Break in the Gas and Dust Surface Density of the Disc around the T Tauri Star IM Lupi’. *Astronomy & Astrophysics* **501**(1), 269–278.
- Papaloizou, J. C. B. and D. N. C. Lin: 1995, ‘Theory Of Accretion Disks I: Angular Momentum Transport Processes’. *Annual Review of Astronomy and Astrophysics* **33**, 505–540.
- Pérez, L. M., J. M. Carpenter, S. M. Andrews, L. Ricci, A. Isella, H. Linz, A. I. Sargent, D. J. Wilner, T. Henning, A. T. Deller, C. J. Chandler, C. P. Dullemond, J. Lazio, K. M. Menten, S. A. Corder, S. Storm, L. Testi, M. Tazzari, W. Kwon, N. Calvet, J. S. Greaves, R. J. Harris, and L. G. Mundy: 2016, ‘Spiral Density Waves in a Young Protoplanetary Disk’. *Science* **353**, 1519–1521.
- Pérez, S., S. Casassus, C. Baruteau, R. Dong, A. Hales, and L. Cieza: 2019, ‘Dust Unveils the Formation of a Mini-Neptune Planet in a Protoplanetary Ring’. *The Astronomical Journal* **158**(1), 15.
- Pérez, S., S. Casassus, A. Hales, S. Marino, A. Cheetham, A. Zurlo, L. Cieza, R. Dong, F. Alarcón, P. Benítez-Llambay, E. Fomalont, and H. Avenhaus: 2020, ‘Long Baseline Observations of the HD 100546 Protoplanetary Disk with ALMA’. *The Astrophysical Journal* **889**, L24.
- Perez, S., A. Dunhill, S. Casassus, P. Roman, J. Szulágyi, C. Flores, S. Marino, and M. Montesinos: 2015, ‘Planet Formation Signposts: Observability of Circumplanetary Disks via Gas Kinematics’. *The Astrophysical Journal* **811**, L5.

- Pinilla, P., T. Birnstiel, L. Ricci, C. P. Dullemond, A. L. Uribe, L. Testi, and A. Natta: 2012, 'Trapping Dust Particles in the Outer Regions of Protoplanetary Disks'. *Astronomy & Astrophysics* **538**, A114.
- Pinte, C., T. J. Harries, M. Min, A. M. Watson, C. P. Dullemond, P. Woitke, F. Ménard, and M. C. Durán-Rojas: 2009, 'Benchmark Problems for Continuum Radiative Transfer. High Optical Depths, Anisotropic Scattering, and Polarisation'. *Astronomy and Astrophysics* **498**(3), 967–980.
- Pinte, C., F. Ménard, G. Duchêne, and P. Bastien: 2006, 'Monte Carlo Radiative Transfer in Protoplanetary Disks'. *Astronomy and Astrophysics* **459**(3), 797–804.
- Pinte, C., F. Ménard, G. Duchêne, T. Hill, W. R. F. Dent, P. Woitke, S. Maret, G. van der Plas, A. Hales, I. Kamp, W. F. Thi, I. de Gregorio-Monsalvo, C. Rab, S. P. Quanz, H. Avenhaus, A. Carmona, and S. Casassus: 2018a, 'Direct Mapping of the Temperature and Velocity Gradients in Discs. Imaging the Vertical CO Snow Line around IM Lupi'. *Astronomy and Astrophysics* **609**, A47.
- Pinte, C., D. J. Price, F. Ménard, G. Duchêne, V. Christiaens, S. M. Andrews, J. Huang, T. Hill, G. van der Plas, L. M. Perez, A. Isella, Y. Boehler, W. R. F. Dent, D. Mentiplay, and R. A. Loomis: 2020, 'Nine Localized Deviations from Keplerian Rotation in the DSHARP Circumstellar Disks: Kinematic Evidence for Protoplanets Carving the Gaps'. *The Astrophysical Journal* **890**, L9.
- Pinte, C., D. J. Price, F. Ménard, G. Duchêne, W. R. F. Dent, T. Hill, I. de Gregorio-Monsalvo, A. Hales, and D. Mentiplay: 2018b, 'Kinematic Evidence for an Embedded Protoplanet in a Circumstellar Disk'. *The Astrophysical Journal* **860**, L13.
- Pinte, C., G. van der Plas, F. Ménard, D. J. Price, V. Christiaens, T. Hill, D. Mentiplay, C. Ginski, E. Choquet, Y. Boehler, G. Duchêne, S. Perez, and S. Casassus: 2019, 'Kinematic Detection of a Planet Carving a Gap in a Protoplanetary Disk'. *Nature Astronomy* **3**, 1109–1114.
- Pohl, A. et al.: 2017, 'The Circumstellar Disk HD 169142: Gas, Dust, and Planets Acting in Concert?*'. *The Astrophysical Journal* **850**(1), 52.
- Pollack, J. B., O. Hubickyj, P. Bodenheimer, J. J. Lissauer, M. Podolak, and Y. Greenzweig: 1996, 'Formation of the Giant Planets by Concurrent Accretion of Solids and Gas'. *Icarus* **124**, 62–85.
- Price, D. J. et al.: 2018, 'Phantom: A Smoothed Particle Hydrodynamics and Magnetohydrodynamics Code for Astrophysics'. *Publications of the Astronomical Society of Australia* **35**, e031.
- Price, D. J. and G. Laibe: 2015, 'A Fast and Explicit Algorithm for Simulating the Dynamics of Small Dust Grains with Smoothed Particle Hydrodynamics'. *Monthly Notices of the Royal Astronomical Society* **451**, 813–826.
- Pringle, J. E.: 1981, 'Accretion Discs in Astrophysics'. *Annual Review of Astronomy and Astrophysics* **19**, 137–162.
- Pringle, J. E. and A. King: 2007, *Astrophysical Flows*. New York: Cambridge University Press.
- Quanz, S. P., A. Amara, M. R. Meyer, M. A. Kenworthy, M. Kasper, and J. H. Girard: 2013a, 'A Young Protoplanet Candidate Embedded in the Circumstellar Disk of HD 100546'. *The Astrophysical Journal* **766**, L1.
- Quanz, S. P., H. Avenhaus, E. Buenzli, A. Garufi, H. M. Schmid, and S. Wolf: 2013b, 'GAPS IN THE HD 169142 PROTOPLANETARY DISK REVEALED BY POLARIMETRIC IMAGING: SIGNS OF ONGOING PLANET FORMATION?*'. *The Astrophysical Journal Letters* **766**(1), L2.
- Rafikov, R.: 2002a, 'Nonlinear Propagation of Planet-Generated Tidal Waves'. *The Astrophysical Journal* **569**(2), 997–1008.
- Rafikov, R. R.: 2002b, 'Planet Migration and Gap Formation by Tidally Induced Shocks'. *The Astrophysical Journal* **572**, 566–579.
- Raman, A., M. Lisanti, D. J. Wilner, C. Qi, and M. Hogerheijde: 2006, 'A Keplerian Disk around the Herbig Ae Star HD 169142'. *The Astronomical Journal* **131**(4), 2290.
- Rameau, J. et al.: 2017, 'An Optical/Near-infrared Investigation of HD 100546 b with the Gemini Planet Imager and MagAO'. *The Astronomical Journal* **153**, 244.

- Reggiani, M. et al.: 2014, ‘DISCOVERY OF A COMPANION CANDIDATE IN THE HD 169142 TRANSITION DISK AND THE POSSIBILITY OF MULTIPLE PLANET FORMATION’. *The Astrophysical Journal Letters* **792**(1), L23.
- Reggiani, M. et al.: 2018, ‘Discovery of a Point-like Source and a Third Spiral Arm in the Transition Disk around the Herbig Ae Star MWC 758’. *Astronomy and Astrophysics* **611**, A74.
- Safronov, V. S.: 1972, *Evolution of the Protoplanetary Cloud and Formation of the Earth and Planets*.
- Sallum, S., K. B. Follette, J. A. Eisner, L. M. Close, P. Hinz, K. Kratter, J. Males, A. Skemer, B. Macintosh, P. Tuthill, V. Bailey, D. Defrère, K. Morzinski, T. Rodigas, E. Spalding, A. Vaz, and A. J. Weinberger: 2015, ‘Accreting Protoplanets in the LkCa 15 Transition Disk’. *Nature* **527**, 342–344.
- Sano, T., S. M. Miyama, T. Umebayashi, and T. Nakano: 2000, ‘Magnetorotational Instability in Protoplanetary Disks. II. Ionization State and Unstable Regions’. *The Astrophysical Journal* **543**, 486–501.
- Shakura, N. I. and R. A. Sunyaev: 1973, ‘Black Holes in Binary Systems. Observational Appearance.’. *Astronomy and Astrophysics*, Vol. 24, p. 337 - 355 **24**, 337.
- Stone, J. M., K. Tomida, C. J. White, and K. G. Felker: 2020, ‘The Athena++ Adaptive Mesh Refinement Framework: Design and Magnetohydrodynamic Solvers’. *The Astrophysical Journal Supplement Series* **249**, 4.
- Szulágyi, J., F. Masset, E. Lega, A. Crida, A. Morbidelli, and T. Guillot: 2016, ‘Circumplanetary Disc or Circumplanetary Envelope?’. *Monthly Notices of the Royal Astronomical Society* **460**, 2853–2861.
- Teague, R.: 2019, ‘Eddy: Extracting Protoplanetary Disk Dynamics with Python’. *The Journal of Open Source Software* **4**, 1220.
- Teague, R., J. Bae, S. M. Andrews, M. Benisty, E. A. Bergin, S. Facchini, J. Huang, C. Longarini, and D. Wilner: 2022, ‘Mapping the Complex Kinematic Substructure in the TW Hya Disk’. *The Astrophysical Journal* **936**, 163.
- Teague, R., J. Bae, E. A. Bergin, T. Birnstiel, and D. Foreman-Mackey: 2018, ‘A Kinematical Detection of Two Embedded Jupiter-mass Planets in HD 163296’. *The Astrophysical Journal* **860**, L12.
- Teague, R. et al.: 2021, ‘Molecules with ALMA at Planet-forming Scales (MAPS). XVIII. Kinematic Substructures in the Disks of HD 163296 and MWC 480’. *The Astrophysical Journal Supplement Series* **257**, 18.
- Teague, R. and D. Foreman-Mackey: 2018, ‘A Robust Method to Measure Centroids of Spectral Lines’. *Research Notes of the AAS* **2**(3), 173.
- The CASA Team et al.: 2022, ‘CASA, the Common Astronomy Software Applications for Radio Astronomy’. *arXiv e-prints*.
- Toci, C., G. Lodato, D. Fedele, L. Testi, and C. Pinte: 2019, ‘Long-Lived Dust Rings around HD 169142’. *The Astrophysical Journal Letters* **888**(1), L4.
- Toomre, A.: 1964, ‘On the Gravitational Stability of a Disk of Stars.’. *The Astrophysical Journal* **139**, 1217–1238.
- Toomre, A.: 1969, ‘Group Velocity of Spiral Waves in Galactic Disks’. *The Astrophysical Journal* **158**, 899.
- Tripathi, A., S. M. Andrews, T. Birnstiel, and D. J. Wilner: 2017, ‘A Millimeter Continuum Size-Luminosity Relationship for Protoplanetary Disks’. *The Astrophysical Journal* **845**, 44.
- Tychoniec, Ł., C. F. Manara, G. P. Rosotti, E. F. van Dishoeck, A. J. Cridland, T.-H. Hsieh, N. M. Murillo, D. Segura-Cox, S. E. van Terwisga, and J. J. Tobin: 2020, ‘Dust Masses of Young Disks: Constraining the Initial Solid Reservoir for Planet Formation’. *Astronomy and Astrophysics* **640**, A19.
- Väistö, P., S. Ryder, S. Mattila, and J. Kotilainen: 2008, ‘A Pair of Leading Spiral Arms in a Luminous Infrared Galaxy?’. *The Astrophysical Journal* **689**, L37.
- van der Marel, N., E. F. van Dishoeck, S. Bruderer, L. Pérez, and A. Isella: 2015, ‘Gas Density Drops inside Dust Cavities of Transitional Disks around Young Stars Observed with ALMA’. *Astronomy and Astrophysics* **579**, A106.

- van Terwisga, S. E., E. F. van Dishoeck, P. Cazzoletti, S. Facchini, L. Trapman, J. P. Williams, C. F. Manara, A. Miotello, N. van der Marel, M. Ansdell, M. R. Hogerheijde, M. Tazzari, and L. Testi: 2019, 'The ALMA Lupus Protoplanetary Disk Survey: Evidence for Compact Gas Disks and Molecular Rings from CN'. *Astronomy and Astrophysics* **623**, A150.
- Verriots, H. J., D. J. Price, C. Pinte, T. Hilder, and J. Calcino: 2022, 'Kinematic Evidence for an Embedded Planet in the IM Lupi Disk'. *The Astrophysical Journal* **934**, L11.
- Virtanen, P. et al.: 2020, 'SciPy 1.0: Fundamental Algorithms for Scientific Computing in Python'. *Nature Methods* **17**, 261–272.
- Ward, W. R.: 1986, 'Density Waves in the Solar Nebula: Differential Lindblad Torque'. *Icarus* **67**, 164–180.
- Ward, W. R.: 1997, 'Protoplanet Migration by Nebula Tides'. *Icarus* **126**, 261–281.
- Weidenschilling, S. J.: 1977a, 'Aerodynamics of Solid Bodies in the Solar Nebula'. *Monthly Notices of the Royal Astronomical Society* **180**, 57–70.
- Weidenschilling, S. J.: 1977b, 'The Distribution of Mass in the Planetary System and Solar Nebula'. *Astrophysics and Space Science* **51**(1), 153–158.
- Weingartner, J. C. and B. T. Draine: 2001, 'Dust Grain-Size Distributions and Extinction in the Milky Way, Large Magellanic Cloud, and Small Magellanic Cloud'. *The Astrophysical Journal* **548**(1), 296.
- Whitham, G. B.: 1999, *Linear and Nonlinear Waves*. New York: John Wiley & Sons, Ltd.
- Wilczynski, E. J.: 1896, 'Outlines of a Theory of Spiral and Planetary Nebulae'. *The Astrophysical Journal* **4**, 97.
- Woolfson, M.: 2000, 'The Origin and Evolution of the Solar System'. *Astronomy & Geophysics*, Vol. 41, Issue 1, p.12 **41**(1), 12.
- Yu, H., R. Teague, J. Bae, and K. Öberg: 2021, 'Mapping the 3D Kinematical Structure of the Gas Disk of HD 169142'. *The Astrophysical Journal* **920**, L33.
- Yun, M. S.: 1999, 'Tidal Interactions in M81 Group'. In: *Galaxy Interactions at Low and High Redshift*, Vol. 186. Kyoto, Japan, p. 81.
- Zhang, K., G. A. Blake, and E. A. Bergin: 2015, 'Evidence of Fast Pebble Growth Near Condensation Fronts in the HL Tau Protoplanetary Disk'. *The Astrophysical Journal* **806**, L7.
- Zhang, K. et al.: 2021, 'Molecules with ALMA at Planet-forming Scales (MAPS). V. CO Gas Distributions'. *The Astrophysical Journal Supplement Series* **257**, 5.
- Zhang, S. et al.: 2018, 'The Disk Substructures at High Angular Resolution Project (DSHARP). VII. The Planet-Disk Interactions Interpretation'. *The Astrophysical Journal* **869**, L47.
- Zhu, Z.: 2019, 'Inclined Massive Planets in a Protoplanetary Disc: Gap Opening, Disc Breaking, and Observational Signatures'. *Monthly Notices of the Royal Astronomical Society* **483**, 4221–4241.
- Zhu, Z., R. Dong, J. M. Stone, and R. R. Rafikov: 2015, 'The Structure of Spiral Shocks Excited by Planetary-mass Companions'. *The Astrophysical Journal* **813**, 88.
- Zhu, Z., J. M. Stone, and R. R. Rafikov: 2012, 'Planet-Disk Interaction in Three Dimensions: The Importance of Buoyancy Waves'. *The Astrophysical Journal* **758**, L42.